

ANALYTICAL APPROXIMATIONS FOR CALCULATING THE ESCAPE AND ABSORPTION OF RADIATION IN CLUMPY DUSTY ENVIRONMENTS

Frank Városi¹ and Eli Dwek
Laboratory for Astronomy and Solar Physics
Code 685
NASA Goddard Space Flight Center
Greenbelt MD 20771

Submitted to ApJ: February 4, 1999 – Accepted: March 10, 1999

ABSTRACT

We present analytical approximations for the scattering, absorption and escape of non-ionizing photons from spherically symmetric two-phase clumpy media, with either a central point source of isotropic radiation, a uniform distribution of isotropic emitters, or uniformly illuminated by external sources. The analytical approximations are based on the mega-grains model of two-phase clumpy media, as proposed by Hobson & Padman, combined with escape and absorption probability formulae for homogeneous media. The accuracy of the approximations is examined by comparison with three-dimensional Monte Carlo simulations of radiative transfer, including multiple scattering. Our studies show that the combined mega-grains and escape/absorption probability formulae provide a good approximation of the escaping and absorbed radiation fractions for a wide range of parameters characterizing the clumpiness and optical properties of the medium.

A realistic test of the analytic approximations is performed by modeling the absorption of a stellar-like source of radiation by interstellar dust in a clumpy medium, and by calculating the resulting equilibrium dust temperatures and infrared emission spectrum of both the clumps and the interclump medium. In particular, we find that the temperature of dust in clumps is lower than in the interclump medium if the clumps are optically thick at wavelengths where most of the absorption occurs. Comparison with Monte Carlo simulations of radiative transfer in the same environment shows that the analytic model yields a good approximation of dust temperatures and the emerging UV to FIR spectrum of radiation for all three types of source distributions mentioned above.

Our analytical model provides a numerically expedient way to estimate radiative transfer in a variety of interstellar conditions and can be applied to a wide range of astrophysical environments, from clumpy star forming regions to starburst galaxies.

¹Raytheon ITSS, varosi@gssc.nasa.gov

Contents

1 INTRODUCTION	3	7 MODELING THE ABSORPTION OF STELLAR RADIATION BY DUST AND THE INFRARED EMISSION	37
2 MONTE CARLO SIMULATION OF RADIATIVE TRANSFER	5	7.1 Absorbed Luminosities and the Distribution of Dust Temperatures . .	38
2.1 General Simulation Methods	5	7.2 The Emerging UV-FIR SED	43
2.2 Radiative Transfer in Two-Phase Clumpy Media	6	7.3 Exploring Parameter Space with the MGEF Model	44
3 ESCAPE AND ABSORPTION IN HOMOGENEOUS MEDIA	10	8 SUMMARY AND CONCLUSIONS	46
3.1 Central Isotropic Point Source	10	A FINAL FLUX APPORTIONMENT IN MONTE CARLO	47
3.2 Uniformly Distributed Emission	11	B RANDOM CLUMPS IN A TWO PHASE MEDIUM	49
3.3 Finite Number of Uniformly Distributed Point Sources	13	C ESCAPE AND INTERACTION PROBABILITIES FOR A SPHERE	49
3.4 Uniformly Illuminating External Source	14	C.1 No Scattering	49
4 ESCAPE AND ABSORPTION IN CLUMPY MEDIA	16	C.2 Including Scattering	51
4.1 The Mega-Grains Approximation . . .	16	D ANALYSIS OF CLUMP OVERLAPS	52
4.1.1 Effective Optical Depth	17	E DISTRIBUTION OF DUST TEMPERATURES AROUND A POINT SOURCE OF RADIATION	53
4.1.2 Effective Scattering Albedo . .	17		
4.1.3 Effective Scattering Asymmetry Parameter	19		
4.2 The Extended Mega-Grains Approximation	20		
4.3 Comparison with Earlier Theory . . .	26		
4.4 Escape and Absorption Probabilities for Clumpy Media	27		
4.5 The Fractions Absorbed in Each Phase of a Clumpy Medium	28		
5 SUMMARY OF EQUATIONS	29		
5.1 Escape and Absorption Probabilities .	29		
5.2 Mega-Grains Approximation	29		
5.3 Fractions Absorbed in Each Phase . .	30		
5.4 The Case of $\alpha < 1$	30		
6 COMPARISON OF ANALYTIC APPROXIMATIONS WITH MONTE CARLO SIMULATIONS	30		
6.1 Dependence on Optical Depth	31		
6.2 Dependence on Filling Factor	33		
6.3 Dependence on Density Ratio	35		
6.4 Body Centered Cubic Lattice of Clumps	35		

1. INTRODUCTION

Radiative transfer plays an important role in the spectral appearance of almost all astrophysical systems ranging from isolated star forming regions to protogalactic and galactic systems. At wavelengths longer than the Lyman limit, absorption and scattering by dust in the intervening medium is the major factor affecting the transfer of radiation. Most of the transfer of radiation occurs in the interstellar medium (ISM) of the host system of the emitting sources. For simplicity, models of radiative transfer often assume a homogeneous distribution of dust and gas, although in reality the structure of the ISM is observed to be significantly more complex.

In our Galaxy, the ISM is known to be composed of at least five phases that are in approximate pressure equilibrium: cold dense molecular clouds, cold diffuse clouds, warm diffuse clouds, H II regions, and hot low density cavities created by supernova remnants (Spitzer 1978, Cox 1995, McKee 1995, Knapp 1995). The ISM is observed to have clumpy structure even at very small scales (Marscher et al. 1993, Stutzki & Gusten 1990). Data from CO line emission indicate a distribution of molecular clouds having a power-law cloud mass spectrum (Sanders, Scoville, and Solomon 1985). Dickey & Garwood (1989) find the same cloud mass spectrum based on 21 cm emission line data. Most likely the ISM has a spectrum of densities and temperatures with correlated multi-scale spatial structure, as evidenced by sky surveys such as the Infrared Astronomical Satellite (IRAS) and 21 cm surveys. Analysis of IRAS 100 μ m sky flux indicates that the diffuse H I clouds have a fractal distribution (Bazell & Desert 1988, Waller et al. 1997). Analysis of CO column densities and emission line profiles further suggests that a fractal distribution of matter applies to the molecular component of the ISM as well (Falgarone 1995, Elmegreen & Falgarone 1996). The complex, possibly fractal, distribution of gas and dust is supported by theoretical arguments as well (Pfenniger & Combes 1994, Rosen & Bregman 1995, Norman & Ferrara 1996, Elmegreen 1997). Thus the ISM is clearly inhomogeneous and simulations of radiative transfer should account for this fact.

The simplest model of an inhomogeneous medium is that consisting of two phases: dense clumps embedded in a less dense interclump medium (ICM). Natta & Panagia (1984) developed simple analytic approximations for the effective optical depth of clumpy

media with no scattering and an empty ICM. Radiative transfer with isotropic scattering in a two-phase clumpy medium (non-empty ICM) with plane-parallel geometry was investigated by Boissé (1990). He used a Markov process model of the medium to develop analytical approximations for the intensity of radiation. Comparison with 3D Monte Carlo simulations verified the accuracy of the approximations. Hobson & Scheuer (1993) developed analytic solutions of radiative transfer with isotropic scattering in N -phase clumpy media using a Markov process model, which they compared with Monte Carlo simulations for the cases of two or three phases. Analytic approximations for radiative transfer in two-phase clumpy media were also developed by Neufeld (1991) and Hobson & Padman (1993), and we discuss and utilize them in later sections of this paper. Witt & Gordon (1996) performed extensive Monte Carlo simulations of the transfer of radiation from a central point source in a spherical two-phase clumpy medium when the scattering is not isotropic, more typical of UV photons scattered by dust. Their simulations showed that the nonlinear variation of effective optical depth and effective albedo with respect to parameters characterizing the clumpy medium could lead to erroneous estimates of the dust albedo and opacity if one assumes a homogeneous medium when modeling what may actually be a clumpy medium. Gordon, Calzetti, and Witt (1997) applied the Monte Carlo model of Witt & Gordon to the study of dust in starburst galaxies, concluding that a shell of clumpy dust around a starburst provides the best model of spectral data. Radiative transfer in a clumpy environment was also investigated by Wolf, Fischer & Pfau (1998), with results similar to Witt & Gordon.

All the simulations and studies mentioned above verify the general expectation that a medium is more transparent when it is clumpy. This can be demonstrated in the following generic example, which then leads to the concept of effective optical depth in an inhomogeneous medium. Consider N randomly chosen parallel and equal length lines of sight of through an inhomogeneous medium acting as a foreground screen. Let τ_i be the optical depth of the i -th line of sight, defined as the product of column density and cross-section of the dust, so that $e^{-\tau_i}$ is the transmission. If N is large (e.g. the number of photons per second emitted by a galaxy) then we can compute the average transmission of all the lines of sight,

which defines the effective optical depth:

$$\tau_{eff} \equiv -\ln \left(\frac{1}{N} \sum_i \exp(-\tau_i) \right). \quad (1)$$

On the other hand, the average of all the optical depths equals the optical depth of the homogeneous medium with equal dust mass:

$$\tau_{hom} \equiv \frac{1}{N} \sum_i \tau_i. \quad (2)$$

Using standard calculus one can prove the inequality

$$\frac{1}{N} \sum_i \exp(-\tau_i) > \exp \left(-\frac{1}{N} \sum_i \tau_i \right), \quad (3)$$

which states that the average transmission of the inhomogeneous medium is greater than that of the equivalent homogeneous medium, allowing relatively more photons to escape. The expression can be an equality only when $\tau_i = \tau_{hom}$ for all lines of sight, i.e. only if the medium is homogeneous. Applying the negative natural logarithm to the inequality (3) and using the definitions (1) and (2) gives

$$\tau_{eff} < \tau_{hom}, \quad (4)$$

so the effective optical depth of an inhomogeneous medium is less than that of a homogeneous medium with equal mass of dust. When the dust also scatters photons, the above inequality can be considered to apply approximately to the scattered photons, so we again expect generically a greater transmission through inhomogeneous media than the equivalent homogeneous medium. In this paper we study the dependence of the nonlinear relationship between τ_{eff} and τ_{hom} on parameters characterizing a clumpy medium, and also give approximations for how absorption of photons is apportioned in each phase of the medium.

One consequence of the fact that $\tau_{eff} < \tau_{hom}$ for an inhomogeneous medium is that a large mass of dust could be concealed in dense regions even though observations of low extinction infer a small mass of dust. Such dense clumps of dust could have a lower temperature than if the dust were distributed homogeneously, providing an alternative explanation of observations which show a discrepancy between dust temperature and absorbed luminosity, as found in recent infrared spectral observations of the Galactic

Center (Chan et al. 1997). For these types of modeling efforts, easily computable analytic approximations of radiative transfer in clumpy media are desirable since they would enable the rapid exploration of the effects of varying the parameters in an astrophysical model. The more time consuming Monte Carlo simulations can be used to guide the development and test the accuracy of analytical approximations.

We have developed a general Monte Carlo Radiative Transfer (MCRT) code for simulating radiative transfer with multiple scattering in a three dimensional inhomogeneous medium, utilizing some novel techniques. The model is restricted to non-ionizing radiation, hence the only absorption and scattering considered is due to dust. We repeated many of the Monte Carlo simulations of Witt & Gordon and our results are in good agreement. The medium in their model is composed of cubic clumps randomly located on a body centered cubic lattice. We instead concentrate our studies on two-phase media composed of spherical clumps because the radiative transfer properties of such media are more directly approximated by analytic formulas in the mega-grains model of Hobson & Padman (1993), hereafter HP93. Furthermore, we extend the research of HP93 by computing the fraction of photons absorbed in each phase of the medium and improving the approximations for scattering. The resulting formulae allow for convenient and rapid exploration of the effects of varying the parameters defining the environment on the escape and absorption of radiation. The cases of a central isotropic point source, uniformly distributed isotropic emitters, and uniformly illuminating external sources are studied for homogeneous and clumpy media, with both MCRT simulations and analytic approximations, over a wide range of dust optical depths, scattering albedos, and from isotropic to forward scattering. The validity and accuracy of the analytical approximations is tested by detailed comparison with MCRT simulations.

We have also investigated the transfer of radiation in a fractal distribution of dust density (Városi & Dwek 1997) using MCRT, where the fractal construction is based on methods given in Elmegreen (1997). Briefly, the variation of the escape of radiation in a fractal medium as a function of τ_{hom} is similar to that of clumpy media, and we find that the mega-grains model can be used to approximate the escaping fraction of photons if some additional assumptions are imposed. However, the distribution of absorbed radi-

ation is more complicated than in two-phase clumpy media since there is a spectrum of densities in the fractal case. Studies and approximations of radiative transfer in complex and fractal media will be presented elsewhere (Városi & Dwek 1999).

The paper is organized as follows. Section 2 describes the MCRT code and its application to two-phase clumpy media. In §3 we present analytical approximations for the fraction of radiation escaping from or absorbed by homogeneous media in spherical geometry, for each of the three types of sources mentioned above. In §4 we present the mega-grains model of two-phase clumpy media, and also some improvements and extensions. The mega-grains approach is combined with the formulae for homogeneous media to get approximations for the escaping/absorbed fractions in clumpy media, and also the fractions absorbed in clumps and the ICM. Section 5 gives a summary of all the equations in a convenient list. Then in §6, we demonstrate the validity of the analytic approximations by comparison with MCRT simulations. In §7 we present a realistic test of the analytical model by simulating the scattering, escape, and absorption of a stellar-like emission spectrum by a clumpy distribution of interstellar dust, and then comparing the predicted equilibrium dust temperatures and emerging UV-FIR spectrum with the results of MCRT simulations. The analytical model is also used to explore a large region of parameter space characterizing the clumpy medium, and we explain why the dust temperature in clumps is lower than in the ICM. The summary and conclusions are presented in §8.

2. MONTE CARLO SIMULATION OF RADIATIVE TRANSFER

2.1. General Simulation Methods

The Monte Carlo code we have developed simulates coherent scattering and absorption of photons by dust with any kind of spatial distribution and composition. The spatial distribution of the dust is specified by a continuous function $\rho(x, y, z)$, the mass of dust per unit volume. In practice this quantity is defined on a discrete three-dimensional grid. For each wavelength simulated, the number of photons absorbed by the dust in each volume element (voxel) of the 3D grid is saved, allowing computation of the dust temperatures and resulting infrared emission spectrum.

The grid resolution is limited only by the available computer memory: increasing the number of

grid elements does not significantly affect the computation time. This is achieved by employing the Monte Carlo method of rejections (Neumann 1951) in selecting the random distances each photon travels between interactions (absorption or scattering) with the dust, as described in Lux & Koblinger (1995). The method proceeds as follows. Let $\mathbf{r} \equiv (x, y, z)$ be the initial position of the emitted photon, and ρ_{\max} be the maximum dust mass density in the direction $\hat{\mathbf{l}}$ the photon is traveling. Assume temporarily that the density is uniform and equal to ρ_{\max} along its path. In that case the probability that the photon will travel a distance s without having an interaction is $\exp(-s\kappa\rho_{\max})$, where κ is the dust mass extinction coefficient. Applying the fundamental principle of the Monte Carlo method, one can choose a uniformly distributed random variable $0 < \zeta < 1$ and set ζ to be equal to $1 - \exp(-s\kappa\rho_{\max})$, the probability that an interaction will occur, and then solve for s , the random value for the interaction distance, to give:

$$s = -\frac{\ln(1 - \zeta)}{\kappa\rho_{\max}}. \quad (5)$$

Note that $(\kappa\rho_{\max})^{-1}$ is the worst case mean-free-path. One then has to play a rejection game in order to determine if the supposed interaction at the new location, $\mathbf{r}' = \mathbf{r} + s\hat{\mathbf{l}}$, is accepted as a real interaction, because the density is of course *not* everywhere equal to ρ_{\max} . We choose another uniformly distributed random number $0 < \vartheta < 1$ and compare it to $\rho(\mathbf{r}')/\rho_{\max}$, the ratio of the actual density at the event location \mathbf{r}' to the maximum density along $\hat{\mathbf{l}}$. If $\vartheta \leq \rho(\mathbf{r}')/\rho_{\max}$ the supposed interaction is accepted as real. In particular, if $\rho(\mathbf{r}')/\rho_{\max} = 1$, all values of the random variable ϑ will fall below this ratio, and the interaction will be accepted as real. Thus $\rho(\mathbf{r}')/\rho_{\max}$ is equal to the probability that an interaction is real. If it happens that $\vartheta > \rho(\mathbf{r}')/\rho_{\max}$ the interaction is rejected and called a virtual interaction. After a virtual interaction the photon is allowed to travel in the same direction another random distance selected by eq.(5), and the above steps are repeated until an interaction event is accepted as real or the photon escapes. After evolving many photons in this manner, the method effectively integrates the density along all directions of travel while performing the Monte Carlo simulation of photon interactions. The 3D medium need only be specified with a point density function, and the method is simpler than performing numerical integrations along each photon path to determine in

which voxel the photon will interact with dust. For most simulations one can set ρ_{\max} equal to the maximum density of the entire medium, thereby further simplifying the process. However if $\rho_{\max} \gg \rho_{\min}$ and the high density regions occupy a very small fraction of the volume, it is worthwhile to have an algorithm for determining the maximum density in a given direction, otherwise the method may iterate through many virtual interactions before getting to a real interaction or escaping, using up more CPU time.

Our Monte Carlo code follows a large group of randomly emitted photons simultaneously, typically 10^5 at a time, through multiple scatterings and to eventual absorption or escape. Each photon is given an initial flux weight of unity, and this weight changes as the photon interacts with the dust. The simulation proceeds via iterations, as follows. First, the group of photons travel randomly selected distances (as described above) depending on the dust density encountered, and then photons either escape the medium (reducing the number in the group) or interact with dust. Photons which interact are considered to experience both scattering and absorption: they are reduced in flux weight by the dust scattering albedo $\omega \equiv \sigma_{\text{scat}}/\sigma_{\text{ext}}$ (the ratio of scattering to extinction cross-section), and a fraction $1 - \omega$ of the energy of each interacting photon is absorbed by the dust at the locations of interaction. The path of each scattered photon is deflected by a random angle, θ_{scat} , which is distributed according to the Henyey-Greenstein (HG) phase function (Henyey & Greenstein 1941), fully characterized by the parameter $g = \langle \cos \theta_{\text{scat}} \rangle$, the average value of the cosine of the deflection angles, also called the asymmetry parameter. The random scattering deflection angles are selected by the method given in Witt (1977). The remaining photons having new directions are fed back into the beginning of the iteration procedure. This cycle of interaction, absorption and scattering is repeated until the net flux of photons remaining in the medium is a small fraction of the flux that has escaped (e.g. less than 5%).

The flux of photons remaining after the iterations are terminated is divided into escaping and absorbed fractions according to a new scheme which considers the history of the escaping photons during each iteration and the dust scattering albedo. Let N_k be the number of photons remaining after iteration k , and let m be the total number of iterations performed. If the remaining fraction after each iteration, given by the ratio $\beta_k = N_k/N_{k-1} \leq 1$, is tending toward a

constant value, then the fraction of the final N_m photons that will escape if the iterations were continued ad-infinitum is approximately (see Appendix A)

$$f_m^{\text{esc}} = \frac{1 - \beta_m}{1 - \omega\beta_m} . \quad (6)$$

Thus upon termination after m scatterings we assume that a fraction f_m^{esc} of the remaining flux escapes and a fraction $1 - f_m^{\text{esc}}$ is absorbed at the current location. Testing of the formula has shown that even if the multiple scattering is terminated after a few iterations when the flux remaining is 20% of the escaped flux, the final escaping fraction of flux obtained after applying eq.(6) is as accurate as if the iteration was continued until the remaining flux is less than 1% of the escaped flux, and the total computation time is reduced. Of course when the iterations are prematurely terminated, the locations of the photon absorptions and exits are not quite as accurate as when the iterations are continued, but the error is always less than the ratio of the flux that was remaining to that which already escaped. In any case, using eq.(6) is more intelligent than considering the remaining flux to be all escaped, all absorbed, or split up using just the scattering albedo.

2.2. Radiative Transfer in Two-Phase Clumpy Media

The main parameters defining a two-phase clumpy medium are the volume filling factor of the clumps, f_c , the ratio of the clump to interclump medium (ICM) densities, $\alpha = \rho_c/\rho_{\text{icm}}$, the total dust mass M , and the volume V of the medium. Typical ranges which may describe parts of the interstellar medium are $0.01 < f_c < 0.3$ and $10 < \alpha < 10^7$ (Spitzer 1978, van Buren 1989, Murthy et al. 1992, Gaustad & van Buren 1993). The number of clumps and the clump sizes are secondary parameters, inversely related, which we shall discuss later. To obtain a formula for the ICM density, first define the density of the equivalent homogeneous medium to be $\rho_{\text{hom}} = M/V$. Then since the total dust mass is simply the sum of mass in each phase, the homogeneous density can be expressed as

$$\begin{aligned} \rho_{\text{hom}} &= \frac{M_c + M_{\text{icm}}}{V} \\ &= \frac{V_c M_c}{V V_c} + \frac{V_{\text{icm}} M_{\text{icm}}}{V V_{\text{icm}}} \\ &= f_c \rho_c + (1 - f_c) \rho_{\text{icm}} \\ &= (\rho_c - \rho_{\text{icm}}) f_c + \rho_{\text{icm}} , \end{aligned} \quad (7)$$

where M_c and M_{icm} are the dust masses in the clumps and ICM respectively, V_c and V_{icm} are the respective volumes, and so $\rho_c = M_c/V_c$ is the density of dust in the clumps, $\rho_{icm} = M_{icm}/V_{icm}$ the density in the ICM, and $f_c = V_c/V$ is the filling factor of the clumps. Equation (7) can be rearranged by substituting for ρ_c with $\alpha\rho_{icm}$ to give an equation for the ICM density

$$\rho_{icm} = \frac{\rho_{hom}}{(\alpha - 1)f_c + 1} . \quad (8)$$

As $f_c \rightarrow 0$, $\rho_{icm} \rightarrow \rho_{hom}$ and $\rho_c \rightarrow \alpha\rho_{hom}$ from below, whereas if $f_c \rightarrow 1$, $\rho_{icm} \rightarrow \rho_{hom}/\alpha$ and $\rho_c \rightarrow \rho_{hom}$ from above.

One possible type of two-phase clumpy medium is that of cubic clumps randomly located on a body centered cubic lattice. The construction is similar to that used in percolation theory, where the probability of lattice site occupation is equivalent to the filling factor and the clumps are then the occupied sites, and the cubic clumps do not overlap. Witt & Gordon (1996) studied radiative transfer in such a two-phase clumpy medium defined on a cubic lattice, and we repeated some of their Monte Carlo simulations giving a successful test of our methods. In this work we use spherical clumps defined on a high resolution 3D grid, allowing clump overlaps and the random locations of clumps to be chosen at a higher resolution than the clump size. In addition, the radiative transfer properties are then readily approximated by analytic formulas, as we demonstrate in §4 and §6. The stochastic media in the analytical models of Boissé (1990) and Hobson & Scheuer (1993) do not impose any restrictions on the shapes of the clumps, however, the models are developed for the case of isotropic scattering.

To construct a two-phase medium with randomly located clumps that may overlap, we must calculate the number of clumps needed to achieve the desired filling factor. This can be derived from the volume of a clump, v_c , the total volume of the medium, V , and the filling factor, f_c , but the possible occurrence of overlapping clumps complicates the calculation. Assume that the clumps are all identical. Defining the volume fraction of a single clump as

$$p \equiv \frac{v_c}{V} , \quad (9)$$

then the probability that a random point is not in any clump is equal to $(1 - p)^{N_c}$, where N_c is the number of clumps, and therefore

$$f_c = 1 - (1 - p)^{N_c} \quad (10)$$

(see Appendix B for more discussion). Equation (10) is easily solved for the total number of clumps,

$$N_c = \frac{\ln(1 - f_c)}{\ln(1 - p)} , \quad (11)$$

in terms of the total filling factor, f_c , and the single clump filling factor, p . Although the above equations apply to identical clumps of any shape, we shall consider only spherical clumps of radius r_c with $v_c = 4\pi r_c^3/3$. Given f_c , r_c , and V , the clumpy medium is constructed by calculating N_c using equations (9) and (11), then selecting N_c random points uniformly distributed in V , placing a sphere of radius r_c and density ρ_c around each point, setting the density between the spheres to ρ_{icm} , and finally discretizing the medium on a high resolution 3D grid. When the randomly located clumps do overlap, the densities are *not* summed, so the medium is always characterized by only two possible densities: that of the ICM and the clumps.

Monte Carlo simulations of radiative transfer were computed for three types of photon sources in a two-phase clumpy medium contained within a sphere of unit radius $R_S = 1$, in which the spherical clumps have radius $r_c = 0.05$ and are 100 times denser than the ICM ($\alpha = 100$). The 3D rectangular grid used to represent the medium has resolution of 127^3 voxels, so that the clump diameters are about 6 grid elements. Figures 1, 2 and 3 show our results for an array of clump filling factors and optical depths, keeping r_c and α constant. Three million photons were followed in each Monte Carlo simulation. Each of the images is the map of photons absorbed in a 2D slice (127×127 pixels) through the center of the sphere. The grey scale from black to white indicates minimum to maximum absorption, on a logarithmic scale. Figure 1 represents the case of a single central isotropic luminosity source, analogous to a star or a centrally condensed cluster of stars in an H II region. Figure 2 represents the case of isotropic photon emission distributed uniformly in the sphere, analogous to a uniform distribution of stars in a galaxy. Figure 3 represents the case of an external uniformly illuminating source of isotropic photons, analogous to cold molecular clouds illuminated by the diffuse interstellar radiation field (IRF). In all cases the dust is characterized by a scattering albedo of $\omega = 0.6$ and asymmetry parameter $g = 0.6$, which are typical values for UV photons scattering off dust grains (Gordon et al. 1994). Recall that $g = 0$ results in isotropic

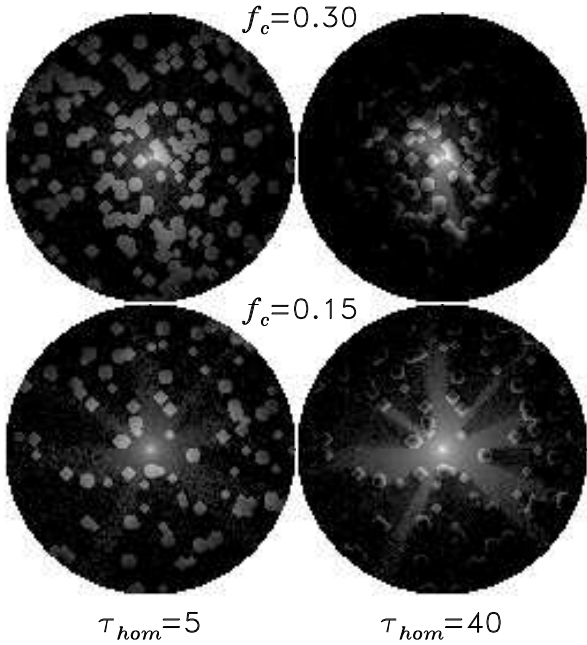


Fig. 1.— Spatial distribution of photons absorbed by dust in a two-phase clumpy medium heated by a central point source. The simulations were performed by Monte Carlo calculations, and the images depict a 2D slice through the center of the sphere. Scaling is logarithmic from the minimum of 0.1 photons (black) to the maximum of 4×10^4 photons absorbed per voxel (white). For more details see §2.2.

scattering and $g = 1$ gives forward scattering.

Moving vertically in the array of slices in the Figures corresponds to increasing the volume filling factor f_c of the clumps while keeping the total dust mass constant (in each column). Thus the number of clumps appearing in each slice increases and ρ_{icm} decreases from bottom to top. Moving horizontally increases the equivalent homogeneous optical depth of the sphere,

$$\tau_{hom} = \kappa \rho_{hom} R_S, \quad (12)$$

which is the radial optical depth of extinction (absorption plus scattering) that would result if the dust were distributed uniformly throughout the sphere instead of being clumpy. Increasing τ_{hom} can be viewed as either increasing the dust abundance (increasing ρ_{icm} and ρ_c) or changing the wavelength of the photons, either case resulting in more absorption.

For the case of a central source (Figure 1), as

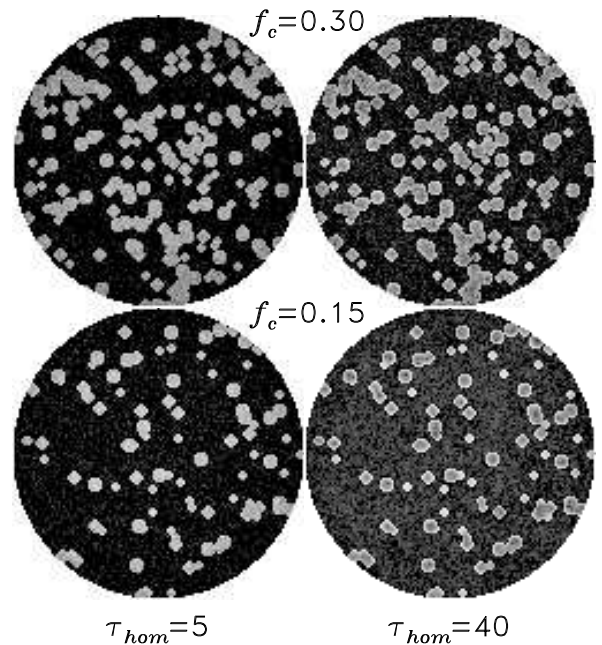


Fig. 2.— Same as Figure 1 for dust heated by a uniform distribution of internal sources. Scaling is logarithmic from the minimum of 0.1 photons (black) to the maximum of 40 photons absorbed per voxel (white). For further description see §2.2.

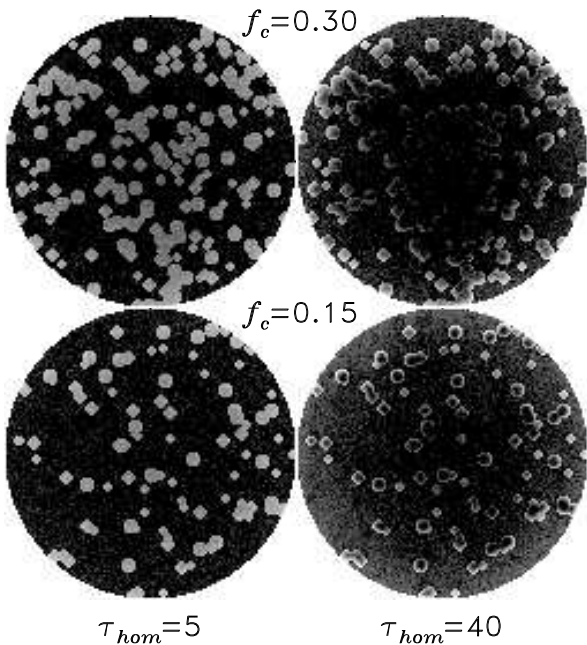


Fig. 3.— Same as Figure 1 for dust heated by an external uniformly illuminating source. Scaling is logarithmic from the minimum of 0.1 photons (black) to the maximum of 80 photons absorbed per voxel (white). For further description see §2.2.

τ_{hom} increases the ICM absorbs more photons and the clumps become opaque, creating the apparent shadows behind the clumps, when f_c is small. However scattering by the dust causes photons to go behind the clumps and become absorbed, thus diminishing the effect of what would otherwise be completely dark shadows in the case of no scattering. As the clumps become opaque ($\tau_{hom} = 40$), absorption occurs more at the clump surfaces. When f_c is increased (keeping the total dust mass constant) the effect of shadows merges into the appearance of an absorption cavity. Similar effects occur for the case of uniformly distributed sources (Figure 2), however not as dramatic as when the clumps are illuminated by a central source, since there are no shadows when the photons are emitted everywhere in the medium. At high f_c the clumps dominate the medium and absorb most of the photons. In the case of a uniformly illuminating external source (Figure 3), when τ_{hom} and f_c are large we find that most of the impacting photons are absorbed in the outer layers of the spherical region and the center is shielded from radiation. However, for small f_c the center of the sphere is less shielded and instead the clump centers are shielded, most photons being absorbed on the surfaces of the clumps. In general, the clumpy medium allows photons to penetrate farther into the spherical region than if the medium was homogeneous, and this fact was the motivation and a conclusion in the work of Boissé (1990), Hobson & Scheuer (1993), and HP93, for the case of plane-parallel slab geometry.

By observing the fraction of photons that escape in the case of a central point source we can compute the effective optical depth of the medium at a given wavelength λ as

$$\tau_S(\lambda) = -\ln\left(\frac{L_{esc}(\lambda)}{L_0(\lambda)}\right) \quad (13)$$

where $L_0(\lambda)$ is the luminosity of the central source and $L_{esc}(\lambda)$ the escaping luminosity (for simplicity we shall hereafter drop any explicit dependence on λ). We use the notation τ_S instead of τ_{eff} because τ_{eff} is reserved for the case of no scattering (absorption plus scattering considered as interaction), whereas τ_S includes the effects of scattering and is therefore dependent on the geometry of the medium, which in this case is spherical. Equation (13) is analogous to eq.(1), and it follows that $\tau_S < \tau_{eff} < \tau_{hom}$ for a clumpy medium. Figure 4 shows the behavior of τ_S as a function of τ_{hom} for three cases of f_c , with other

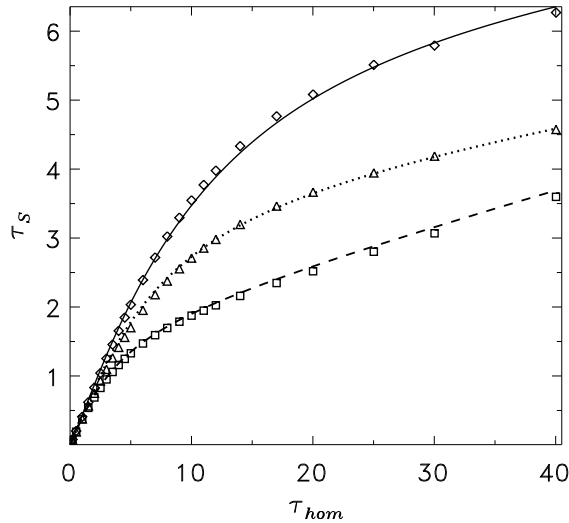


Fig. 4.— The effective optical radius, τ_S , of clumpy media in a sphere is shown as a function of the equivalent homogeneous optical depth, τ_{hom} , for three values of f_c , the clump filling factor. The symbols show τ_S given by eq.(13) using the results of Monte Carlo simulations including scattering ($\omega = 0.6$ and $g = 0.6$), with $f_c = 0.1$ (squares), 0.2 (triangles), and 0.3 (diamonds). See §2.2 for more discussion. The curves are produced by analytic approximations developed in this paper, and are discussed in §6.

parameters having the values mentioned above. The diamonds indicate results of Monte Carlo simulations when $f_c = 0.3$ (corresponding to top row in Figure 1), the triangles show $f_c = 0.2$, and the squares show $f_c = 0.1$. There are two slopes in each curve of τ_S versus τ_{hom} , corresponding to the two phases of the medium. The steeper slope at low values of τ_{hom} is due to absorption by the increasing optical depth of the clumps. As $\tau_{hom} \rightarrow \infty$ the clumps become opaque and any further increase in absorption is due to the ICM, and because it has a lower density the slope of the τ_S curves is less. The solid, dotted and dashed curves are produced by the analytic approximations presented in sections 3 and 4, and the agreement with Monte Carlo results is discussed further in §6.

3. ESCAPE AND ABSORPTION IN HOMOGENEOUS MEDIA

Since Monte Carlo simulations can require a large amount of computer time, it is useful to have analytical approximations for the basic results of radiative transfer, such as, the fraction of photons which escape a bounded medium. In this section we present such approximations for homogeneous spherical media with internal or external sources. The escape and absorption probability approximations are also compared with results of Monte Carlo simulations to assess their accuracy. These escape probability formulae are later applied to the case of clumpy media.

3.1. Central Isotropic Point Source

Consider an isotropic point source in the center of a spherical homogeneous medium. When the medium does not scatter photons the escape probability is simply $e^{-\tau}$, where $\tau = \rho\kappa R$ is the optical radius of the sphere, characterized by a radius R and a mass density ρ , and where κ is the absorption cross-section of the dust per unit mass. If the medium also scatters photons, we can construct an analytical approximation for the effective optical radius of the sphere, τ_S , defined as the negative natural logarithm of the escaping fraction of photons, as in eq.(13). The approximation formula is based on limiting cases of the optical parameters. When the optical depth of extinction (absorption and scattering), $\tau = \tau_{abs} + \tau_{scat}$, is large and the scattering is isotropic ($g \sim 0$), then theoretical analysis (Rybicky & Lightman 1979) suggests that τ_S is approximately

$$\tau_S \simeq \tau(1 - \omega)^{\frac{1}{2}}; \quad (\tau \gg 1 \text{ and } g \sim 0), \quad (14)$$

where $\omega \equiv \tau_{scat}/\tau$ is the scattering albedo. When the optical radius is small ($\tau \ll 1$) and g is any value, we expect that

$$\tau_S \simeq \tau(1 - \omega); \quad (\tau \ll 1 \text{ and any } g), \quad (15)$$

which is also an exact formula in the case of purely forward scattering at any optical depth. We can interpolate between these extreme cases using the following formula:

$$\tau_S(\tau, \omega, g) \equiv \tau(1 - \omega)^{\chi(\tau, g)}, \quad (16)$$

where the interpolation exponent is given by

$$\chi(\tau, g) \equiv 1 - \frac{1}{2} \left(1 - e^{-\tau/2}\right) (1 - g)^{\frac{1}{2}}. \quad (17)$$

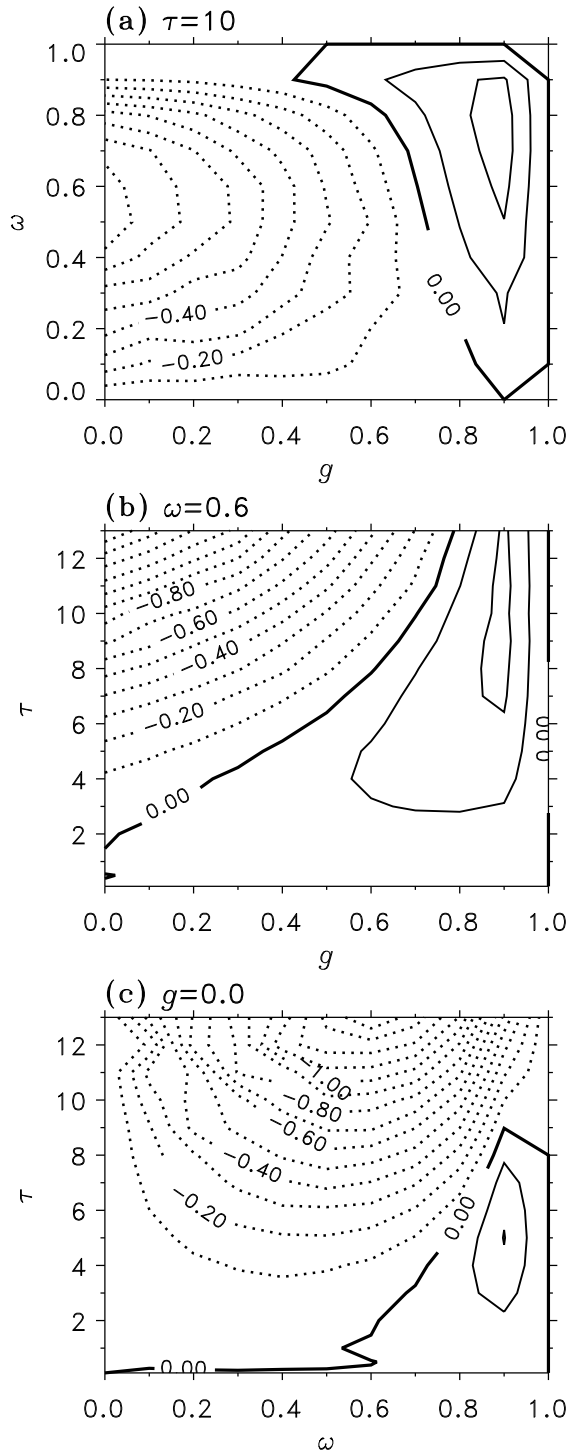


Fig. 5.— Contours show the difference between the effective optical depth of a homogeneous sphere as predicted by eq.(16) and that resulting from Monte Carlo simulations.

The probability of escaping from the homogeneous sphere is then defined as

$$\mathcal{P}_{esc}^c(\tau, \omega, g) \equiv \exp[-\tau_S(\tau, \omega, g)] \quad , \quad (18)$$

where the superscript “c” indicates that this is for a central point source.

To check this approximation, the Monte Carlo code was used to compute a 3D matrix of effective optical radii as a function of optical parameters in the ranges $0 < \tau \leq 13$ with $\Delta\tau \leq 1$, $0 \leq \omega \leq 1$ with $\Delta\omega = 0.1$, and $0 \leq g \leq 1$ with $\Delta g = 0.1$, following more than 10^6 photons in each simulation. Figure 5 shows contours of the difference between $\tau_S(\tau, \omega, g)$ given by eq.(16) and τ_S from Monte Carlo simulations. The differences are shown on 2D slices through the 3D parameter space, as a function of (a): (g, ω) with $\tau = 10$; (b): (g, τ) with $\omega = 0.6$; and (c): (ω, τ) with $g = 0$. The bold line in each panel depicts the region in parameter space where the agreement is perfect. The dotted contour lines indicate where eq.(16) gives values less than the Monte Carlo results. The worst case of the approximation occurs when $\omega = 0.6$, $g = 0$, and $\tau > 4$, as panels (b) and (c) show that $\tau_S(\tau, \omega, g)$ underestimates the Monte Carlo results by a value exceeding unity. Also, panels (a) and (c) show that eq.(14) is not always a good approximation. However the difference is relatively small compared to the value of $\tau_S \approx 10$ at $(\tau, \omega, g) = (13, 0.6, 0)$. In addition, when modeling radiative transfer through interstellar dust, isotropic scattering occurs at near-infrared (NIR) wavelengths for which the optical depth is smaller than at UV wavelengths where the scattering is more forward directed, and so the approximation is likely to be good at all wavelengths, as shown in panel (b).

3.2. Uniformly Distributed Emission

Consider a spherical homogeneous medium with a uniform distribution of isotropically emitting sources. When there is no scattering, Osterbrock (1989) derived an exact solution for the photon escape probability given by

$$P_e(\tau) \equiv \frac{3}{4\tau} \left[1 - \frac{1}{2\tau^2} + \left(\frac{1}{\tau} + \frac{1}{2\tau^2} \right) e^{-2\tau} \right] \quad (19)$$

where $\tau = \rho\kappa R$ is the optical radius of the sphere ($R =$ radius of sphere, $\rho =$ density of absorbers, and $\kappa =$ absorption cross-section). We find that $P_e(\tau)$ agrees exactly with the escaping fraction of photons

computed in Monte Carlo simulations. Using the optical depth of extinction resulting from both absorption and scattering, $\tau_{ext} = \tau_{abs} + \tau_{scat}$, we can get the probability, $P_e(\tau_{ext})$, that photons will escape the spherical medium without any interactions (absorption or scattering), and we call it the extinction escape probability. Making the assumption that the scattered photons have the same spatial and angular distribution as the emission sources, the extinction escape probability can be applied recursively to arrive at the scattering escape probability (Lucy et al. 1991)

$$\mathcal{P}_{esc}^u(\tau, \omega) \equiv \frac{P_e(\tau)}{1 - \omega[1 - P_e(\tau)]}, \quad (20)$$

where $\tau \equiv \tau_{ext}$ and $\omega = \tau_{scat}/\tau_{ext}$ is the scattering albedo. This formula estimates the effects of scattering, namely that scattered photons may eventually escape, thereby increasing the escape probability. The superscript “*u*” indicates that \mathcal{P}_{esc}^u is for uniformly distributed emitters in a sphere. Actually, $P_e(\tau)$ in the formula can be any extinction escape probability for any geometry, but this paper will concentrate on the case of spherical geometry, for which eq.(19) applies. The derivations of equations (19) and (20) are reviewed in Appendix C.

Equations (19) and (20), which we shall call the Osterbrock-Lucy escape probability (OLEP) formula, were tested extensively against Monte Carlo radiative transfer simulations with multiple scattering and found to be a reasonable approximation of the fraction of photons escaping from a spherical homogeneous medium. Since the scattering asymmetry parameter, $g = \langle \cos \theta_{scat} \rangle$, does not enter into the formula for $\mathcal{P}_{esc}^u(\tau, \omega)$, the value of g for which the OLEP formula agrees exactly with Monte Carlo simulations is found to depend on the extinction optical depth τ . The top panel in Figure 6 shows contours of the percent relative difference between the OLEP formula and escaping fraction of photons found by Monte Carlo calculations (following 10^6 photons in each simulation), as a function of g and τ , when the albedo is $\omega = 0.7$. The values of g for which the OLEP agrees with Monte Carlo results are indicated by the zero contour level drawn with a thick solid line. The dotted contours indicate where the escape probability formula underestimates the escaping fraction, and the thin solid contours indicate where it overestimates the escaping fraction. For optically thin situations ($\tau < 1$) the OLEP formula agrees well with the Monte Carlo simulations for all values of g , with the best agree-

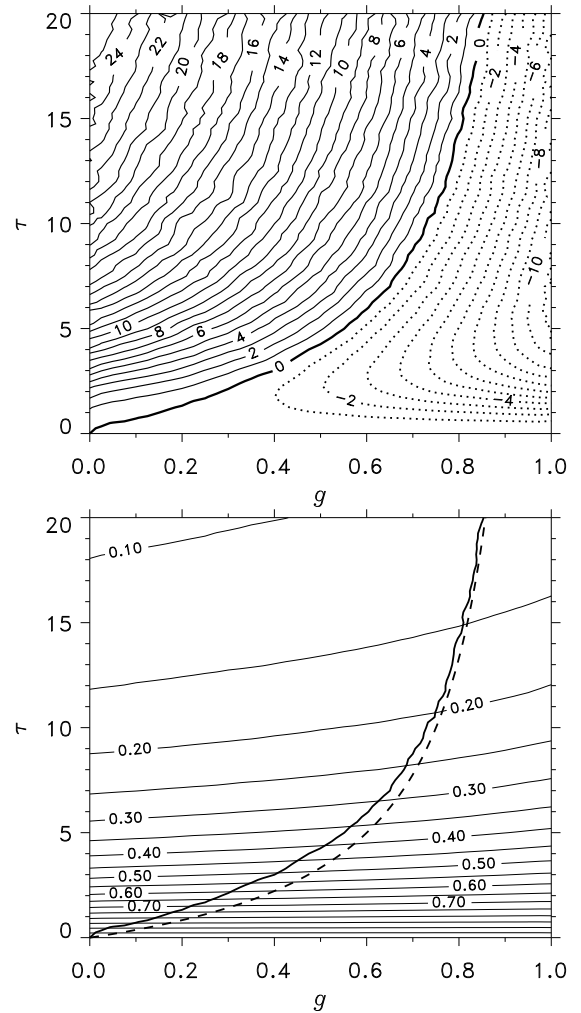


Fig. 6.— Analysis of the escaping fraction of photons that are emitted by sources uniformly distributed in a homogeneous sphere, as a function of the scattering asymmetry parameter g , and τ , the extinction optical radius of the sphere, with albedo $\omega = 0.7$. The top panel shows contours of the percent relative difference between the escaping fraction given by the OLEP formula [eqs.(19) and (20)] and that predicted by Monte Carlo simulations. The bottom panel shows contours labeled with the escaping fraction predicted by Monte Carlo simulations, over-plotted with the zero difference contour (thick solid line) from the top graph, referred to as $g^*(\tau)$. The dashed line is an approximation of $g^*(\tau)$ given by eq.(21).

ment occurring when the scattering is nearly isotropic ($g \sim 0$). As the optical depth increases the agreement shifts toward more forward scattering cases ($g \rightarrow 1$) of the Monte Carlo simulations. The maximum relative difference in the range shown is 26% overestimation at $\tau = 20$, $\omega = 0.7$, and $g = 0$, where the escaping fraction is only 0.10. The behavior of the relative difference is similar for other values of the albedo, and always decreases with albedo, to zero as $\omega \rightarrow 0$, since then $\mathcal{P}_{esc}^u(\tau, \omega) \rightarrow P_e(\tau)$. The value of g for which $\mathcal{P}_{esc}^u(\tau, \omega)$ agrees with Monte Carlo calculations (the zero difference contour) is found to be a function of optical depth only, independent of the albedo ω , and so we designate this special value by $g^*(\tau)$.

The bottom panel in Figure 6 shows contours labeled with the escaping fraction resulting from the Monte Carlo calculations, and the thick solid line is again $g^*(\tau)$, the zero difference contour from the top panel. We find that a reasonable empirical approximation for $g^*(\tau)$ is given by

$$g^*(\tau) \simeq 1 - \frac{3.3}{\tau + 3.3} \quad , \quad (21)$$

as shown by the dashed line.

There is a simple explanation for why the best agreement between $\mathcal{P}_{esc}^u(\tau, \omega)$ and Monte Carlo simulations occurs at a value of g which approaches unity as $\tau \rightarrow \infty$. To explain this fact we rewrite eq.(20) to read

$$\mathcal{P}_{esc}^u(\tau, \omega) = \frac{1}{\omega + (1 - \omega)/P_e(\tau)} \quad , \quad (22)$$

where $P_e(\tau)$ is the extinction escape probability from a sphere given by eq.(19). As $\tau \rightarrow \infty$ the extinction escape probability approaches zero as $P_e(\tau) \sim 3/4\tau$. Applying this limiting behavior to eq.(22) gives

$$\mathcal{P}_{esc}^u(\tau, \omega) \sim \frac{1}{\omega + 4\tau(1 - \omega)/3} \sim \frac{3}{4\tau(1 - \omega)} \quad , \quad (23)$$

since the term $4\tau(1 - \omega)/3 \gg \omega$ as $\tau \rightarrow \infty$. Now we recognize that $\tau(1 - \omega)$ is exactly the optical depth in the case of purely forward scattering, when $g = 1$, since then scattering acts like a reduction in absorption. The forward scattering escape probability is then exactly $P_e[\tau(1 - \omega)]$, which has the same limiting behavior as eq.(23) when $\tau \rightarrow \infty$:

$$P_e[\tau(1 - \omega)] \sim \frac{3}{4\tau(1 - \omega)} \quad . \quad (24)$$

Therefore as $\tau \rightarrow \infty$ the OLEP approximation approaches from below the exact escape probability for

purely forward scattering:

$$\mathcal{P}_{esc}^u(\tau, \omega) \rightarrow P_e[\tau(1 - \omega)] \quad . \quad (25)$$

Since the left side is valid at $g = g^*(\tau)$ and the right side is valid at $g = 1$, the limiting behavior implies that $g^*(\tau) \rightarrow 1$ as $\tau \rightarrow \infty$, which is satisfied by the approximation equation (21).

In summary, $\mathcal{P}_{esc}^u(\tau, \omega)$ overestimates the actual escape probability when $g < g^*(\tau)$ and underestimates it when $g > g^*(\tau)$. For values of g in the range $g^*(\tau) < g < 1$ the escape probability approximation can be improved by linear interpolation in g between the values $\mathcal{P}_{esc}^u(\tau, \omega)$ at $g^*(\tau)$ and $P_e[\tau(1 - \omega)]$ at $g = 1$. If an analytical approximation for the escape probability when $g = -1$ (purely backward scattering) were known, then three point parabolic interpolation could be used to obtain a very good approximation to the actual escape probability for all g , and hence all (τ, ω, g) . When modeling absorption and scattering by dust, large optical depths usually occur at UV wavelengths for which the scattering by dust tends to be more forward oriented, having values of g near $g^*(\tau)$, so the error incurred by using the OLEP approximation may be relatively small.

3.3. Finite Number of Uniformly Distributed Point Sources

The question arises as to whether the escape probability formula can be successfully applied to a discrete collection of randomly placed isotropic point sources (“stars”) instead of a continuous uniform distribution of emitters, and in particular what is the minimum number of stars for which the escape probability formula gives correct results. To answer these questions we performed Monte Carlo simulations for cases of 2 to 80 randomly placed “stars” in a homogeneous sphere, and for each case we simulated 200 trials, where in each trial 10^5 photons were followed to find the fraction that eventually escapes. The results are shown in Figure 7 for when the optical radius of the sphere is $\tau = 5$, for the case (a) of no scattering ($\omega = 0$) and case (b) with scattering ($\omega = 0.6$ and $g = 0.6$). The horizontal lines in cases (a) and (b) are the escape probabilities $P_e(\tau)$ and $\mathcal{P}_{esc}^u(\tau, \omega)$, respectively, given by equations (19) and (20). Each diamond symbol shows the average escaping fraction of the Monte Carlo trials for a fixed number of stars, and the error bars are plus and minus one standard deviation from the average value. The distribution of escaping fractions from the Monte Carlo trials is

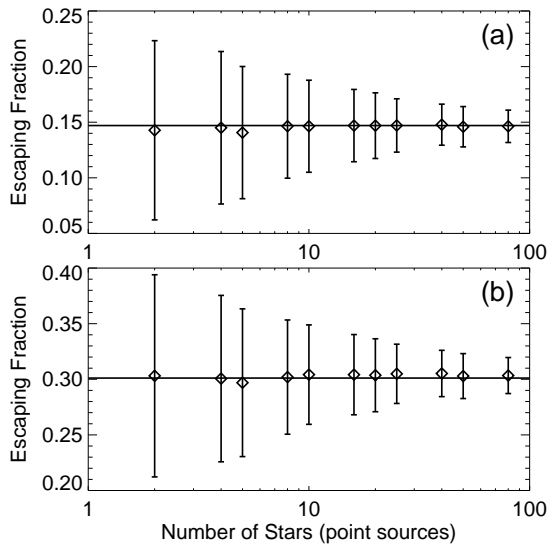


Fig. 7.— Monte Carlo simulations of the fraction of photons that escape from a homogeneous sphere of dust after being emitted by a small number of point sources (“stars”), as indicated on the horizontal axes. Case (a) is for absorption only ($\omega = 0$), case (b) is with scattering ($\omega = 0.6$ and $g = 0.6$), and the optical radius of the sphere is $\tau = 5$ in both cases. The diamonds and error bars are each the means and standard deviations of 200 Monte Carlo simulations. The solid horizontal lines are predictions by the OLEP formula. The figure is discussed in §3.3.

approximately Gaussian. We find that the standard deviation of the trials goes as the inverse square root of the number of stars n_s , as expected for sums of random variables, and in particular $\sigma \sim 0.1 (n_s)^{-0.5}$ for all $\tau > 1$. Since the escaping fraction in the case of no scattering behaves as $P_e(\tau) \sim 3/4\tau$ when $\tau \rightarrow \infty$, the expected relative deviation (σ/P_e) in the escaping fraction of photons from n_s stars randomly located in a sphere of optical depth $\tau \gg 1$ will be approximately $0.133 \tau n_s^{-0.5}$ for the case of absorption only, and less when scattering is also involved. Thus the number of stars must increase as the square of the optical depth to maintain the same expected relative deviations. The analytic escape probability agrees well with the average escaping fraction found for each group of Monte Carlo trials, it is just a question of what relative deviation is acceptable.

3.4. Uniformly Illuminating External Source

In this section we introduce approximations for the probability that externally emitted isotropic photons will interact with and get absorbed by a homogeneous medium contained in a sphere. The term interaction includes both absorption and scattering events. Given that a distribution of photons encounters the sphere at a random impact parameters, the probability of interaction at any location inside the sphere is

$$P_i(\tau) = 1 - \frac{1}{2\tau^2} + \left(\frac{1}{\tau} + \frac{1}{2\tau^2}\right) e^{-2\tau}, \quad (26)$$

where $\tau = \rho\kappa R$ is the extinction optical radius of the sphere. This equation is derived by averaging the transmission over all possible impact parameters and computing the ratio of net absorption versus impacting flux, using the same techniques as for the derivation of eq.(19) (see Appendix C). When $\tau \ll 1$ we have $P_i(\tau) \sim 4\tau/3$, which is the optical path length through a sphere averaged over all impact parameters. Equation (26) was utilized by Neufeld (1991) and Hobson & Padman (1993) in their models for clumpy media, as we shall discuss in §4.1. Note that equations (26) and (19) are related by

$$P_i(\tau) = \frac{4\tau}{3} P_e(\tau) \quad , \quad (27)$$

giving a duality between absorption (interaction) of an external source and escape (non-interaction) of an internal source.

If the medium scatters photons, we would like to know what fraction of $P_i(\tau)$, the interacting frac-

tion, will eventually escape due to multiple scattering events, and thus determine what fraction of photons are actually absorbed. In the special case of purely forward scattering there is an exact formula for the absorbed fraction of photons. When the scattering deflection angle is always zero, it is equivalent to no scattering with a reduced optical depth equal to $\tau(1 - \omega)$, where ω is the scattering albedo. So the actual fraction of photons absorbed in the purely forward scattering case is

$$\mathcal{P}_{abs}^x(\tau, \omega; g = 1) \equiv P_i[\tau(1 - \omega)] \quad , \quad (28)$$

where the superscript “ x ” indicates that this is for the case of an external source and g is the scattering asymmetry parameter. As expected, equations (26) and (28) agree exactly with Monte Carlo simulations.

For non-forward scattering cases, when $g < 1$, we can use the methods discussed in §3.2 for the case of internal uniformly distributed emitters, namely the OLEP equations (19) and (20). Given that photons interact with the medium inside the sphere, the probability that they scatter is simply ω . These scattering events can be regarded as re-emitted photons, and assuming that they are approximately uniformly distributed in the sphere, the scattered photons have a probability $\mathcal{P}_{esc}^u(\tau, \omega)$ of escaping [eq.(20)]. The fraction of the interacting photons which actually get absorbed is then $1 - \omega\mathcal{P}_{esc}^u(\tau, \omega)$. Thus an approximation for the fraction of photons absorbed is

$$\mathcal{P}_{abs}^x(\tau, \omega) \equiv P_i(\tau) [1 - \omega\mathcal{P}_{esc}^u(\tau, \omega)] \quad . \quad (29)$$

Recall that $\mathcal{P}_{esc}^u(\tau, \omega)$ is valid only for $g = g^*(\tau)$ as discussed in §3.2, and so we expect $\mathcal{P}_{abs}^x(\tau, \omega)$ to follow the same pattern. When τ_c is large, the penetration depth of photons decreases so they will not be uniformly distributed in the sphere, as assumed above, but this does not severely affect the application the approximation as we show next.

The top panel in Figure 8 shows contours of the percent relative difference between $\mathcal{P}_{abs}^x(\tau, \omega)$ and absorbed fraction of photons found by Monte Carlo calculations, as a function of g and τ , for $\omega = 0.7$. The values of g for which eq.(29) agrees with Monte Carlo results are indicated by the zero contour level drawn with a thick solid line. The dotted contours indicate where the absorption probability formula (29) underestimates the absorbed fraction, and the thin solid contours indicate where it overestimates. The difference is small and independent of g for optically

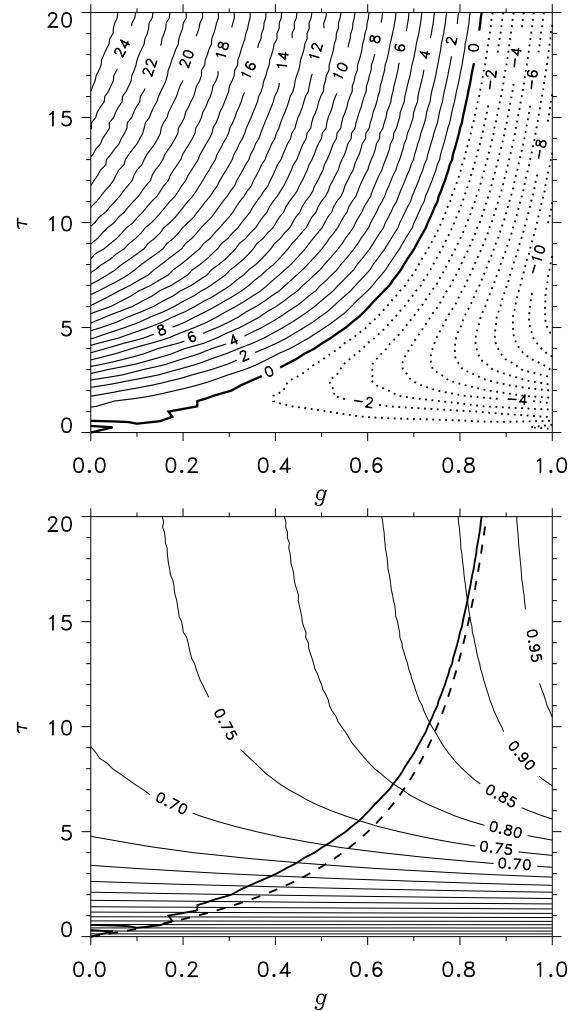


Fig. 8.— Analysis of the absorbed fraction of photons from an external source which uniformly illuminates a homogeneous sphere, when the scattering albedo is $\omega = 0.7$. The top panel shows the percent relative difference between the absorption probability given by eq.(29) and the absorbed fraction found by Monte Carlo simulations, as a function of the asymmetry parameter g , and τ , the extinction optical radius of the sphere. The contours in the bottom panel are labeled with the absorbed fractions computed by Monte Carlo simulations. The thick solid line is the locus of agreement between \mathcal{P}_{abs}^x [eq.(29)] and Monte Carlo simulations (zero difference contour from top graph), referred to as $g^*(\tau)$. The dashed line is an approximation of $g^*(\tau)$ given by eq.(21).

thin situations ($\tau < 1$), and as the optical depth increases the agreement shifts toward more forward scattering cases ($g \rightarrow 1$) of the Monte Carlo simulations. Not surprisingly, the behavior of the relative difference contours is identical to that in Figure 6 of §3.2, since we are using $\mathcal{P}_{esc}^u(\tau, \omega)$ in the formula. The relative difference decreases as $\omega \rightarrow 0$, since then $\mathcal{P}_{abs}^x(\tau, \omega) \rightarrow P_i(\tau)$ and $P_i(\tau)$ is an exact formula.

The bottom panel in Figure 8 shows contours labeled with values of the absorbed fraction obtained from Monte Carlo simulations of a uniformly illuminating isotropic external source. Comparison with Figure 6 shows that the behavior of the absorbed fraction of an external source is quite different from the absorbed fraction of an internal source (one minus the escaping fraction shown in bottom panel of Figure 6). Note that for $g < 1$, as $\tau \rightarrow \infty$ the absorbed fraction tends asymptotically toward a constant value, since in the opaque limit scattering occurs at the surface of the sphere. The thick solid line is again the contour of zero difference between $\mathcal{P}_{abs}^x(\tau, \omega)$ and Monte Carlo simulations, and the dashed line is the approximation of $g^*(\tau)$ given by eq.(21). This zero difference contour is found to be independent of ω and fit well by eq.(21), also because $\mathcal{P}_{esc}^u(\tau, \omega)$ is used in the approximation formula.

Let us now examine the behavior of the absorption probability as $\tau \rightarrow \infty$ to show in more detail why the best agreement with Monte Carlo simulations occurs at a value of g which approaches unity. Using eqs.(27) and (20), and defining $P \equiv P_e(\tau)$ for convenience, eq.(29) can be rewritten as

$$\begin{aligned} \mathcal{P}_{abs}^x(\tau, \omega) &= \frac{4\tau}{3} P \left[1 - \frac{\omega P}{1 - \omega(1 - P)} \right] \\ &= \frac{4\tau}{3} P \left[\frac{1 - \omega}{1 - \omega(1 - P)} \right] \\ &= \frac{4\tau(1 - \omega)}{3} \left[\frac{P}{1 - \omega(1 - P)} \right] \\ &= \frac{4\tau(1 - \omega)}{3} \mathcal{P}_{esc}^u(\tau, \omega), \end{aligned} \quad (30)$$

thus extending eq.(27), the duality between the cases of internal and external sources, to the case of $\omega > 0$. Equation (28) can be rewritten as

$$\mathcal{P}_{abs}^x(\tau, \omega; g = 1) = \frac{4\tau(1 - \omega)}{3} P_e[\tau(1 - \omega)] \quad (31)$$

where we have used eq.(27) again. The analysis given by eqs.(23-25) proved that $\mathcal{P}_{esc}^u(\tau, \omega) \rightarrow P_e[\tau(1 - \omega)]$

from below as $\tau \rightarrow \infty$, thereby proving that

$$\mathcal{P}_{abs}^x(\tau, \omega; g = g^*) \rightarrow \mathcal{P}_{abs}^x(\tau, \omega; g = 1) \quad (32)$$

from below, implying that $g^*(\tau) \rightarrow 1$ as $\tau \rightarrow \infty$.

4. ESCAPE AND ABSORPTION IN CLUMPY MEDIA

A viable approach to the problem of estimating the escaping and absorbed fractions of photons in an inhomogeneous medium is to find effective values for the absorption and scattering properties of the inhomogeneous medium and then use these effective values in the escape/absorption probability formulae that were developed for homogeneous media. The work of Hobson & Padman (1993) (HP93) provides the means to such an approach for two-phase clumpy media by a model they called the ‘‘mega-grains’’ approximation, which reduces the inhomogeneous radiative transfer problem to an effectively homogeneous one. In the following sections we review the mega-grains approximation, and then discuss how it is utilized to give escape/absorption probability approximations for clumpy media. We also introduce some improvements to the mega-grains approximation of HP93. In addition, we present new formulae giving the approximate fraction of photons absorbed in each phase of the medium, which can then be used to estimate the dust temperature and infrared emission from the clumps and ICM separately.

4.1. The Mega-Grains Approximation

Natta & Panagia (1984) developed analytic approximations for the extinction by dust having various kinds of inhomogeneous distributions, in particular, a clumpy distribution with an empty interclump medium (ICM). Neufeld (1991) proposed the approach of treating spherical clumps in a two-phase medium as large grains, and applied it to the special case of the scattering, absorption, and escape of Ly α radiation, involving both gas and dust. HP93 proposed a more general set of formulae called the mega-grains approximation, which also treats the spherical clumps as large grains but with absorption and scattering coefficients in direct analogy with dust grains. Their mega-grains model gives equations for the effective optical depth and effective scattering albedo of a two-phase clumpy medium, with a non-empty ICM. In this section we review the derivation of

the mega-grains approximation and introduce an improved equation for the effective scattering albedo. We also develop a new approximate formula for the effective scattering asymmetry parameter of the clumpy medium. To distinguish between similar properties of the clumps (mega-grains) and the dust we will assign them the subscripts “c” and “d”, respectively. So ω_c will be the macroscopic albedo of the clumps and ω_d is the microscopic albedo of the dust. Also, an implicit dependence on wavelength is assumed in all the following.

4.1.1. Effective Optical Depth

Assume that a collection of spherical clumps, each of radius r_c and having dust mass density ρ_c , are randomly distributed in an inter-clump medium (ICM) having a constant dust mass density of $\rho_{icm} \leq \rho_c$. Following HP93, define the clump optical radius

$$\begin{aligned} \tau_c &= (\rho_c - \rho_{icm}) \kappa r_c \\ &= (\alpha - 1) \kappa \rho_{icm} r_c \end{aligned} \quad (33)$$

where κ is the total absorption plus scattering cross-section of the dust grains per unit mass and recall that $\alpha = \rho_c / \rho_{icm}$. The reason for the subtraction of densities in this definition is to disregard the clumps in the limit of when the clump density approaches the density of dust in the ICM, since then there are effectively no clumps. Thus the mega-grains are considered to be just the over-density, $\rho_c - \rho_{icm}$, allowing for analysis as a separate component superimposed on a continuous medium of lower density. Now considering the clumps as large grains, the probability that a randomly emitted photon will encounter a clump is just πr_c^2 . Once a clump is encountered, the probability that the photon will interact (get absorbed or scatter) with dust in clump is $P_i(\tau_c)$, given by eq.(26), the interaction probability for a sphere of optical radius τ_c . Then we can define the interaction coefficient per unit length, Λ_{mg} , in the medium for just the mega-grains as

$$\Lambda_{mg} = n_c \pi r_c^2 P_i(\tau_c) \quad (34)$$

where n_c is the number of clumps per unit volume. Here the use of the interaction probability $P_i(\tau_c)$ is analogous to the absorption and scattering efficiency coefficient of dust grains.

Define the effective interaction coefficient per unit length, Λ_{eff} , in the two-phase clumpy medium by including the ICM:

$$\Lambda_{eff} = \Lambda_{mg} + \kappa \rho_{icm} \quad (35)$$

This reduces to the interaction coefficient for a homogeneous medium, $\kappa \rho_{hom}$, when $\alpha = \rho_c / \rho_{icm} = 1$ or $f_c = 0$, i.e. when the medium is homogeneous [see eqs.(7) & (8)]. For a clumpy medium in a plane-parallel slab of thickness L , or sphere of radius $R = L$, the effective optical depth is then

$$\tau_{eff} = L \Lambda_{eff} = L \Lambda_{mg} + L \kappa \rho_{icm}, \quad (36)$$

where by effective we mean the optical depth corresponding to the average transmission of a large collection of randomly chosen paths through the slab, as expressed by eq.(1). In §4.2 we analyze in more detail the implementation of the mega-grains equation (34), developing an improved version, and discuss the behavior of τ_{eff} as a function of all the parameters characterizing the clumpy medium. Equation (34) is compared with the approximation developed by Natta & Panagia (1984) in §4.3.

4.1.2. Effective Scattering Albedo

The effective scattering albedo of the two-phase clumpy medium is logically defined as a weighted combination of the albedos for each phase in the medium:

$$\omega_{eff} \equiv \frac{\omega_c \Lambda_{mg} + \omega_d \kappa \rho_{icm}}{\Lambda_{eff}}, \quad (37)$$

where ω_d is the albedo of the dust and ω_c is the effective albedo of a clump, which we discuss below. First note that in the limit as the medium becomes homogeneous ($f_c \rightarrow 0$) we have $\Lambda_{mg} \rightarrow 0$ and $\Lambda_{eff} \rightarrow \kappa \rho_{icm}$, so then $\omega_{eff} \rightarrow \omega_d$ as expected.

Given that interactions with dust in a clump have occurred for a group of photons, the effective albedo of the clump is the fraction of those photons that manage to eventually escape from the clump by means of multiple scattering. HP93 suggested an approximation for the clump albedo for which we shall use the symbol ω_c^{HP} :

$$\omega_c^{HP} \equiv \frac{\omega_d}{1 + (1 - \omega_d) 4\tau_c/3}, \quad (38)$$

where τ_c is the optical radius of a clump as given by eq.(33). As $\tau_c \rightarrow 0$ we have $\omega_c^{HP} \rightarrow \omega_d$ as required. As $\tau_c \rightarrow \infty$ then $\omega_c^{HP} \rightarrow 0$, but this cannot be generally true since we expect always some backscattering from the surface layer of the clump as long as the dust scattering asymmetry parameter $g_d < 1$. Note that the approximation does not consider the distribution of scattering angles. In addition we shall show

that for small τ_c , equation (38) is below the minimum possible value for the clump albedo.

Let us examine the special case of purely forward scattering, when the asymmetry parameter of the dust is $g_d = 1$. In this case there is an exact formula for the clump albedo. The forward scattering case for photons randomly impacting a spherical clump was discussed previously in the presentation of equations (26) and (28), and the actual fraction of photons absorbed is $P_i[\tau_c(1 - \omega_d)]$. The fraction which escapes is then $P_i(\tau_c) - P_i[\tau_c(1 - \omega_d)]$, and the ratio of escaping fraction over interacting fraction is the clump albedo:

$$\omega_c^1 = \frac{P_i(\tau_c) - P_i[\tau_c(1 - \omega_d)]}{P_i(\tau_c)} \quad (39)$$

where the superscript “1” indicates that $g_d = 1$. As $\tau_c \rightarrow 0$, we have $P_i(\tau_c) \rightarrow 4\tau_c/3$ and then

$$\begin{aligned} \omega_c^1 &\rightarrow \frac{4\tau_c/3 - 4\tau_c(1 - \omega_d)/3}{4\tau_c/3} \\ &= 1 - (1 - \omega_d) = \omega_d \end{aligned}$$

reaching the correct limit. On the other hand, if $\tau_c \rightarrow \infty$ then $\omega_c^1 \rightarrow 0$, which is expected in this case of purely forward scattering. We shall show that ω_c^1 is the minimum clump albedo over all $-1 \leq g_d \leq 1$.

To determine the actual clump albedo and how it depends on dust scattering parameters we performed Monte Carlo simulations of photons randomly impacting a spherical clump for many values of the optical parameters in the ranges of $0 < \tau_c \leq 25$, $0 < \omega_d < 1$, and $0 \leq g_d \leq 1$. The fraction of photons which interact with the clump is found to be exactly given by eq.(26), as expected. Of these interacting photons, the fraction that scatters and eventually escapes from the clump is the clump albedo ω_c . Figure 9 shows ω_c versus τ_c for three values of the dust albedo $\omega_d = 0.3, 0.6$, and 0.8 (apparent when $\tau_c = 0$). The square symbols indicate the case of $g_d = 0$ (isotropic scattering), the diamonds show $g_d = 1$ (forward scattering), and intermediate values of $0 < g_d < 1$ at increments of 0.1 are plotted as dots vertically connecting the squares and diamonds. The dotted line is ω_c^1 given by eq.(39), the dashed line is ω_c^{HP} given by eq.(38), and the solid line we shall introduce shortly. Clearly, the theoretical forward scattering clump albedo, ω_c^1 (dotted line), agrees exactly with the Monte Carlo results for $g_d = 1$ (diamond symbols), as expected, and is a lower bound on the

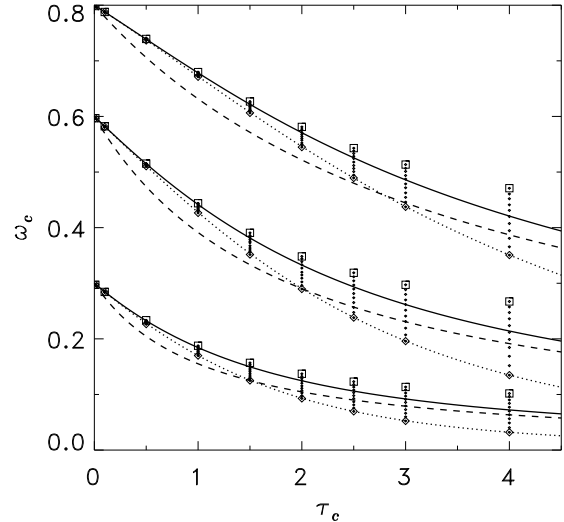


Fig. 9.— Comparison of theoretical approximations for the clump albedo given by HP93, [ω_c^{HP} of eq.(38), dashed line], and those developed in this paper, ω_c^* [eq.(40), solid line] and ω_c^1 [eq.(39), dotted line], with Monte Carlo simulations (squares for $g_d = 0$, diamonds for $g_d = 1$), as a function of the clump optical depth τ_c .

clump albedo. From the dashed line it is apparent that $\omega_c^{HP} < \omega_c^1$ when $\tau_c < 2$, which violates the lower bound.

Another formula for the clump albedo can be derived using the OLEP formula [eqs. (19) and (20)] in the same manner as was discussed in the derivation of equation (29). Given that a photon interacts with the dust inside a clump, the probability that it scatters is just ω_d . These scattering events can be regarded as re-emitted photons, and assuming that they are approximately uniformly distributed in the clump, they have a probability $\mathcal{P}_{esc}^u(\tau_c, \omega_d)$ of escaping, thus obtaining the clump albedo

$$\omega_c^* = \omega_d \mathcal{P}_{esc}^u(\tau_c, \omega_d) \quad , \quad (40)$$

which gives the solid line shown in Figure 9. The escape probability equation (20) for $\mathcal{P}_{esc}^u(\tau_c, \omega_d)$ can be rearranged to give

$$\omega_c^* = \frac{\omega_d}{\omega_d + (1 - \omega_d) / P_e(\tau_c)} \quad (41)$$

where $P_e(\tau_c)$ is the extinction escape probability, as given by eq.(19). As $\tau_c \rightarrow 0$, we have $P_e(\tau_c) \rightarrow 1$ and so $\omega_c^* \rightarrow \omega_d$, because after a single scattering a photon will most likely escape an optically thin clump. As $\tau_c \rightarrow \infty$, we have $P_e(\tau_c) \rightarrow 3/4\tau_c$ and then $\omega_c^* \rightarrow 0$. However, ω_c^* gives the actual clump albedo for a single value of g_d for each τ_c , and this value, $g_d^* = g^*(\tau_c)$, is approximately given by eq.(21), since we are using the approximate escape probability $\mathcal{P}_{esc}^u(\tau_c, \omega_d)$ (see Figure 6). Therefore the fact that $\omega_c^* \rightarrow 0$ as $\tau_c \rightarrow \infty$ is just a consequence of the fact that $g^*(\tau_c) \rightarrow 1$ as $\tau_c \rightarrow \infty$, coupled with the fact that the exact equation (39) for the case of $g_d = 1$ gives the limit of zero for the albedo of increasingly opaque clumps.

The clump albedo depends more strongly on g_d as τ_c increases (see Figure 9), creating a large spread in the values of ω_c between the cases of forward scattering ($g_d = 1$, diamonds) and isotropic scattering ($g_d = 0$, squares). This is because as τ_c increases the average photon penetration depth to first scattering decreases, and then forward scattered photons are likely to be absorbed in the clump whereas the spherical geometry presents many opportunities for the escape of any non-forward scattered photon.. Thus a higher probability of backscattering, corresponding to smaller values of g_d , increases the probability that a photon will escape, giving a larger effective clump albedo. For any $g_d < 1$ our Monte Carlo simulations indicate that the albedo of increasingly opaque clumps ($\tau_c > 20$) remains non-zero.

In summary, Figure 9 compares the theoretical approximations for the clump albedo developed in this paper, ω_c^* [solid line, eq.(41)], ω_c^1 [dotted line, forward scattering, eq.(39)], with the approximation given by HP93, ω_c^{HP} [dashed line, eq.(38)], and with the Monte Carlo results (symbols). From the figure it is clear that $\omega_c^* > \omega_c^{HP}$ and $\omega_c^* > \omega_c^1$ for all clump optical depths, and for $\tau_c < 2$ our proposed eq.(41) for ω_c^* does better at predicting the clump albedo computed by Monte Carlo than ω_c^{HP} given by eq.(38). We shall assume that ω_c^* given by eq.(41) is a sufficiently good approximation of the actual clump albedo, and will use it in eq.(37) to obtain the effective albedo of the clumpy medium. If $g^*(\tau_c) \leq g_d \leq 1$, one can interpolate in the variable g_d between values ω_c^* and ω_c^1 corresponding to the endpoints of the range to obtain a more accurate estimate of the clump albedo.

4.1.3. Effective Scattering Asymmetry Parameter

Hobson and Padman did not consider the angular scattering distribution of photons in their paper introducing the mega-grains approximation, but a similar approach as used for the effective albedo of the clumpy medium can be followed. We define the effective phase function asymmetry parameter for the two-phase clumpy medium as a weighted combination of the asymmetry parameters of each phase in the medium:

$$g_{eff} \equiv \frac{g_c \Lambda_{mg} + g_d \kappa \rho_{icm}}{\Lambda_{eff}} \quad , \quad (42)$$

where g_d is the asymmetry parameter of the dust and g_c is the clump scattering asymmetry parameter, which we discuss below. Note that $g_{eff} \rightarrow g_d$ as the medium becomes homogeneous ($f_c \rightarrow 0$), since then $\Lambda_{mg} \rightarrow 0$ and $\Lambda_{eff} \rightarrow \kappa \rho_{icm}$.

Let us assume that a collection of photons enter a clump with parallel ray paths, are scattered by the dust in the clump, and eventually escape from the clump. How does the exiting angular distribution depend on the dust scattering properties and the optical depth of the clump? The results of our Monte Carlo simulations shown in Figure 10 answer this question. We computed $g_c = \langle \cos \theta_{exit} \rangle$ for all simulations, where θ_{exit} is the exiting angle respect to the entering parallel rays, and plot g_c versus the clump optical radius τ_c , for values of $g_d = \{-0.4, 0.0, 0.6, 0.9\}$ (evident when $\tau_c = 0$), and albedos $0.1 \leq \omega_d \leq 0.9$. The square symbols are for when $\omega_d = 0.1$, the diamonds for $\omega_d = 0.9$, and intermediate values of ω_d in

increments of 0.1 are plotted as dots connecting the squares and diamonds. The distribution of exit angles does not actually follow the HG phase function with $g = g_c$, since the scattering is complicated by the spherical geometry, however, the HG phase function is a reasonable approximation. In the case of forward scattering ($g_d > 0$), the clump scattering distribution becomes more isotropic as the optical radius τ_c of the clump increases and as the dust albedo ω_d increases. If $g_d = 0$ (isotropic scattering by dust), then as the clump becomes opaque the clump asymmetry parameter approaches a backscattering distribution of $g_c = -1/3$ independent of the dust albedo. In addition, when $|g_d|$ is near zero and τ_c is large, it is apparent that g_c approaches $-1/3$ as ω_d increases. Our computations of g_c agree with the three cases computed and mentioned by Code & Whitney (1995).

The solid lines in Figure 10 are produced by the following empirical formula:

$$g_c(\tau_c, \omega_d, g_d) = g_d - C \left(1 - \frac{1 + e^{-B/A}}{1 + e^{(\tau_c - B)/A}} \right) \quad (43)$$

where

$$\begin{aligned} A &\equiv 1.5 + 4g_d^3 + 2\omega_d\sqrt{g_d}\exp(-5g_d) \\ B &\equiv 2 - g_d(1 - g_d) - 2\omega_d g_d \\ C &\equiv \frac{1}{3 - \sqrt{2g_d} - 2\omega_d g_d(1 - g_d)}. \end{aligned}$$

The formula is a good approximation of the Monte Carlo results when $g_d \geq 0$. For g_d slightly negative one can shift the $g_d = 0$ curve downward to get an approximation of g_c , or just use $g_c = g_d$ when $g_d < -0.2$. The exact value of g_c is of importance mainly for the case of a central point source, since the escaping fraction is then very sensitive to the distribution of angular scattering.

4.2. The Extended Mega-Grains Approximation

The mega-grains approximation as presented by Hobson & Padman is limited to small values of the clump filling factor. In addition, we found that for optically thin situations it predicts an effective optical depth which is slightly greater than the equivalent homogeneous optical depth, in violation of eq.(3). In this section we develop an improved version of the mega-grains approximation that resolves these problems, and extends the approximation to all values of the clump filling factor.

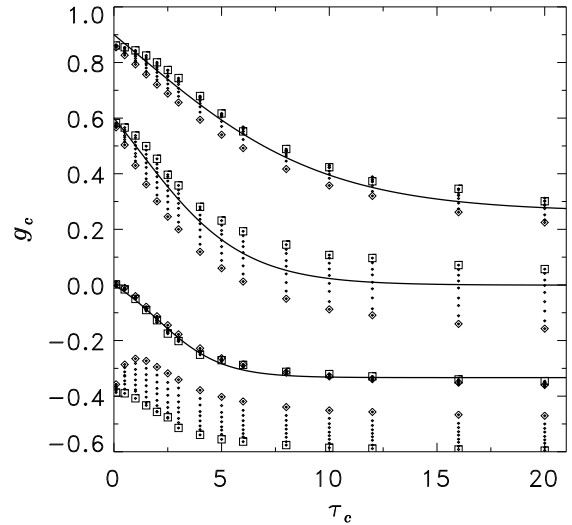


Fig. 10.— The effective clump scattering asymmetry parameter $g_c = \langle \cos \theta_{exit} \rangle$, where θ_{exit} is the angle between impacting and exiting directions as simulated by Monte Carlo calculations, is plotted as a function of the clump optical depth τ_c , for four values of the dust scattering asymmetry parameter, $g_d = -0.4, 0.0, 0.6,$ and 0.9 , corresponding to the intersection of each curve with the vertical axis at $\tau_c = 0$. The square symbols are for dust scattering albedo of $\omega_d = 0.1$, the diamonds for $\omega_d = 0.9$, and the dots show intermediate values of ω_d in increments of 0.1. The solid lines show the empirical approximation given by eq.(43) for $\omega_d = 0.5$.

An important term in eq.(34) is n_c , the density of clumps, which we shall now discuss in detail since it is the key to our extension of the mega-grains approximation. Define the porosity, Q_c , of a randomly located collection of identical clumps as the ratio of the total volume of clumps, *including* possible overlaps, to the volume V of the medium:

$$Q_c = \frac{N_c v_c}{V} \quad (44)$$

where N_c is the total number of clumps and v_c is the volume of just one clump. Equation (44) is easily solved for the density of clumps

$$n_c = \frac{N_c}{V} = \frac{Q_c}{v_c} = \frac{3Q_c}{4\pi r_c^3}, \quad (45)$$

as a function of the porosity and the radius of a spherical clump r_c . Substituting for n_c in eq.(34) gives

$$\Lambda_{mg} = \frac{3Q_c}{4r_c} P_i(\tau_c) \quad (46)$$

for the interaction coefficient of the mega-grains, where τ_c is the optical radius of a clump.

The filling factor f_c is related to the porosity, Q_c , of the clumps by

$$f_c = 1 - e^{-Q_c} \quad (47)$$

because the probability that a random point is not in a clump goes as e^{-Q_c} (this is a very good approximation to eq.(10) when $v_c \ll V$, see Appendix B). When $f_c \ll 1$ then $f_c \simeq Q_c$, however as $f_c \rightarrow 1$ we have $Q_c = -\ln(1 - f_c) \rightarrow \infty$, since then the clumps tend to overlap. Thus an obvious problem with equation (46) is that as $f_c \rightarrow 1$ we have $Q_c \rightarrow \infty$ causing $\Lambda_{mg} \rightarrow \infty$. Indeed, Hobson & Padman found that $f_c < 0.3$ is the useful range for the mega-grains approximation. The clump overlapping fraction is calculated as $(Q_c - f_c)/Q_c$, and for $f_c < 0.3$ it is less than 16% of the volume of clumps, but as $f_c > 0.3$ the overlapping volume fraction increases rapidly toward 100% so that the clumps can no longer be treated as separate mega-grains.

There is another problem with the previous equation, which is more subtle but still important. Consider the behavior of eq.(46) as $\tau_c \rightarrow 0$, which occurs when either $r_c \rightarrow 0$, $\kappa \rightarrow 0$ or $\rho_{hom} \rightarrow 0$ (holding f_c and $\alpha = \rho_c/\rho_{icm}$ constant). In that case $P_i(\tau_c) \sim 4\tau_c/3$, which simplifies eq.(46), and upon

substituting for τ_c with eq.(33), the clump radius cancels giving

$$\Lambda_{mg} \approx \frac{Q_c}{r_c} \tau_c = (\rho_c - \rho_{icm}) \kappa Q_c \quad (48)$$

when the clump optical radii are very small. Substituting this into eq.(35) gives

$$\begin{aligned} \Lambda_{eff} &= \Lambda_{mg} + \kappa \rho_{icm} \\ &\approx \kappa [(\rho_c - \rho_{icm}) Q_c + \rho_{icm}] \end{aligned} \quad (49)$$

for the behavior of the effective interaction coefficient of the two-phase clumpy medium as $\tau_c \rightarrow 0$. The problem with this behavior is that since $Q_c > f_c$ we get that

$$\Lambda_{eff} > \kappa [(\rho_c - \rho_{icm}) f_c + \rho_{icm}] = \kappa \rho_{hom} \quad (50)$$

using eq.(7) for the final equality. Thus as the clump optical depths become small, Λ_{eff} exceeds the interaction coefficient of the equivalent homogeneous medium. If L is the geometrical thickness of the medium then eq.(50) implies that

$$\tau_{eff} = L \Lambda_{eff} > L \kappa \rho_{hom} = \tau_{hom}, \quad (51)$$

contradicting equations (3) and (4) which state that a clumpy medium is more transparent than the equivalent homogeneous medium. The inequality in eqs.(50) and (51) becomes greater in error as f_c increases since then $Q_c \rightarrow \infty$.

An immediate solution to the problem is to substitute f_c in place of Q_c in eq.(46), then obtaining

$$\Lambda_{mg} = \frac{3f_c}{4r_c} P_i(\tau_c) \quad (52)$$

which gives the correct behavior of $\Lambda_{eff} < \kappa \rho_{hom}$ as $\tau_c \rightarrow 0$ for values of the clump filling factor. However, now consider the behavior as $\tau_c \rightarrow \infty$, occurring when $\rho_{hom} \rightarrow \infty$ or $\kappa \rightarrow \infty$ while holding f_c , α , and r_c constant. Then $P_i(\tau_c) \rightarrow 1$ and $\Lambda_{mg} \rightarrow 3f_c/4r_c$ as the clumps become opaque. For values of $f_c > 0.1$ the resulting effective interaction coefficient $\Lambda_{eff} = 3f_c/4r_c + \kappa \rho_{icm}$ underestimates the actual value found from Monte Carlo simulations (see Figure 11(b) and discussion below). In addition, as $f_c \rightarrow 1$ we should have $\Lambda_{eff} \rightarrow \kappa \rho_{hom}$, but instead eq.(52) gives $\Lambda_{eff} \rightarrow 3/4r_c + \kappa \rho_{icm}$, which because of the dependence on r_c will in general not reach the correct limit.

To extend the mega-grains approximation to all filling factors and retain the correct behavior as the clumps become optically thin or opaque, we propose to renormalize the clump radii by the factor $(1 - f_c)^\gamma$, where $0 < \gamma \leq 1$ is a parameter that can fine tune the behavior as the clumps become opaque. In Appendix D we discuss the motivation and a possible interpretation of this renormalization of the clump radii. Substituting $r_c(1 - f_c)^\gamma$ for all instances of r_c in eq.(52) we get

$$\Lambda_{mg} = \frac{3f_c}{4r_c} \frac{P_i [\tau_c(1 - f_c)^\gamma]}{(1 - f_c)^\gamma}, \quad (53)$$

our new definition of the mega-grains interaction coefficient. Now as $\tau_c \rightarrow 0$ or $f_c \rightarrow 1$ we have that $P_i [\tau_c(1 - f_c)^\gamma] \sim \frac{4}{3}\tau_c(1 - f_c)^\gamma$ and so the behavior of eq.(53) is

$$\Lambda_{mg} \sim \frac{f_c}{r_c} \tau_c = (\rho_c - \rho_{icm}) \kappa f_c \quad (54)$$

since the $(1 - f_c)^\gamma$ factor cancels out. This gives the desired result of $\Lambda_{eff} \rightarrow \kappa\rho_{hom}$ as $\tau_c \rightarrow 0$ or $f_c \rightarrow 1$, and keeps $\Lambda_{eff} < \kappa\rho_{hom}$ for a clumpy medium, thereby extending the mega-grains approximation to the full range of $0 \leq f_c \leq 1$.

In the other extreme, when $\tau_c \gg (1 - f_c)^{-\gamma}$ then $P_i [\tau_c(1 - f_c)^\gamma] \sim 1$ resulting in

$$\Lambda_{mg} \sim \frac{3f_c}{4r_c(1 - f_c)^\gamma}. \quad (55)$$

Comparing this with the previously discussed versions of the mega-grains approximation gives the following sequence of inequalities in the limit as the clumps become opaque:

$$\frac{3f_c}{4r_c(1 - f_c)} > \frac{3Q_c}{4r_c} > \frac{3f_c}{4r_c}, \quad (56)$$

corresponding to equations (53), (46), and (52) respectively, with $\gamma = 1$ and $f_c < 1$. Varying the parameter γ allows for adjustment of the opaque clump limit behavior of eq.(53) over the complete range in the above sequence of inequalities: as $\gamma \rightarrow 0$ the left side of the inequality approaches the right side. We find that the optimal value of γ in our extended mega-grains approximation depends on the arrangement of the source of photons with respect to the geometry of the clumpy medium: $\gamma \sim 0.5$ gives a good approximation for the situation of photons impacting a slab of clumps with a fixed angle with respect to the

surface normal, whereas $\gamma \sim 0.75$ works better for a central source within a sphere, and $\gamma = 1$ works best for uniformly distributed sources. When $f_c \ll 1$ the variation of the extended mega-grains approximation is small with respect to the parameter γ , and of course vanishes as the filling factor goes to zero. We shall use $\gamma = 1$ unless indicated otherwise.

Figure 11 compares the three versions of the mega-grains approximation (MGA) to Monte Carlo simulations. Figure 11(a) shows the ratio τ_{eff} / τ_{hom} versus τ_{hom} for the case of $f_c = 0.2$, $\alpha = 100$, and with $r_c = 0.05$ in the same units as ρ_{hom} and κ (f_c and α are dimensionless). By definition, $\tau_{eff} = R\Lambda_{eff}$ and $\tau_{hom} = R\kappa\rho_{hom}$, where R is the extent of the medium. The upper horizontal axis is the clump optical depth, τ_c , which is proportional to τ_{hom} via

$$\tau_c = \left(\frac{r_c}{R}\right) \tau_{hom} \left[\frac{(\alpha - 1)}{(\alpha - 1)f_c + 1} \right], \quad (57)$$

derived by combining equations (8) and (33). The dashed line in Figure 11(a) results from the use of equation (46), the straightforward implementation of HP93, and it clearly exceeds unity for $\tau_c < 0.2$ and $\tau_{hom} < 1$, violating the requirement that $\tau_{eff} < \tau_{hom}$. The overshoot of unity becomes worse for larger filling factors. The diamonds are results from Monte Carlo simulations of a central source in a sphere of radius $R = 1$ containing a two-phase clumpy medium characterized by the same parameters but with no scattering ($\omega_d = 0$). Each diamond plotted is the ratio τ_{eff} / τ_{hom} , where τ_{eff} is computed by eq.(13). The dotted line results from the use of equation (52), giving $\tau_{eff} < \tau_{hom}$ as required, however the disagreement with Monte Carlo results becomes worse as τ_{hom} increases. The solid line results from the use of equation (53), our new definition of the mega-grains interaction coefficient, also giving $\tau_{eff} < \tau_{hom}$ and agreeing well with the Monte Carlo results.

Figure 11(b) compares τ_{eff} resulting from the three version of the MGA at large τ_{hom} (equivalent to large τ_c) for the same clumpy medium. As before, the diamonds are results from the same Monte Carlo simulations. The dotted line is produced by using equation (52), giving

$$\tau_{eff} \rightarrow R(3f_c/4r_c + \kappa\rho_{icm}) \quad (58)$$

as $\tau_c \rightarrow \infty$, which clearly disagrees with the Monte Carlo results. The dashed line is produced by using equation (46), giving

$$\tau_{eff} \rightarrow R(3Q_c/4r_c + \kappa\rho_{icm}) \quad (59)$$

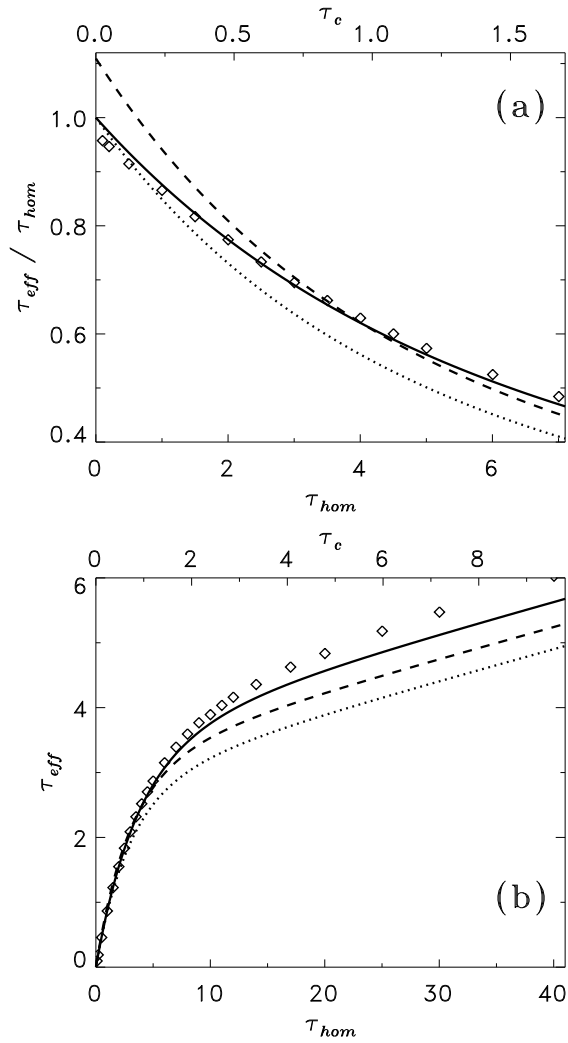


Fig. 11.— Comparison of three versions of the megagrains approximations (MGA) with Monte Carlo results, for the case of no scattering, in a clumpy medium having $f_c = 0.2$, $\alpha = 100$, and $r_c = 0.05$. In both panels (a) and (b) the dashed line results from the original version of MGA using eq.(46), the dotted line from the modified version using eq.(52), and the solid line is our new extended version of MGA using eq.(53). The diamonds are results from Monte Carlo simulations. Panel (a) shows the ratio of the effective optical depth of the clumpy medium, τ_{eff} , to the equivalent homogeneous optical depth, τ_{hom} , as a function of τ_{hom} and the clump optical radii τ_c (upper horizontal axis). Panel (b) shows τ_{eff} as a function of larger values of τ_{hom} and τ_c .

as $\tau_c \rightarrow \infty$, which is in better agreement with the Monte Carlo results. The solid line is produced by our extended MGA, using eq.(53), and as $\tau_c \rightarrow \infty$

$$\tau_{eff} \rightarrow R \left[\frac{3f_c}{4r_c(1-f_c)} + \kappa\rho_{icm} \right], \quad (60)$$

which provides the best approximation of the Monte Carlo results. There is a smooth transition in the slope of the τ_{eff} curves as τ_c increases, and when the clumps become optically thick ($\tau_c > 4$) their contribution to the absorption becomes a fixed quantity so the only further change is due to the ICM density. Thus all versions of the MGA become linear as $\tau_c \gg 1$ and $\tau_{hom} \rightarrow \infty$, basically having the slope

$$\frac{\partial\tau_{eff}}{\partial\tau_{hom}} \rightarrow \frac{\partial\rho_{icm}}{\partial\rho_{hom}} = \frac{1}{(\alpha-1)f_c+1}, \quad (61)$$

which for the parameters used for Figure 11(b) is a value of about $\frac{1}{21}$. The intercepts of the asymptotic lines with the vertical axis are given by R times the first term in each of the above eqs.(58-60), and these values are approximately the average number of clumps encountered along a random line of sight (see Appendix B).

Now consider the behavior of the MGA as the clump radii vanish and other parameters are held fixed. This is shown in Figure 12 for the case of $f_c = 0.2$, $\alpha = 100$, and $\tau_{hom} = 1$, where τ_{eff} is plotted versus r_c and τ_c . The dashed line produced by using eq.(46) exceeds the value of $\tau_{hom} = 1$ (thin long dashed line) when $r_c < 0.03$ ($\tau_c < 0.2$), because as $r_c \rightarrow 0$ we have $\tau_c \rightarrow 0$, and by eqs.(48) and (49)

$$\tau_{eff} \rightarrow R\kappa[(\rho_c - \rho_{icm})Q_c + \rho_{icm}] > \tau_{hom}.$$

Thus the same problematic behavior of $\tau_{eff} > \tau_{hom}$ that was shown in Figure 11(a) for $\tau_{hom} \rightarrow 0$ occurs as $r_c \rightarrow 0$ and τ_{hom} is held constant. The solid line is produced by our extended MGA, using eq.(53), and clearly yields the expected behavior $\tau_{eff} < \tau_{hom}$ for the full range of clump radii, since then as $r_c \rightarrow 0$ we have the exact limit of

$$\tau_{eff} \rightarrow R\kappa[(\rho_c - \rho_{icm})f_c + \rho_{icm}] = \tau_{hom}$$

[see eq.(54)]. The diamonds are results from Monte Carlo simulations, in good agreement with our extended MGA. The dotted line is produced by using eq.(52), which has the correct limit as $r_c \rightarrow 0$ but tends to underestimate τ_{eff} at larger clump radii.

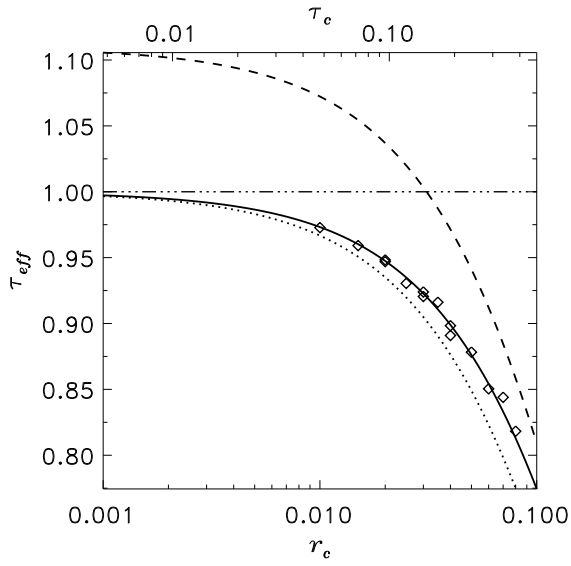


Fig. 12.— Comparison of HP93 version [eq.(46), dashed line], modified version [eq.(52), dotted line], and new extended version [eq.(53), solid line] of the MGA as a function of the clump radius r_c . Results of Monte Carlo simulations are plotted as diamonds, and the clumpy medium is defined by parameters $f_c = 0.2$, $\alpha = 100$, and $\tau_{hom} = 1$.

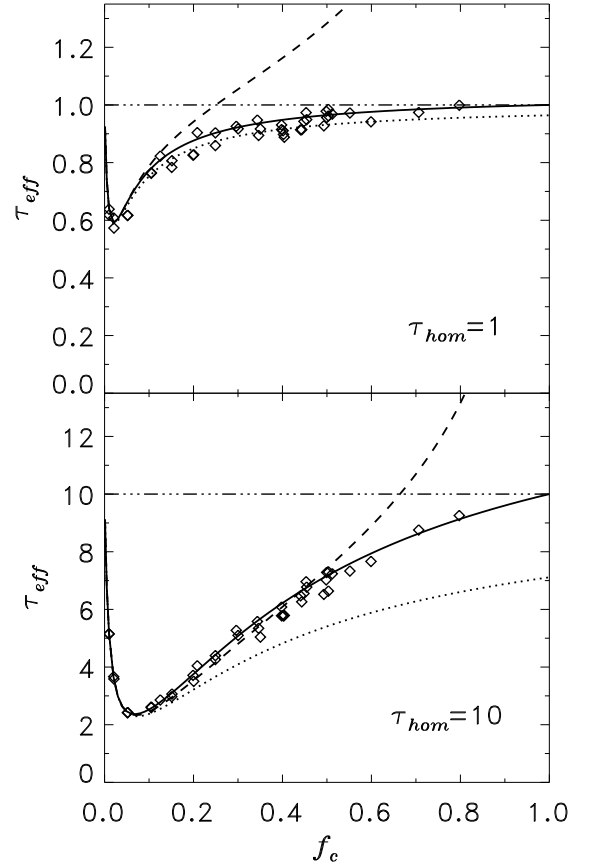


Fig. 13.— Comparison of τ_{eff} (vertical axes) predicted by the new extended version [eq.(53) with $\gamma = 1$, solid line], modified version [eq.(52), dotted line], and original version [eq.(46), dashed line] of the MGA, with Monte Carlo results (diamonds), over the full range of clump filling factors ($0 < f_c < 1$ on horizontal axis), for cases $\tau_{hom} = 1$ and $\tau_{hom} = 10$, as indicated. The medium consists of clumps with radii $r_c = 0.05$ and density ratio $\alpha = 100$.

Figure 13 compares the extended MGA to the original version over the full range of clump filling factors, $0 \leq f_c \leq 1$, with $\alpha = 100$ and $r_c = 0.05$ held constant, for cases $\tau_{hom} = 1$ and $\tau_{hom} = 10$, as indicated. In each case the horizontal axis is f_c and the vertical axis is τ_{eff} , the effective optical depth. The diamonds are the τ_{eff} resulting from Monte Carlo simulations of a central source in a sphere of unit radius containing a two-phase clumpy medium with clump filling factors in the range $0.01 \leq f_c \leq 0.8$, also with $\alpha = 100$ and $r_c = 0.05$ held constant. Clearly the extended MGA [using eq.(53) in eq.(35)], shown as the solid lines, gives the best agreement with the Monte Carlo results, and satisfies the condition $\tau_{eff} < \tau_{hom}$ for the full range of clump filling factors. The original version of the MGA [using eq.(46)], shown as the dashed lines, starts diverging to infinity for $f_c > 0.1$ in the case of $\tau_{hom} = 1$, and diverges to infinity for $f_c > 0.5$ in the case of $\tau_{hom} = 10$. The dotted line is produced using eq.(52), which underestimates the value of τ_{eff} and fails to reach the correct limit of $\tau_{eff} \rightarrow \tau_{hom}$ as $f_c \rightarrow 1$, especially when τ_{hom} is large. The fluctuations in the Monte Carlo results are due to variations in particular realizations of clumps in a finite volume, and these fluctuations grow larger as $f_c \rightarrow 1$.

The behavior of τ_{eff} versus f_c always exhibits a minimum at a single value of f_c which has a complicated dependence on the other parameters characterizing the clumpy medium. To study this behavior, Figure 14 shows the prediction of τ_{eff} by the extended MGA (solid lines) and the contribution from each phase on the clumpy medium: the dashed lines are ICM component, $\tau_{icm} = R\kappa\rho_{icm}$, and the dotted lines are the component of the effective optical depth due to clumps, $\tau_{mg} = R\Lambda_{mg}$, so that $\tau_{eff} = \tau_{mg} + \tau_{icm}$. The horizontal axis is now $\log_{10} f_c$ and the cases of $\tau_{hom} = R\kappa\rho_{hom} = 1$ and 10 are shown, with $\alpha = 100$, and $r_c = 0.05$ (same as Figure 13). Some of the same Monte Carlo results are shown (diamonds) to verify the behavior. Starting at $f_c \sim 0$, τ_{icm} decreases rapidly as f_c increases since ρ_{icm} , given by eq.(8), is inversely related to f_c and the total mass is held constant. In fact the shape of the $\tau_{icm} = R\kappa\rho_{icm}$ curve depends only on α and f_c so only the magnitude changes with the value of τ_{hom} : the shape of the variation of τ_{icm} versus f_c is exactly the same for the two cases of τ_{hom} in Figure 14. The opacity of the clumps is also inversely related to their filling factor, as seen in eq.(57), and so τ_c is near maximum when $f_c \sim 0$, and then $\tau_{mg} \sim R(4f_c/3r_c)$. Thus τ_{mg} increases lin-

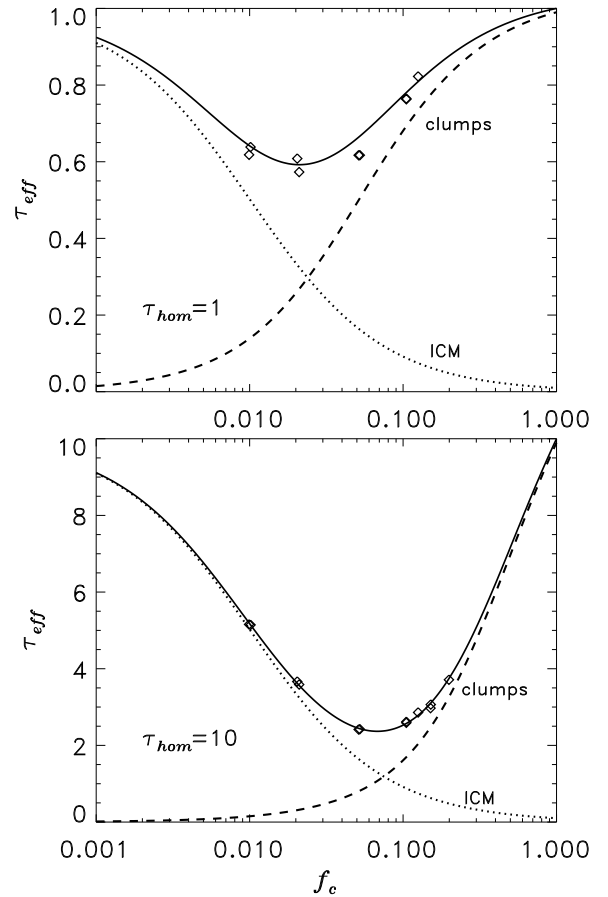


Fig. 14.— Analysis of τ_{eff} versus f_c predicted by our new extended version of the MGA for the same cases shown in Figure 13. The dashed lines are $\tau_{mg} = R\Lambda_{mg}$ [eq.(53)], the dotted lines are $\tau_{icm} = R\kappa\rho_{icm}$, and the solid lines are the sum $\tau_{eff} = \tau_{mg} + \tau_{icm}$.

early with f_c until the clumps become optically thin and they fill up the medium, causing $\tau_{mg} \rightarrow \tau_{hom}$. The linear increase of τ_{mg} does not compensate for the rapid decrease of τ_{icm} with f_c , the net effect being that τ_{eff} decreases with increasing f_c until the clumps start to fill the medium. Therefore τ_{eff} goes through a minimum as a function of f_c when the number of lines of sight which pass through the very low density ICM greatly exceeds the number of paths intersecting optically thick clumps. For $f_c \ll 1$, the magnitude of τ_{mg} is independent of τ_{hom} whereas the magnitude of τ_{icm} is directly proportional to τ_{hom} , so the minimum of τ_{eff} occurs at a larger value of f_c for the case of $\tau_{hom} = 10$ than for the case of $\tau_{hom} = 1$.

In general, the minimum of τ_{eff} occurs at nearly the same value of f_c for which $\tau_{mg} = \tau_{icm}$, and analysis of the equations shows why this is true. Assuming that $f_c \ll 1$ then

$$\frac{\partial \tau_{mg}}{\partial f_c} \approx R \left(\frac{4}{3r_c} \right) \approx \frac{\tau_{mg}}{f_c}. \quad (62)$$

Assuming that $\alpha \gg 1$ then

$$\begin{aligned} \frac{\partial \tau_{icm}}{\partial f_c} &= -R\kappa\rho_{icm} \left[\frac{\alpha - 1}{(\alpha - 1)f_c + 1} \right] \\ &\approx -\frac{\tau_{icm}}{f_c + \frac{1}{\alpha}}. \end{aligned} \quad (63)$$

Now since $\tau_{eff} = \tau_{mg} + \tau_{icm}$ we have that

$$\frac{\partial \tau_{eff}}{\partial f_c} \approx \frac{\tau_{mg}}{f_c} - \frac{\tau_{icm}}{f_c + \frac{1}{\alpha}}. \quad (64)$$

The local minimum occurs when the partial derivative is zero so that

$$\frac{\partial \tau_{eff}}{\partial f_c} = 0 \iff \left(1 + \frac{1}{\alpha f_c} \right) \tau_{mg} \approx \tau_{icm}, \quad (65)$$

which is approximately the relationship between the minimum of τ_{eff} and the intersection of the τ_{mg} and τ_{icm} curves in Figure 14. Consequently, as a function of f_c (with constant $\alpha \gg 1$), the total luminosity absorbed by a clumpy medium attains a minimum when the luminosities absorbed in the clumps and in the ICM are equal, and this is demonstrated over a large region of parameter space in §7.3.

The previous discussion of τ_{eff} has been for the case of no scattering, or for scattering and absorption together considered as interaction with dust. To model scattering in a clumpy medium we need the

effective scattering albedo, ω_{eff} , given by eq.(37), which depends on ω_c , the clump albedo given by eq.(41). We find that the clump radius renormalization technique introduced above also needs to be applied to the clump albedo formula in order to produce the correct approximation for scattering in the clumpy medium as $f_c \rightarrow 1$. The new equation is then

$$\omega_c = \omega_d \mathcal{P}_{esc}^u [\tau_c(1 - f_c)^\gamma, \omega_d] \quad (66)$$

so that $\omega_c \rightarrow \omega_d$ as $f_c \rightarrow 1$, since then the escape probability becomes unity. This leads to the correct behavior of $\omega_{eff} \rightarrow \omega_d$ for as $f_c \rightarrow 1$. For the same reasons, τ_c in eq.(43) is replaced by $\tau_c(1 - f_c)^\gamma$ to give the correct limits as $f_c \rightarrow 1$ for g_c , the clump asymmetry parameter, and g_{eff} , the effective scattering asymmetry parameter. All the equations are summarized in §5.

In summary, we have extended and improved the formulas for the effective optical depth and albedo of a clumpy medium, and introduced an approximation for the effective scattering asymmetry parameter. The validity of the extended mega-grains formulas, with scattering and for other source distributions, is further demonstrated by comparison with Monte Carlo simulations in §6 and §7.

4.3. Comparison with Earlier Theory

Here we compare the extended mega-grains approximation (MGA) for the effective optical depth of just clumps with the theory of Natta & Panagia (1984) (hereafter NP84), when α is large so the ICM can be ignored. Figure 15 compares the approximations and quantities involved as function of $\log_{10} f_c$, for the case of $\tau_{hom} = 2$, $\alpha = 1000$, and $r_c = 0.05$. The top panel shows τ_c (solid line), the clump optical radii, and two extreme values bounding F_c , the average number of clumps encountered along a random line of sight:

$$F_c^q = R \left(\frac{3Q_c}{4r_c} \right) \quad (67)$$

is the dashed line which eventually diverges to infinity, where Q_c is the porosity given by eq.(44), and the dotted line is

$$F_c^f = R \left(\frac{3f_c}{4r_c} \right), \quad (68)$$

which stays finite, so that $F_c^f \leq F_c \leq F_c^q$ (see Appendix B). F_c is also called the covering factor of the clumps, and the random lines of sight are perpendicular to the plane of a slab of thickness R , or radial in

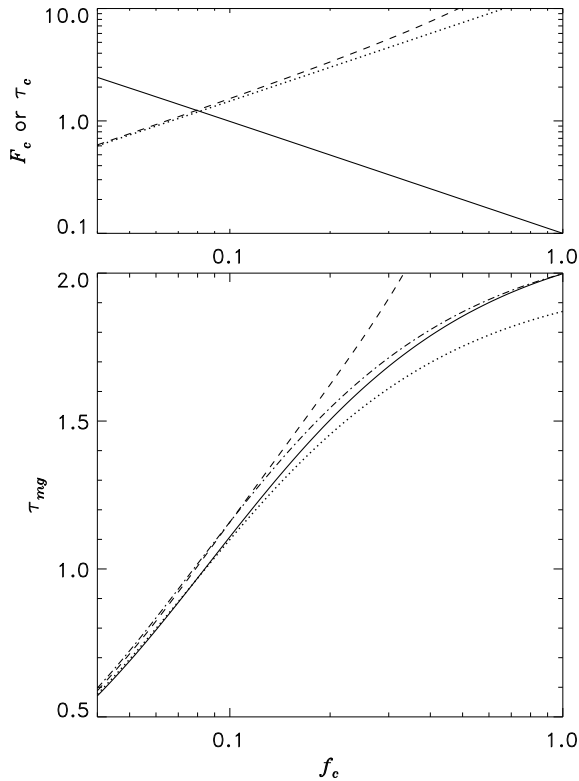


Fig. 15.— Comparison our extended MGA with the effective optical depth of a clumpy medium derived by Natta & Panagia (1984), for the case of $\tau_{hom} = 2$, $\alpha = 1000$, and $r_c = 0.05$. The top panel shows τ_c (solid line), the clump optical radii, or upper and lower bounds for F_c , the covering factor of clumps (dashed and dotted lines). The solid line in bottom graph is $\tau_{mg} = R\Lambda_{mg}$ produced by eq.(53). The dashed and dotted lines are produced by eq.(69), using τ_c and bounds on F_c from the top panel. The dash-dotted line is produced by eq(70).

the case of a spherical medium of radius R . In the bottom panel the solid line is $\tau_{mg} = R\Lambda_{mg}$ using eq.(53), the extended MGA. Assuming that the number of clumps encountered along a random line of sight is Poisson distributed with mean number F_c , NP84 derived an equation for the effective optical depth:

$$\tilde{\tau} = F_c \left(1 - e^{-4\tau_c/3} \right), \quad (69)$$

where $\frac{4}{3}\tau_c$ is the expected optical depth of a random path through a spherical clump. The result of using $F_c = F_c^q$ in eq.(69) is shown by the dashed line in the bottom panel of Figure 15, and $\tilde{\tau}$ agrees with τ_{mg} (solid line) for $f_c < 0.1$, corresponding to $F_c \leq 1$, but $\tilde{\tau}$ exceeds τ_{hom} when $f_c > 0.3$ and $F_c > 5$, diverging to infinity.. If instead $F_c = F_c^f$ is used in eq.(69) then $\tilde{\tau}$ remains finite as shown by the dotted line. Applying the clump radii renormalization gives

$$\tilde{\tau} = F_c^f \left(\frac{1 - \exp[-4\tau_c(1 - f_c)/3]}{1 - f_c} \right), \quad (70)$$

shown as the dash-dotted line, which is almost identical to τ_{mg} . So the approach used by NP84 gives almost the same result for τ_{mg} as the extended MGA when the average optical depth of a sphere, $\frac{4}{3}\tau_c$, is used. The quantity $1 - e^{-4\tau/3}$ happens to be a good approximation of $P_i(\tau)$, with a maximum relative difference of 5% overestimation occurring at $\tau \approx 1.5$ when $P_i(1.5) \approx 0.8$.

4.4. Escape and Absorption Probabilities for Clumpy Media

The effective optical depth, τ_{eff} , effective scattering albedo, ω_{eff} , and effective asymmetry parameter, g_{eff} , given by the mega-grains approximation reduces the basic radiative transfer properties of a two-phase clumpy medium to an effectively homogeneous medium. Therefore we propose use τ_{eff} , ω_{eff} , and g_{eff} , given by equations (53, 35, 36), (37, 40), and (42, 43) respectively, in the escape and absorption probability formulae that were developed for homogeneous media to estimate the escaping or absorbed fractions of photons in clumpy media. In particular, for isotropic emission uniformly distributed within a sphere we use \mathcal{P}_{esc}^u given by eqs.(19) and (20), for a central point source we use \mathcal{P}_{esc}^c given by eqs.(16-18), and for a uniformly illuminating external source we use \mathcal{P}_{abs}^x given by eq.(29). The full set of equations is summarized as a convenient list in §5.

We find these analytic approximations give results in reasonable agreement with Monte Carlo simulations, as is demonstrated in §6. As suggested by HP93, we also conjecture that given an escape probability function for a homogeneous medium having any geometry and any distribution of sources, the escape probability for a two-phase clumpy medium of same geometry and source distribution can be reasonably approximated by substituting the effective optical parameters given by the mega-grains equations into the homogeneous escape probability function.

4.5. The Fractions Absorbed in Each Phase of a Clumpy Medium

The energy of the radiation absorbed by the dust is converted into heat and then re-radiated as infrared (IR) photons. The spectrum of the IR emission from the dust is dependent on the dust temperature, which in most cases is determined by the equilibrium between the energy absorbed and emitted. In this paper, we shall not deal with very small dust grains which can undergo temperature fluctuations, an effect that will cause a wider distribution in dust temperature and enhanced IR emission in the $\sim 3 - 20\mu\text{m}$ range (e.g. Dwek et al. 1997). For the case of a homogeneous medium with uniformly distributed emitters, most of the dust will be at the same temperature (accept at the boundary of the medium where the temperature will be lower). When the uniformly distributed emission occurs in an inhomogeneous medium there will be a distribution of dust temperatures. In a two-phase clumpy medium, the clumps will most likely attain a different radiative equilibrium temperature than the ICM, since the clumps will absorb/radiate a different amount of energy. Given the total amount of energy absorbed by the dust we need to know what fraction is absorbed in the clumps and what fraction in the ICM, to determine the approximate equilibrium temperature of each phase of the clumpy medium.

In the mega-grains approximation it is the overdensity of the clumps which enters into the formulation, in this way separating the clumps and the ICM while keeping the ICM continuous. However, to determine the fraction of photons absorbed by the clumps we must consider the clumps as being completely separate from the ICM, therefore considering the full density of dust in the clumps, and so the ICM is not viewed as uniform and continuous but as having holes occupied by clumps. This approach will give

the correct absorbed fractions as $\alpha = \rho_c/\rho_{icm} \rightarrow 1$. Thus we define the full clump optical depth as:

$$\tau_c^a \equiv \kappa \rho_c r_c = \alpha \kappa \rho_{icm} r_c, \quad (71)$$

where κ is the total absorption plus scattering coefficient of the dust grains per unit mass, and r_c is the clump radius. We then replace τ_c with τ_c^a in all the mega-grains approximation equations, and the superscript “a” shall indicate that all of the clump optical depth is being used in the following quantities, in particular, Λ_{mg}^a is the result of using τ_c^a in eq.(34).

First we deal with the case of a point source in the center of a spherical clumpy medium, and assume that the point source is not in any clump. Let R be the radius of the sphere and define optical depths

$$\tau_{mg}^0 = R \Lambda_{mg}^a, \quad (72)$$

$$\tau_{icm}^0 = R \kappa \rho_{icm}, \quad (73)$$

due to the mega-grains (subscript “mg”) and ICM, respectively, where the superscript “0” indicates that this is for no scattering. To model the effects of scattering we employ the analytical approximation for the effective optical radius of a homogeneous sphere with scattering, as given by equations (16) and (17), defining new optical depths as

$$\tau_{mg} = \tau_{mg}^0 (1 - \omega_c^a)^{\chi(\tau_{mg}^0, g_c^a)}, \quad (74)$$

$$\tau_{icm} = \tau_{icm}^0 (1 - \omega_d)^{\chi(\tau_{icm}^0, g_d)}, \quad (75)$$

for the mega-grains and ICM, respectively, where the function $\chi(\tau, g)$ is given by eq.(17). Note that we use clump scattering properties ω_c^a and g_c^a for τ_{mg} , and the usual dust scattering albedo and asymmetry parameter, ω_d and g_d , for the ICM optical depth. Of the total photons absorbed by the medium, the fraction, A_{icm}^c , that gets absorbed by the ICM is then estimated to be

$$A_{icm}^c \equiv \frac{(1 - f_c) \tau_{icm}}{\tau_{mg} + (1 - f_c) \tau_{icm}}, \quad (76)$$

where the superscript “c” indicates a central point source. The factor $1 - f_c$ is introduced to get an approximation which gives the correct behavior as $\alpha \rightarrow 1$ or $f_c \rightarrow 1$, because the volume occupied by the clumps should not be included in the ICM. Now if \mathcal{P}_{esc}^c is the fraction of photons which escapes the sphere then $A_{icm}^c(1 - \mathcal{P}_{esc}^c)$ is the fraction absorbed in the ICM and $(1 - A_{icm}^c)(1 - \mathcal{P}_{esc}^c)$ is the fraction absorbed by clumps.

In the case of an internal uniform distribution of emitters we consider the emission occurring in the clumps and ICM separately, as follows. For the fraction $1 - f_c$ of the photons which are emitted in the ICM we predict that A_{icm}^c will be absorbed by the ICM. For the fraction f_c which are emitted in the clumps we predict that a fraction $\mathcal{P}_{esc}^u(\tau_c^a, \omega_d)$ [given by eqs.(19) and (20)] of those photons will escape the clumps, and then a fraction A_{icm}^c of them will be absorbed by the ICM. The total fraction of emitted photons which will be absorbed by the ICM is then

$$A_{icm}^u \equiv A_{icm}^c [(1 - f_c) + f_c \mathcal{P}_{esc}^u(\tau_c^a, \omega_d)], \quad (77)$$

where the superscript “u” indicates that this is for the case of uniformly distributed emission of photons. This gives $A_{icm}^u < A_{icm}^c$ because part of the emission occurs inside clumps that are more dense than the ICM. Defining $F_{abs} \equiv 1 - \mathcal{P}_{esc}^u(\tau_{eff}, \omega_{eff})$ to be the total fraction of photons absorbed in the medium then $A_{icm}^u F_{abs}$ is the fraction absorbed in the ICM and $(1 - A_{icm}^u) F_{abs}$ is the fraction absorbed by clumps.

To estimate absorbed fractions for the case of a uniformly illuminating external source we just take the average of the values for central source and uniform source:

$$A_{icm}^x \equiv \frac{A_{icm}^u + A_{icm}^c}{2}. \quad (78)$$

The estimate is motivated by Monte Carlo simulations which indicate that $A_{icm}^u < A_{icm}^x < A_{icm}^c$. If $\mathcal{P}_{abs}^x(\tau_{eff}, \omega_{eff})$ is the total fraction absorbed in the sphere then $A_{icm}^x \mathcal{P}_{abs}^x$ is the fraction absorbed in the ICM and $(1 - A_{icm}^x) \mathcal{P}_{abs}^x$ is the fraction absorbed by clumps. The absorbed fractions predicted by the above equations are compared with the results of Monte Carlo simulations in §6.

5. SUMMARY OF EQUATIONS

5.1. Escape and Absorption Probabilities

In the following formulae, use $(\tau_{hom}, \omega_d, g_d)$ for all occurrences of (τ, ω, g) if the medium is homogeneous, or if the medium is clumpy use $(\tau_{eff}, \omega_{eff}, g_{eff})$ given by the mega-grains equations below.

Central Point Source:

$$\begin{aligned} \mathcal{P}_{esc}^c(\tau, \omega, g) &\equiv \exp[-\tau_S(\tau, \omega, g)] \\ \tau_S(\tau, \omega, g) &\equiv \tau(1 - \omega)^{\chi(\tau, g)} \\ \chi(\tau, g) &\equiv 1 - \frac{1}{2} \left(1 - e^{-\tau/2}\right) (1 - g)^{\frac{1}{2}} \end{aligned} \quad (79)$$

Uniform Distribution of Emitters:

$$\mathcal{P}_{esc}^u(\tau, \omega) \equiv \frac{P_e(\tau)}{1 - \omega[1 - P_e(\tau)]} \quad (80)$$

$$P_e(\tau) = \frac{3}{4\tau} P_i(\tau) \quad (81)$$

$$P_i(\tau) = 1 - \frac{1}{2\tau^2} + \left(\frac{1}{\tau} + \frac{1}{2\tau^2}\right) e^{-2\tau} \quad (82)$$

Uniformly Illuminating External Source:

$$\begin{aligned} \mathcal{P}_{abs}^x(\tau, \omega) &\equiv P_i(\tau) [1 - \omega \mathcal{P}_{esc}^u(\tau, \omega)] \\ &= \frac{4\tau(1 - \omega)}{3} \mathcal{P}_{esc}^u(\tau, \omega) \end{aligned} \quad (83)$$

Recall that \mathcal{P}_{esc}^u and \mathcal{P}_{abs}^x are valid (most accurate) when $g = g^*(\tau)$ [see eq.(21)], whereas $P_e(\tau)$ and $P_i(\tau)$ are exact formulae.

5.2. Mega-Grains Approximation

Input Parameters:

- κ = dust mass extinction coefficient
- ω_d = scattering albedo of dust grains
- g_d = scattering asymmetry parameter
- ρ_{hom} = average mass density of the dust
- f_c = filling factor of the clumps
- γ = MGA tuning parameter (~ 1)
- α = ρ_c / ρ_{icm}
- r_c = radius of each spherical clump
- R_S = radius of spherical medium.

Effective Optical Depth, τ_{eff} :

$$\rho_{icm} = \frac{\rho_{hom}}{(\alpha - 1) f_c + 1} \quad (\text{ICM density})$$

$$\tau_c = (\alpha - 1) \rho_{icm} r_c \kappa \quad (\text{clump optical radius})$$

$$\Lambda_{mg} = \frac{3f_c}{4r_c} \frac{P_i[\tau_c(1 - f_c)^\gamma]}{(1 - f_c)^\gamma} \quad (84)$$

$$\Lambda_{eff} = \Lambda_{mg} + \kappa \rho_{icm}$$

$$\tau_{eff} = R_S \Lambda_{eff}$$

where the formula for Λ_{mg} utilizes $P_i(\tau)$ given by eq.(82) and $0 < \gamma \leq 1$. Use $\gamma = 1$ for uniform internal/external sources, $\gamma = 0.75$ for central source, and $\gamma = 0.5$ for photons impacting a slab.

Effective Albedo, ω_{eff} :

$$\omega_{eff} = \frac{\omega_c \Lambda_{mg} + \omega_d \kappa \rho_{icm}}{\Lambda_{eff}} ,$$

where the clump albedo is

$$\omega_c = \omega_d \mathcal{P}_{esc}^u [\tau_c (1 - f_c)^\gamma, \omega_d] ,$$

and \mathcal{P}_{esc}^u is the OLEP formula stated in eq.(80) above.

Effective Scattering Asymmetry Parameter, g_{eff} :

$$g_{eff} = \frac{g_c \Lambda_{mg} + g_d \kappa \rho_{icm}}{\Lambda_{eff}} ,$$

where the clump asymmetry parameter is

$$\begin{aligned} g_c &= g_d - C \left(1 - \frac{1 + \exp(-B/A)}{1 + \exp[\tau_c (1 - f_c)^\gamma - B]/A} \right) \\ A &\equiv 1.5 + 4g_d^3 + 2\omega_d \sqrt{g_d} \exp(-5g_d) \\ B &\equiv 2 - g_d(1 - g_d) - 2\omega_d g_d \\ C &\equiv \left[3 - \sqrt{2g_d} - 2\omega_d g_d(1 - g_d) \right]^{-1} \end{aligned}$$

5.3. Fractions Absorbed in Each Phase

Let $P_{abs} = 1 - P_{esc}$ be the generic absorption probability. Then the fraction of photons absorbed in the ICM is $A_{icm} P_{abs}$, and the fraction absorbed by clumps is $(1 - A_{icm}) P_{abs}$, where A_{icm} is given by one of the following formulas, corresponding to the type of source. See below for definitions of τ_{mg} and τ_{icm} .

Central Point Source:

$$A_{icm}^c \equiv \frac{(1 - f_c) \tau_{icm}}{\tau_{mg} + (1 - f_c) \tau_{icm}} \quad (85)$$

Uniform Distribution of Emitters:

$$A_{icm}^u \equiv A_{icm}^c [(1 - f_c) + f_c \mathcal{P}_{esc}^u(\tau_c^a, \omega_d)] \quad (86)$$

Uniformly Illuminating External Source:

$$A_{icm}^x \equiv \frac{A_{icm}^u + A_{icm}^c}{2} \quad (87)$$

Component Optical Depths:

$$\begin{aligned} \tau_c^a &\equiv \kappa \rho_c r_c = \alpha \kappa \rho_{icm} r_c \\ \tau_{mg}^0 &= R_S \Lambda_{mg}^a \\ \tau_{icm}^0 &= R_S \kappa \rho_{icm} \end{aligned}$$

The superscript “a” indicates that the full clump optical depth is being used, i.e. Λ_{mg}^a is the result of using τ_c^a in eq.(84). The superscript “0” indicates that the quantities are for no scattering. To include the effects of scattering in spherical geometry, apply equations (79):

$$\begin{aligned} \tau_{mg} &= \tau_{mg}^0 (1 - \omega_c^a)^{\chi(\tau_{mg}^0, g_c^a)} \\ \tau_{icm} &= \tau_{icm}^0 (1 - \omega_d)^{\chi(\tau_{icm}^0, g_d)} . \end{aligned}$$

5.4. The Case of $\alpha < 1$

If one desires to model randomly distributed spherical cavities (e.g. SNRs instead of clumps) which have a lower density than the ICM (so that $\alpha < 1$), the mega-grains equations can be applied by redefining

$$\begin{aligned} f'_c &= 1 - f_c , \\ \alpha' &= \frac{1}{\alpha} , \end{aligned} \quad (88)$$

and using these new inverted values in the above equations to obtain $(\tau_{eff}, \omega_{eff}, g_{eff})$ for the medium with cavities. However, when computing the fractions absorbed in each phase of the medium we do not apply the inversion transform of eq.(88). The inverted mega-grains approximation is demonstrated in §6.3.

6. COMPARISON OF ANALYTIC APPROXIMATIONS WITH MONTE CARLO SIMULATIONS

In §4.2 we developed the extended mega-grains approximation (MGA) and compared it with Monte Carlo simulations, which verified the effective optical depth predicted by the approximations for the case of no scattering and when emission is from a central point source in a spherical clumpy medium. We shall use the acronym MCRT when referring to Monte Carlo simulations of radiative transfer, and the acronym MGEP when referring to the analytic approximations consisting of the mega-grains (MG) approximations combined with escape/absorption probability (EP) formulae, which were summarized §5. In this section we present more detailed comparisons of the MGEP model with MCRT simulations when scattering is also involved, and for all three types of source distributions discussed in §3. In the following we designate the cases of a central isotropic source by “C”, uniformly distributed internal sources by “U”, and uniformly illuminating external source by “X”.

We shall compare the MGEP approximations with MCRT results over a wide range of parameters that define a two-phase clumpy medium in spherical geometry, except that the clump radii will be held fixed at $r_c = 0.05$ relative to the radius of the sphere $R_S = 1$. A larger value would be less realistic and cause the number of clumps to be less than needed for good statistics in the MCRT model, whereas spherical clumps with radii smaller than $r_c = 0.05$ become difficult to represent accurately on a grid. All the Monte Carlo simulations were performed using a grid of 100^3 or 127^3 voxels to represent the clumpy medium, and followed at least 10^6 photons for each result. The quantities in the comparisons will be shown as a function of either equivalent homogeneous optical depth, τ_{hom} , clump filling factor, f_c , or clump to ICM density ratio, α , in the following three subsections.

6.1. Dependence on Optical Depth

Recall that the equivalent homogeneous optical depth of extinction, $\tau_{hom} = \kappa\rho_{hom}R_S$, can vary due to changing wavelength or dust mass (R_S is held constant), and so is the major parameter involved in modeling the transfer of a spectrum of radiation in a clumpy medium. Figure 4 showed the behavior of the effective optical depth τ_S [eq.(13)] versus τ_{hom} resulting from Monte Carlo simulations with scattering ($\omega_d = 0.6$ and $g_d = 0.6$) for three cases of the filling factor, $f_c = 0.1, 0.2,$ and 0.3 , (squares, triangles, and diamonds, respectively) with $\alpha = 100$. The dashed, dotted, and solid lines are produced by the extended mega-grains theory combined with eq.(79) to compute $\tau_S(\tau_{eff}, \omega_{eff}, g_{eff})$, and the curves agree well with Monte Carlo results. As discussed in §4.2, the transition in the variation of τ_S as a function τ_{hom} goes from clump dominated (steeper slope at low values of τ_{hom}) to ICM dominated (less slope at large τ_{hom}) as the clumps become opaque, and the occurrence of this transition can be estimated by eq.(57). Unless otherwise indicated, $\alpha = 100$ in this section.

In Figure 16 we study the effect of changing the dust scattering parameters for the case of $f_c = 0.2$, with the top panel showing the effective optical depth with or without scattering (τ_S or τ_{eff} respectively) for source type C, and bottom panel showing the escaping fraction of source type U, all versus τ_{hom} . The case of no scattering is indicated with squares for MCRT results and the dash-dot lines are the MGEP model. The diamonds and solid lines show MCRT and MGEP results, respectively, for $\omega_d = 0.8$ and

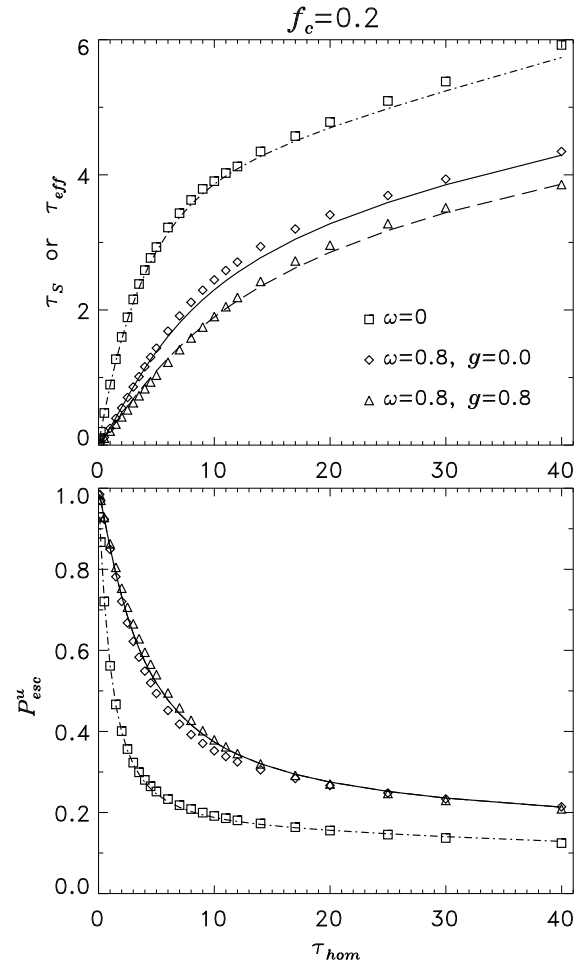


Fig. 16.— Comparison of MGEP theory (curves) to MCRT results (symbols) as function of τ_{hom} with $f_c = 0.2$ and $\alpha = 100$, for 3 different sets of dust scattering parameters as indicated in the plot legend.

$g_d = 0$ (isotropic scattering); the triangles and long-dashed lines show MCRT and MGEP results, respectively, for $\omega_d = 0.8$ and $g_d = 0.8$ (almost forward scattering). The values of τ_{eff} given by MGA (dash-dotted line) for no scattering are used in eq.(79), along with values of ω_{eff} and g_{eff} (not shown), to compute $\tau_S(\tau_{eff}, \omega_{eff}, g_{eff})$, the solid and long-dashed lines in the top panel. The solid line in the bottom panel is computed by using τ_{eff} and ω_{eff} in eq.(80) for source type U. The MCRT results show that, as expected, forward scattering dust lowers the effective optical depth and increases the escape probability as compared to isotropic scattering dust, especially for a central source of photons, and the analytical approximations of MGEP correctly predict this effect. In the case of a uniformly distributed source the dependence of the escaping fraction on the dust scattering asymmetry parameter g_d is weak, and so it is not a problem that g_d does not enter into the MGEP equations for source type U. The analytical approximations of MGEP agree well with the numerical results of MCRT at low optical depths, whereas at high optical depths there are some differences, especially for source type C, which are due to specific realizations of the clumpy medium in MCRT simulations, but the agreement is still acceptable.

Figure 17 compares in the top panel the absorbed fraction of photons from each type of source, and in the bottom panel the fraction of the total absorbed photons that are absorbed in just the ICM, as function of τ_{hom} , with $f_c = 0.1$, and with scattering parameters $\omega_d = 0.6$ and $g_d = 0.6$. The star, diamond, and square symbols represent MCRT numerical results for source types C, U, and X respectively. The solid, dot-dashed, and dashed lines represent MGEP predictions for source types C, U, and X respectively. The absorbed fractions are computed as

$$P_{abs} = \left\{ \begin{array}{ll} 1 - \mathcal{P}_{esc}^c(\tau_{eff}, \omega_{eff}, g_{eff}) & [\text{C, eq.(79)}] \\ 1 - \mathcal{P}_{esc}^u(\tau_{eff}, \omega_{eff}) & [\text{U, eq.(80)}] \\ \mathcal{P}_{abs}^x(\tau_{eff}, \omega_{eff}) & [\text{X, eq.(83)}] \end{array} \right\}$$

for each indicated source type. The fractions absorbed by the ICM, A_{icm} , are computed by equations (76), (77), and (78) for source types C, U, and X, respectively. The MGEP model agrees with the MCRT results, showing the same behavior for each source type. Figure 18 compares the same quantities for $f_c = 0.3$. The MGEP model predicts a total absorbed fraction (top panel) for source type X greater than the MCRT results when $\tau_{hom} > 10$, probably

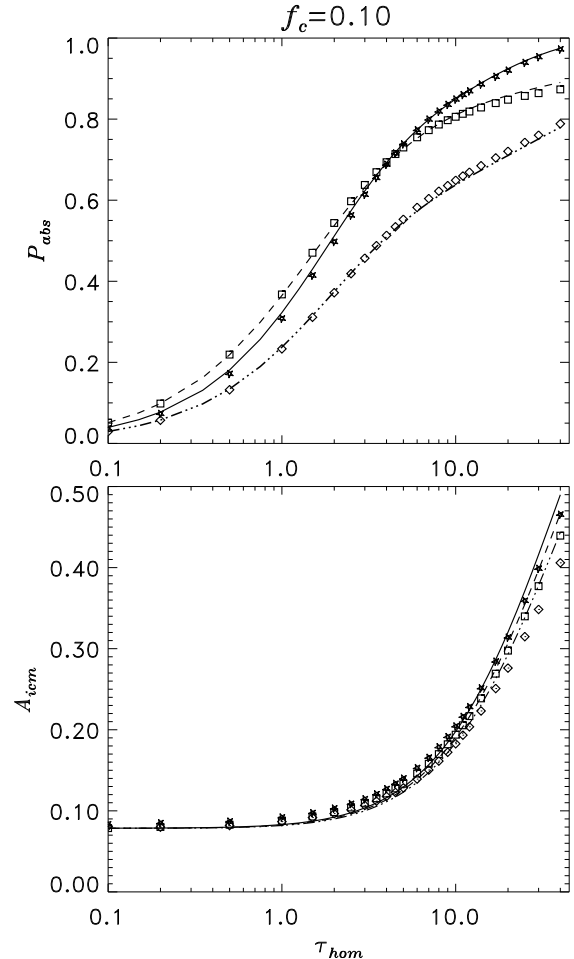


Fig. 17.— Comparison of MGEP absorption probabilities to MCRT absorbed fractions as function of τ_{hom} , with $f_c = 0.1$, $\alpha = 100$, and $r_c = 0.05$. The top panel shows the total absorbed fractions whereas the bottom panel shows the fraction of the total which is absorbed by the ICM. Scattering parameters are $\omega_d = 0.6$ and $g_d = 0.6$. The star, diamond, and square symbols represent MCRT results for source types C, U, and X, respectively. The solid, dot-dashed, and dashed lines represent MGEP results for source types C, U, and X.

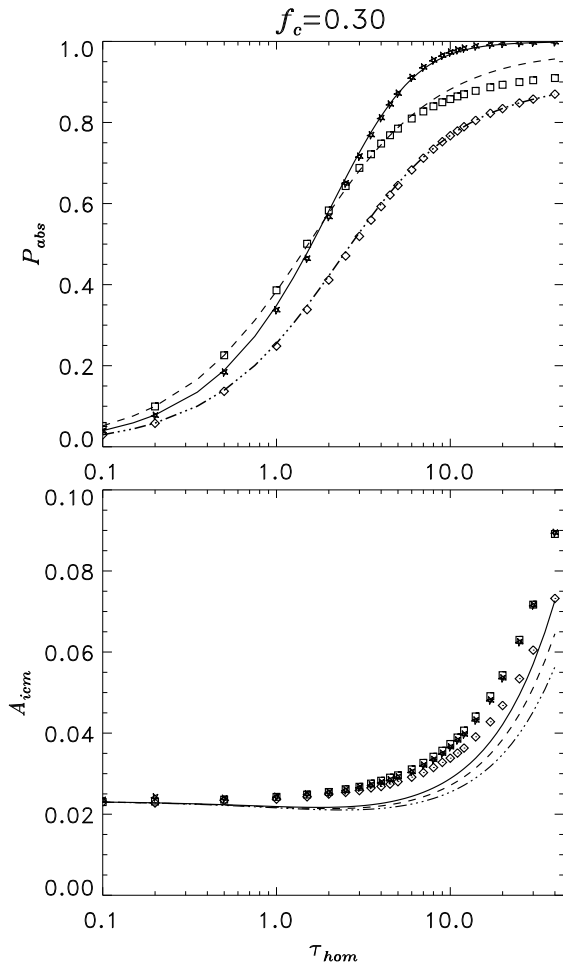


Fig. 18.— Same as Figure 17, but for $f_c = 0.3$.

due to limitations of the assumptions used in deriving eq.(29) for \mathcal{P}_{abs}^x . For this case of $f_c = 0.3$ (and actually for $f_c > 0.1$) the MGEF model predicts values for A_{icm} (bottom panel) that are lower than the MCRT results. When $f_c < 0.1$ the absorbed ICM fractions predicted by MGEF are slightly higher than the MCRT results. Overall, the agreement is acceptable and the MGEF model exhibits the same behavior as the MCRT simulations.

6.2. Dependence on Filling Factor

We next compare MGEF and MCRT results as a function of the clump filling factor f_c , holding other parameters fixed. Figures 19 and 20 compare MCRT and MGEF predictions of the fraction of emitted photons that are absorbed in the medium, P_{abs} , in the top panels, and the fraction of the total absorbed photons that are absorbed in the ICM, A_{icm} , in the bottom panels, as function of f_c , with scattering parameters $\omega_d = 0.6$ and $g_d = 0.6$. Figure 19 is for the case of $\tau_{hom} = 2$ and Figure 20 is for $\tau_{hom} = 10$ (note the different ranges for P_{abs} axis). The star, diamond, and square symbols represent MCRT numerical results for source types C, U, and X, respectively. The solid, dot-dashed, and dashed lines represent MGEF analytical results for source types C, U, and X, respectively. The analytical MGEF theory agrees well with the MCRT numerical results, with the exception of the absorbed fraction of a uniformly illuminating external source with scattering. For that case of source type X, when τ_{hom} is large and $f_c \rightarrow 1$ the MGEF theory overestimates the absorbed fraction with a difference that increases with f_c . This is probably because the assumption of uniformly distributed photons after first scattering (see §3.4) becomes invalid as $\tau_{hom} \rightarrow \infty$ since then the externally impacting photons do not penetrate the sphere.

The dotted line and the triangles in the bottom panels represent MGEF and MCRT results, respectively, for the case of no scattering ($\omega_d = 0$). The effect of turning on scattering is to decrease the fraction of photons absorbed in the ICM, since photons scattered by the ICM then have more of a chance of getting absorbed in the denser clumps. The MGEF model tends to overestimate A_{icm} at low clump filling factors and underestimate A_{icm} at high filling factors, with best agreement at about $f_c = 0.1$. However, the MGEF theory gives the same variation of A_{icm} with f_c as the MCRT simulations, and overall the agreement is acceptable.

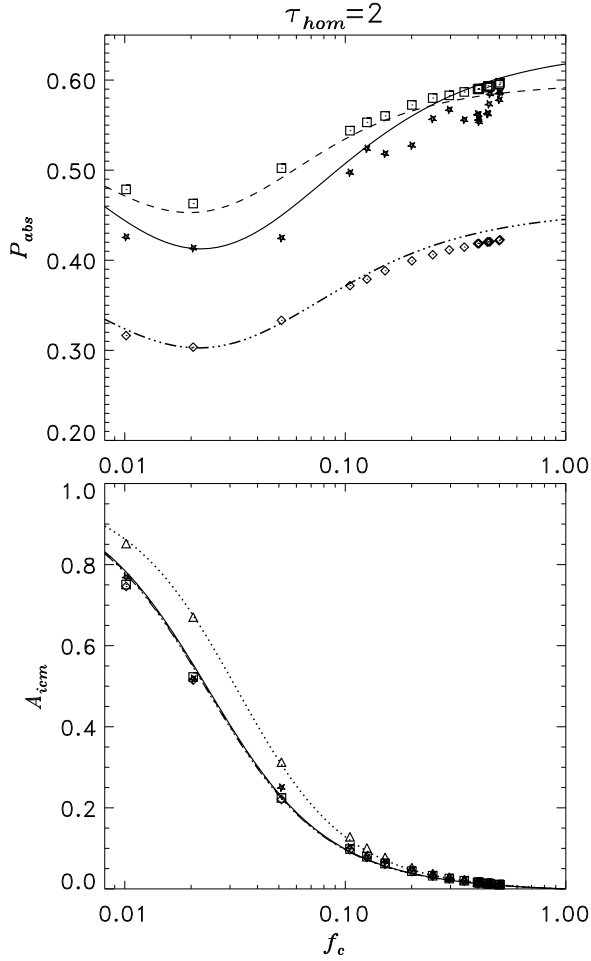


Fig. 19.— Comparison of MGEF absorption probabilities to MCRT absorbed fractions as function of f_c , with $\tau_{hom} = 2$, $\alpha = 100$, and $r_c = 0.05$. Scattering parameters are $\omega_d = 0.6$ and $g_d = 0.6$. The star, diamond, and square symbols represent MCRT results for source types C, U, and X, respectively. The solid, dot-dashed, and dashed lines represent MGEF results for source types C, U, and X. The dotted line and the triangles represent MGEF and MCRT results, respectively, for the case of no scattering.

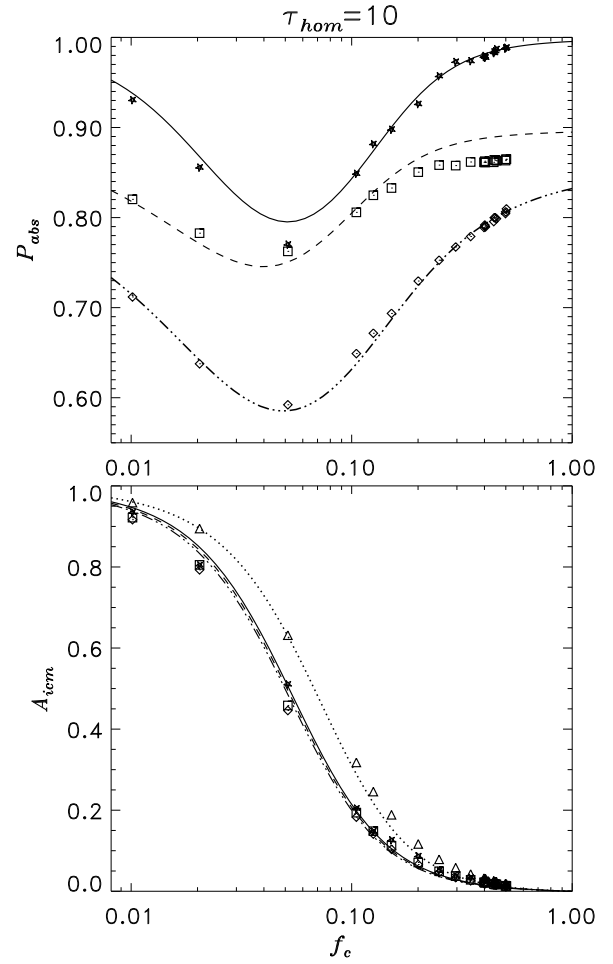


Fig. 20.— Same as Figure 19, but for $\tau_{hom} = 10$.

6.3. Dependence on Density Ratio

Finally, we compare MGEP and MCRT as a function of the clump to ICM density ratio, $\alpha = \rho_c / \rho_{icm}$, holding other parameters fixed. Figure 21 shows the effective optical depth (τ_{eff} or τ_S) for source type C (top row), the escaping fraction of photons (\mathcal{P}_{esc}^u) from source type U (second row), the fractions absorbed by the ICM for source type C (A_{icm}^c in third row), and for source type U (A_{icm}^u in fourth row), all as a function of α , for the cases of $f_c = 0.1, 0.5$, and 0.9 as indicated, with $\tau_{hom} = 10$. The square and diamond symbols indicate MCRT results for no scattering ($\omega_d = 0$) and with scattering (for $\omega_d = 0.6$ and $g_d = 0.6$), respectively. The solid and dashed lines indicate MGEP predictions with and without scattering, respectively. The value $\alpha = 1$ corresponds to a homogeneous medium, and then $\tau_{eff} = \tau_{hom}$ when $\omega_d = 0$. Values of $\alpha < 1$ show the case of spherical cavities in a denser ICM. For the case of denser clumps ($\alpha > 1$), most of the variation in τ_{eff} , τ_S , and \mathcal{P}_{esc}^u occurs for $1 < \alpha < 100$ because in this range the clumps go from being optically thin to thick, and for $\alpha > 100$ the clumps are essentially opaque. Turning on scattering decreases the effective optical depth and allows more photons to escape, but this effect is diminished as $\alpha \rightarrow \infty$, and is correctly predicted by the MGEP model. The reason for the diminished effects of scattering is that ω_{eff} and g_{eff} (not shown) decrease by more than a factor of two as $\alpha \rightarrow \infty$.

Applying the MGEP model to the case of spherical cavities ($\alpha < 1$) is accomplished by the inversion transform of eq.(88), which then regards the cavities as the ICM and the rest of the medium as clumps. This is not the intended application of the mega-grains approximation, since there are then actually no isolated clumps, but there is some indication that the MGEP model could be tailored to give a reasonable approximation of the escaping radiation. When $f_c = 0.9$ we see that the MGEP model does not give correct predictions for $\alpha < 1$, the case of spherical cavities. This is understandable, because when the cavities occupy 90% of the volume, the high density regions are just shells between the cavities, which are not well approximated by clumps having the same radius as the cavities (recall $r_c = 0.05$). Choosing a smaller value for r_c would improve the MGEP approximation of the MCRT results. The MGEP model provides an acceptable approximation of the MCRT results for $\alpha \geq 1$. When $f_c = 0.5$ and as $\alpha \rightarrow \infty$ there is an increasing difference between MGEP and MCRT

results in the case of a central source, but this can be attributed to the specific realization of the clump locations relative to the source: there is a 50% chance that the point source will be inside a clump (as in this case), causing an increase of the optical depth in the MCRT simulation. Other simulations for the same filling factor give MCRT results that are less than the MGEP predictions, so we expect that on average the MGEP predictions will be close to MCRT results.

The fractions absorbed by the ICM are shown in the third and bottom rows of Figure 21 for source types C and U, respectively. The intersection of the horizontal and vertical dotted lines indicate the nominal value of A_{icm}^u expected as the medium becomes homogeneous, since then the fraction photons absorbed by the ICM should be $1 - f_c$ of the total absorbed photons. For the case of when the clumps are denser than the ICM ($\alpha > 1$) the MGEP model agrees well with the MCRT results, when the source is uniformly distributed. When the source is at a central point and $f_c = 0.5$ the MGEP predictions are less than the MCRT results, and this can be attributed to the fact that the point source happens to be in a clump, as discussed above. Note that the MGEP model correctly predicts that turning on scattering causes less photons to be absorbed by the ICM and more to be absorbed in clumps. When $\alpha < 1$ the MGEP model predicts values lower than MCRT for $f_c > 0.3$, since the MGA was not actually formulated for this application, but the MGEP model does exhibit the correct behavior.

6.4. Body Centered Cubic Lattice of Clumps

The mega-grains approximation can be applied to the case of cubic clumps randomly located on a body centered cubic (BCC) lattice with partial success. The BCC lattice was used by Witt & Gordon (1996) in their Monte Carlo simulations. For source type U, the MGEP model does predict the same escaping fraction computed by MCRT when $r_c = 1/N = 0.05$, where $N = 20$ is the number of grid element along each axis of the lattice. However, this value of r_c in the MGEP model gives erroneous predictions for the effective optical depth seen by a central source. The problem is related to the fact that the apparent projected area of a cubic clump depends on the viewing angle. To match the MGEP model with MCRT results for source type C, we need to use $r_c \simeq \sqrt{2}/N = 0.071$ in the mega-grains equations, but then the predictions for source type U are wrong.

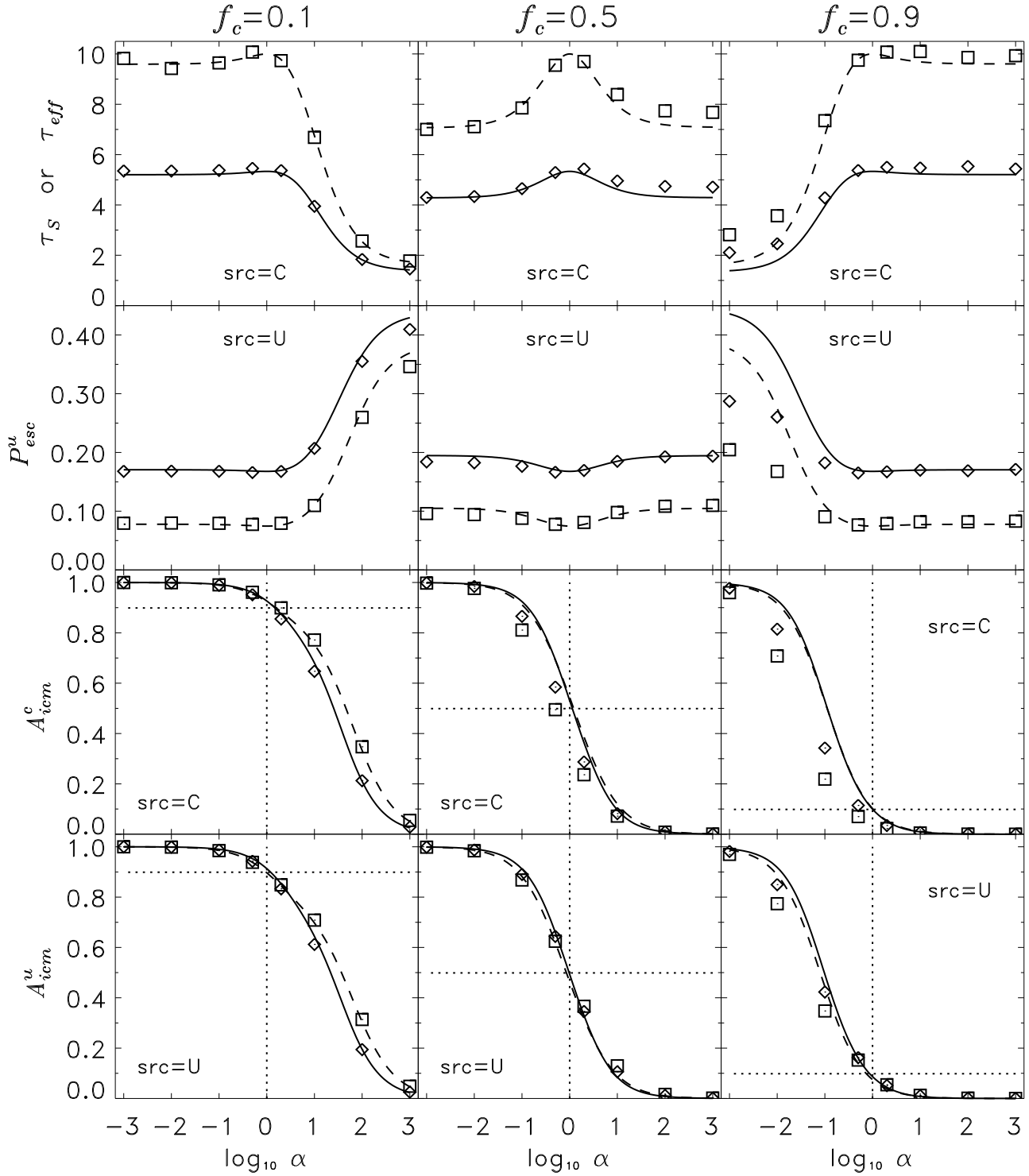


Fig. 21.— Comparison of MGEP and MCRT results as function of $\alpha = \rho_c/\rho_{icm}$ for three values of $f_c = 0.1, 0.5,$ and 0.9 , as indicated, with $\tau_{hom} = 10$ and $r_c = 0.05$. See §6.3 for more information.

7. MODELING THE ABSORPTION OF STELLAR RADIATION BY DUST AND THE INFRARED EMISSION

In this section we model the transfer of a spectrum of radiation in a two-phase clumpy medium, from emission by stellar-like sources to the absorption and scattering by dust and the resulting infrared emission from dust heated by the absorbed radiation. Both detailed Monte Carlo simulations and the analytical approximations developed in previous sections are used to model the transfer of radiation, and the emerging spectral energy distribution (SED) from the two methods of modeling are compared. We shall again use the acronyms MCRT when referring to the Monte Carlo radiative transfer model, and MGEP when referring to the mega-grains approximations combined with escape/absorption probability formulae.

The dust is assumed to be composed of 40% graphite and 60% silicates by mass, and to have the grain size distribution

$$\zeta(a) \propto a^{-3.5}, \quad (89)$$

normalized over the following range of grain sizes:

$$0.001\mu\text{m} < a < 0.25\mu\text{m}. \quad (90)$$

Using the optical constants from Draine (1985), we applied Mie theory to calculate the absorption and scattering efficiencies of dust grains, $Q_{abs}(a, \lambda)$ and $Q_{scat}(a, \lambda)$ respectively, as a function of grain size, a , and photon wavelength λ . The scattering asymmetry parameters, $g(a, \lambda) = \langle \cos \theta_{scat}(a, \lambda) \rangle$, were also calculated by averaging with respect to the distribution of scattering angles. Then the cross-sections and asymmetry parameters were averaged with respect to the grain size distribution to get the mass absorption and scattering coefficients and average asymmetry parameters used in the models:

$$\begin{aligned} \kappa_{abs}(\lambda) &\equiv \frac{\langle \pi a^2 Q_{abs}(a, \lambda) \rangle_a}{\langle m_g \rangle_a} \quad (91) \\ \kappa_{scat}(\lambda) &\equiv \frac{\langle \pi a^2 Q_{scat}(a, \lambda) \rangle_a}{\langle m_g \rangle_a} \\ g_d(\lambda) &\equiv \frac{\langle g(a, \lambda) \pi a^2 Q_{scat}(a, \lambda) \rangle_a}{\langle \pi a^2 Q_{scat}(a, \lambda) \rangle_a}, \end{aligned}$$

where the averaging operator is defined as

$$\langle \cdot \rangle_a \equiv \int_{a_{\min}}^{a_{\max}} (\cdot) \zeta(a) da, \quad (92)$$

and the average grain mass is

$$\langle m_g \rangle_a \equiv \left\langle \frac{4}{3} \pi a^3 \rho \right\rangle_a, \quad (93)$$

where ρ is the mass density of a graphite or silicate grain. All the following simulations have the same total dust mass of $1.01 M_\odot$ contained in spherical region 1pc in radius. This corresponds to a dust mass density of $\rho_{hom} = 1.63 \times 10^{-23} \text{ gm/cm}^3$ in the homogeneous case, equivalent to a gas density of 1000 cm^{-3} with a dust to gas mass ratio of 0.007, giving a homogeneous optical depth of $\tau_V = 1.67$ in the V-band.

Before discussing the results of the MCRT and MGEP simulations, we illustrate how the degree of clumpiness in the distribution of dust is as important as the total dust mass and scattering albedo in affecting the transfer of radiation through the medium. Figure 22 compares as a function of wavelength, (a) the effective optical depth, $\tau_{eff}(\lambda)$, (b) the effective albedo, $\omega_{eff}(\lambda)$, and (c) the effective asymmetry parameter, $g_{eff}(\lambda)$, of a spherical region of dust with different degrees of clumpiness, computed using the mega-grains equations listed in §5, with $R_S = 1\text{pc}$, $\rho_{hom} = 1.63 \times 10^{-23} \text{ gm/cm}^3$, and

$$\begin{aligned} \kappa(\lambda) &= \kappa_{abs}(\lambda) + \kappa_{scat}(\lambda) \\ \omega_d(\lambda) &= \kappa_{scat}(\lambda) / \kappa(\lambda). \end{aligned} \quad (94)$$

The solid curves in Figure 22 shows the homogeneous case, giving $\tau_V = 1.67$. The dashed curves are for the case $f_c = 0.1$ with $\alpha = \rho_c / \rho_{icm} = 100$, and clump radii $r_c = 0.05\text{pc}$, giving $\tau_V = 1.11$. The dotted curves are for the extreme case of $f_c = 0.01$ with $\alpha = 10^4$, and $r_c = 0.01\text{pc}$, giving $\tau_V = 0.66$. It is evident that the effective radiative transfer properties of the dusty medium can be radically affected by the degree of clumpiness. The effect is greatest at shorter wavelengths where the dust absorption and scattering coefficient is sufficiently large to make the clumps, opaque causing $\tau_{eff}(\lambda)$ to become almost flat and featureless. The small features remaining are due to the ICM, but the opaque clumps dominate the effective optical depth. An explanation for this ‘‘gray’’ behavior when $\tau_c(\lambda) \gg 1$ is obtained by using eq.(61):

$$\begin{aligned} \frac{\partial \tau_{eff}}{\partial \lambda} &= \frac{\partial \tau_{eff}}{\partial \tau_{hom}} \frac{\partial \tau_{hom}}{\partial \lambda} \quad (95) \\ &\approx \left(\frac{1}{\alpha f_c} \right) \frac{\partial \tau_{hom}}{\partial \lambda} \ll \frac{\partial \tau_{hom}}{\partial \lambda}. \end{aligned}$$

Thus, as $\alpha f_c \rightarrow \infty$ the variation of $\tau_{eff}(\lambda)$ for the clumpy medium becomes a small fraction of the

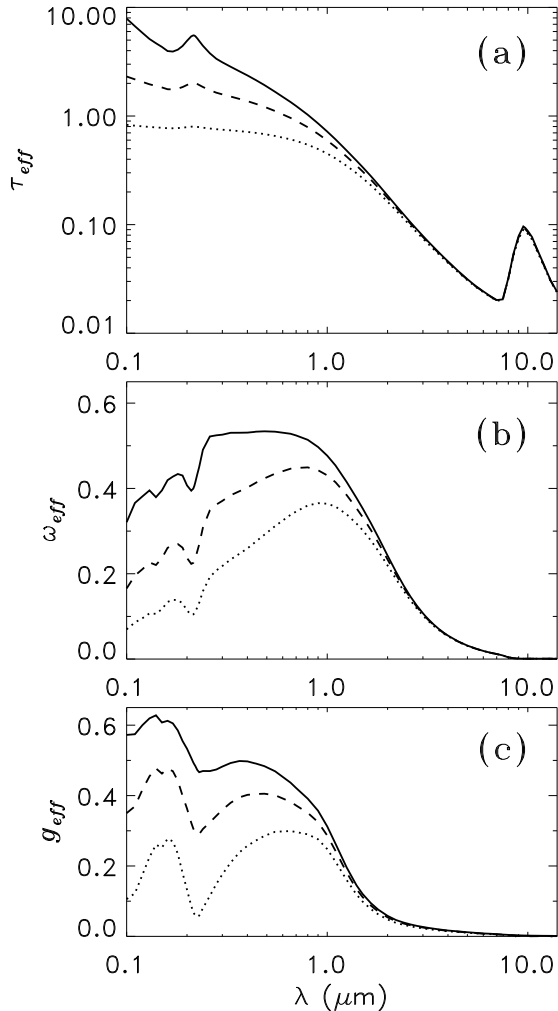


Fig. 22.— Comparison of radiative transfer properties of dust distributed homogeneously or in clumps. Panels show effective values of (a) optical depth, (b) albedo, and (c) scattering asymmetry parameter, versus wavelength, computed using the mega-grains approximation. For comparison, the solid curves show the dust optical parameters for the equivalent homogeneous medium. The dashed curves show effective optical parameters for a two-phase clumpy medium with filling factor $f_c = 0.1$, clump radii $r_c = 0.05\text{pc}$ (843 clumps), and clump to ICM density ratio of $\alpha = \rho_c/\rho_{icm} = 10^2$. The dotted curves show the case of $f_c = 0.01$, $r_c = 0.01\text{pc}$ (9918 clumps), and $\alpha = 10^4$. See §7 for more information.

variation of $\tau_{hom}(\lambda)$ in the equivalent homogeneous medium. For longer wavelengths (infrared) there is no difference between clumpy and homogeneous media because the clumps are optically thin.

To test the MGEP model using MCRT, we simulated a two-phase clumpy medium with $f_c = 0.1$, $\alpha = 100$, and $r_c = 0.05\text{pc}$, so that the effective optical depths, albedos, and asymmetry parameters used in all the MGEP calculations are given by the dashed curves in Figure 22. The MCRT computations always use the optical parameters given by the homogeneous case (solid curves) in Figure 22, simulating the details of the clumpy medium on a 3D grid of 127^3 voxels. The radiation source in all cases is a black-body spectrum with $T_s = 15000\text{K}$ and $L_s = 33000L_\odot$, so the spectrum of the emitted flux is

$$S_\lambda = \frac{L_s}{\sigma T_s^4} B_\lambda(T_s). \quad (96)$$

The transfer of radiation is computed by MCRT at 40 wavelengths from $\lambda_{\min} = 0.1\mu\text{m}$ to $\lambda_{\max} = 14\mu\text{m}$, following 10^7 photons at each wavelength. The standard three types of source geometries are studied: uniformly distributed internal emission (U), uniformly illuminating external source (X), and a central isotropic point source (C).

7.1. Absorbed Luminosities and the Distribution of Dust Temperatures

Since we model only non-ionizing photons experiencing coherent scattering, for a given type of source the radiative transfer of a unit emitted flux can be simulated at each wavelength separately, giving an escape and absorption response function for the particular choice of source, geometry, and clumpiness. Then we multiply the chosen source spectrum with the escape/absorption response function to get the actual escaping SED and the luminosity absorbed by each component of the dust. In the case of Monte Carlo simulations (MCRT) we obtain the 3D spatial distribution of the absorbed luminosity, whereas using the analytical approximations (MGEP) gives the luminosity absorbed by all the clumps and luminosity absorbed by the ICM. The equilibrium dust temperatures, T_d for graphite or silicate, are computed by equating the absorbed and emitted luminosities:

$$\int_{\lambda_{\min}}^{\lambda_{\max}} S_\lambda P_{abs}(\lambda) d\lambda = 4\pi m_d \int_0^\infty \kappa_\lambda B_\lambda(T_d) d\lambda, \quad (97)$$

where $P_{abs}(\lambda)$ generically represents the fraction of flux at wavelength λ absorbed by graphite or silicate in a particular 3D voxel of mass m_d in the case of MCRT, or it is the fraction absorbed by graphite or silicate in either the ICM or the clumps of mass m_d in the case of MGEP. The energy conservation eq.(97) is solved iteratively for T_d using Brent's method of finding the zeros of a function (Press et al. 1992), giving a 3D distribution of dust temperatures for MCRT, or the average temperatures of the dust in clumps and the ICM when using the MGEP model.

Figure 23 shows the distribution of equilibrium dust temperatures computed by the MCRT model for clumps (top row) and in the ICM (bottom row), for source types U, X, and C in each column from left to right. The solid lines are the probability densities of graphite dust temperatures and the dotted lines represent silicate dust. For the cases of uniformly distributed internal and external sources the probability densities are Gaussian on the high temperature side and of exponential form on the low temperature side (note slightly different temperature scales). In contrast, the central source creates a power law distribution of temperatures (third column is a log-log plot) since dust next to the source is heated much more than dust farther from the center. In fact, the straight lines in Figure 23 are power laws: the solid line is T_d^{-8} and appears to be parallel to the graphite temperature distribution whereas T_d^{-9} (dashed line) is parallel to the temperature distribution of silicates.

Table 1 compares the luminosities absorbed by each component (graphite or silicates) and phase (ICM or clumps) of the medium, as computed by the MCRT and MGEP models, again for the cases of uniform internal, uniform external, and central source. The MGEP results were obtained by computing the escaping and absorbed SED using the mega-grains equations and the escape/absorption probability formulae, combined with formulae for the fractions absorbed by the ICM and clumps, given in §4.5. Also compared in Table 1 are the resulting dust temperatures: averages of the distributions shown in Figure 23 for the case of MCRT simulations, and in the case of the MGEP model when the source is not a central point source, a single temperature for each component and phase computed using eq.(97).

To compute the average temperature of the dust in the case of a central source we use a theoretical power law distribution of dust temperatures as described in Appendix E, along with two assumptions:

that the absorbed luminosity decays with radial distance from the source like an inverse power law with index $\eta = 2.5$ ($\eta = 2$ is normal for optically thin case), and we use the maximum dust temperatures found by MCRT in the voxel containing the source. Normally the maximum temperature would be the dust sublimation temperature, however, the MCRT simulation is not set up to fully resolve the volume next to the source so the sublimation temperature is not reached in the simulation. Since we are comparing with MCRT results we chose to use those maximum temperatures. We then solve for minimum temperature of the power law distribution which matches the emitted and absorbed luminosities, and this also yields the average dust temperature.

Table 1 shows that the MCRT and MGEP results are in close agreement. The uniformly illuminating external source experiences more absorption (67%) than the uniformly distributed internal emission (49%) and therefore heats the dust to slightly higher temperatures. Approximately the same fractions of luminosity are absorbed in the central and external source cases, but the average dust temperature is lower in the central source case since most of the dust is far from the source. In all cases the clumps absorb about seven times more energy than the ICM, and this is in part due to the fact that the clumps contain more than ten times the mass of the ICM:

$$\frac{M_c}{M_{icm}} = \frac{\rho_c f_c V}{\rho_{icm}(1 - f_c)V} = \frac{\alpha f_c}{1 - f_c} \quad , \quad (98)$$

and this ratio is greater than ten for $f_c = 0.1$ and $\alpha = 100$. However, the larger mass can easily radiate the absorbed energy in the IR so that the temperature of dust in clumps is generally lower than in the ICM. In §7.3 we study in more detail the reasons for the lower temperatures of dust in clumps.

TABLE 1
COMPARISON OF DUST ENERGETICS AND TEMPERATURES

source	dust	phase	L_{abs} ($10^3 L_{\odot}$)		T_{dust} (K)	
			MCRT	MGEP	MCRT	MGEP
U	graphite	ICM	1.66	1.56	45.8	45.7
		Clumps	11.55	11.54	41.9	42.2
	silicates	ICM	0.44	0.42	37.0	37.0
		Clumps	2.75	2.74	33.4	33.6
	total	$L_{abs}/L_s =$	49%	49%		
X	graphite	ICM	2.33	2.19	48.7	48.5
		Clumps	15.70	15.86	44.2	44.6
	silicates	ICM	0.62	0.58	39.0	39.0
		Clumps	3.66	3.69	34.9	35.3
	total	$L_{abs}/L_s =$	67%	67%		
C	graphite	ICM	2.40	2.21	41.3	42.8
		Clumps	15.16	15.48	37.9	39.9
	silicates	ICM	0.64	0.59	32.4	34.8
		Clumps	3.57	3.63	29.3	31.9
	total	$L_{abs}/L_s =$	65%	66%		

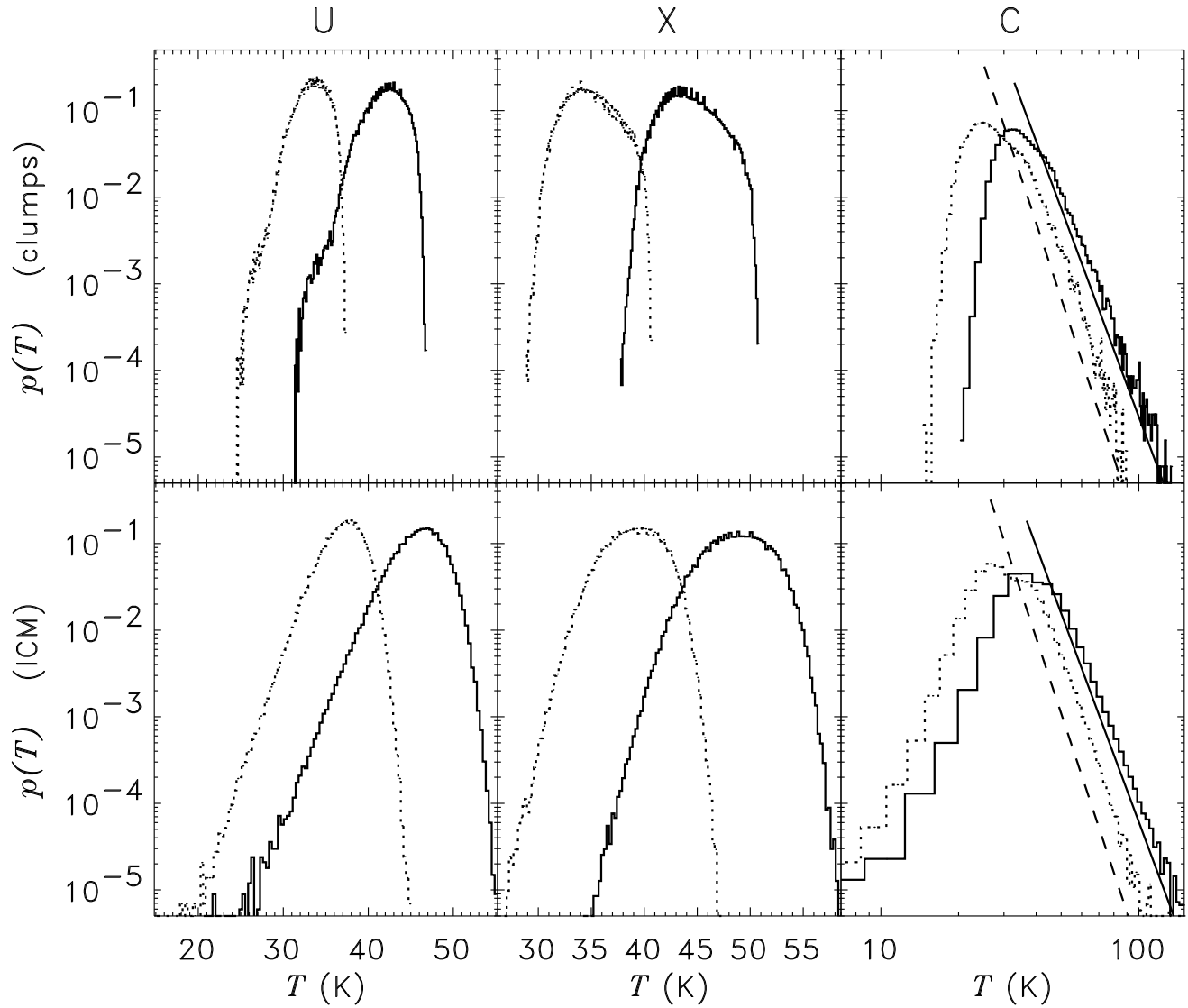


Fig. 23.— Probability distribution of equilibrium dust temperatures from MCRT simulations for each type of source (indicated at top), in a clumpy medium with $f_c = 0.1$, $\alpha = 100$, and $r_c = 0.05$. The top row represents the temperature distribution of dust in clumps and the bottom row that for the ICM. The solid lines are for graphite and the dotted lines are for silicates. See §7.1 for more information.

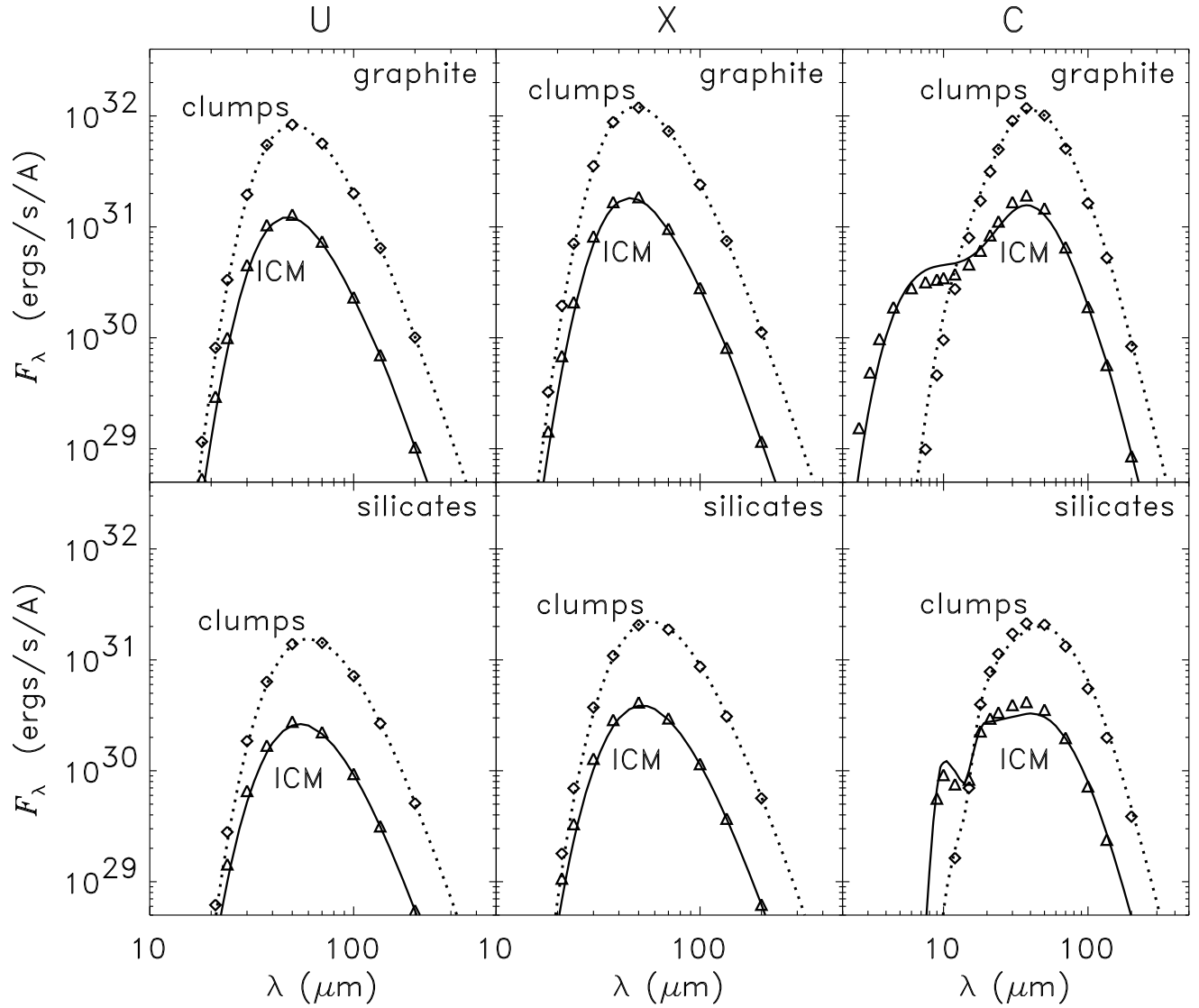


Fig. 24.— Comparison of dust emission spectra from MCRT and MGEP models for each type of source: U, X, C, from left to right (indicated at top). The clumpy medium has $f_c = 0.1$, $\alpha = 100$, and $r_c = 0.05$. The top row is for graphite, bottom row is for silicates. The triangles are for the MCRT model of dust in ICM and the diamonds are for dust in clumps. The solid lines are for the MGEP model of dust in ICM and the dotted lines are for dust in clumps. See §7.2 for more information.

7.2. The Emerging UV-FIR SED

Computation of the dust temperatures also gives the IR emission from dust in each voxel of the 3D simulation by the MCRT model, or from each phase of the medium in the MGEP model:

$$F_\lambda = 4\pi m_d \kappa(\lambda) B_\lambda(T_d), \quad (99)$$

where T_d is the temperature of dust in a voxel of mass m_d in the MCRT model, or where T_d is the temperature of a dust in clumps/ICM of mass m_d in the MGEP model. Equation (99) is used by the MGEP model only for uniformly distributed internal or external sources. In the case of a central source with a power law distribution, $p(T_d)$, of dust temperatures, the MGEP model essentially computes

$$F_\lambda = 4\pi m_d \kappa(\lambda) \int_{T_{\min}}^{T_{\max}} B_\lambda(T) p(T) dT, \quad (100)$$

an approximation which is described in more detail in Appendix E. Integrating the IR emission over the 3D volume in the case of the MCRT approach, or just adding the IR emission from the clumps and ICM in the case of the MGEP approach, gives the total IR emission spectrum. Figure 24 shows the IR emission spectra from graphite (top row) and silicates (bottom row), with the diamonds and triangles representing emission from clumps and the ICM, respectively, as computed by MCRT, and the solid and dotted lines representing emission from the ICM and clumps as computed by MGEP. The source types U, X, and C, are presented in columns from left to right. The MGEP model is in close agreement with the MCRT results. The emission from the clumps is in general greater than that from the ICM because the absorbed luminosity is larger. An exception is the case of a central source where the heating of dust adjacent to the source to much higher temperatures causes more emission from the ICM at short IR wavelengths.

The emerging SED is the sum of the escaping radiation and the IR emission from heated dust:

$$\lambda E_\lambda = \lambda S_\lambda P_{esc}(\lambda) + \lambda F_\lambda, \quad (101)$$

where $P_{esc}(\lambda)$ generically designates an escape probability which is computed either numerically (MCRT) or analytically (MGEP) and depends on the model and source type. Figure 25 compares the SED computed by the MCRT and MGEP models for each type of source. The diamond symbols are the MCRT results, the solid lines are the MGEP theory, and the

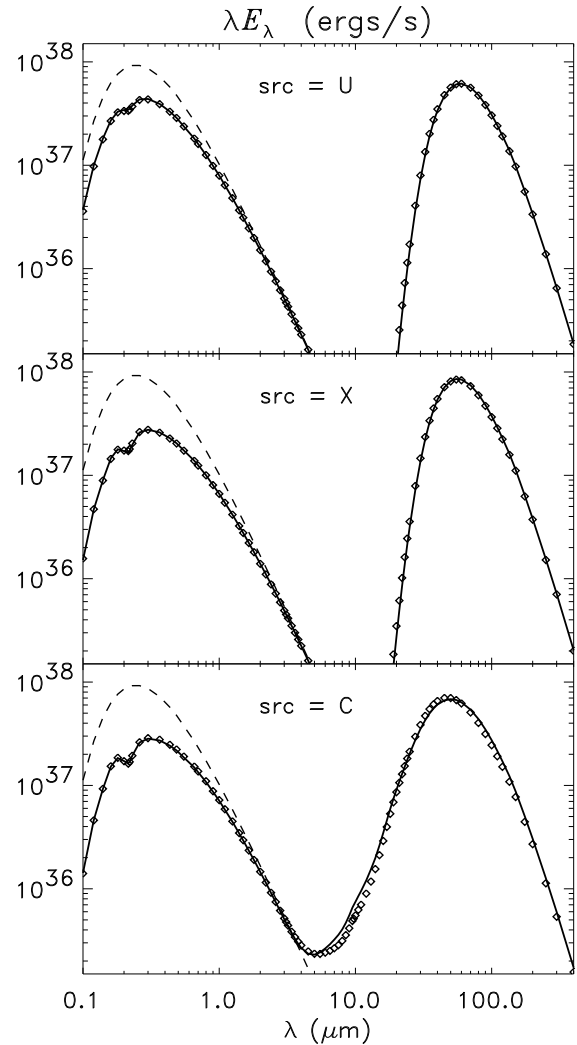


Fig. 25.— Comparison of the emerging UV-FIR SED resulting from the MGEP model (solid lines) and the MCRT model (diamonds). The dashed line is the SED of the source types U, X, and C, from top to bottom rows.

dashed line is the original source spectrum λS_λ . The source types U, X, and C, are presented in panels from top to bottom. The SED at short wavelengths is the source radiation which escapes from the clumpy dusty environment, whereas the SED at long wavelengths is emission from dust heated by the absorbed radiation. The agreement between the MGEP and MCRT models is excellent. The SEDs for the uniform internal and external sources have very similar appearances, except that in the case of an external source more of the source energy is absorbed (68% versus 49%). The central and external source cases have the same fraction of energy absorbed by the dust, so that the short wavelength portion of the SEDs are the same. However, in the case of a central source the emission from hot dust near the source increases the SED around $10\mu\text{m}$. In all cases, the relative paucity of emission in the $\sim 3 - 20\mu\text{m}$ region is caused by the omission of stochastic heating in the calculations.

7.3. Exploring Parameter Space with the MGEP Model

Since the MGEP equations are computationally fast, we can very easily model the escape and absorption of radiation over a wide range of parameters characterizing the clumpy medium or the radiation source. Figures 26 and 27 show the results of MGEP model calculations over the range of clump filling factors, $0.001 < f_c < 1$, and density ratios, $1 < \alpha < 10^4$, with clump radii $r_c = 0.05$. The dust composition and total mass is the same as that used in the above MCRT to MGEP comparisons. The sources of radiation are isotropic and uniformly distributed within the sphere, again having a black-body spectrum with temperature $T_s = 15,000\text{K}$ and total luminosity $L_s = 33,000L_\odot$. In all the panels the diamond and cross marks the point $(\alpha, f_c) = (100, 0.1)$ for which we presented detailed comparisons with MCRT, and the horizontal dotted lines indicate the limiting value of f_c ($=0.0015$) below which there are less than 10 clumps in the medium, therefore, only filling factors above the dotted line are considered to be statistically reliable.

Figure 26 shows (a) the contours of the fraction of the source luminosity which is absorbed by the clumpy medium (L_{abs}/L_s) in the top panel, and (b) the contours of the logarithm of the ratio of luminosity absorbed by the ICM to that absorbed by clumps [$\log(L_{icm}/L_c)$] in the bottom panel. The dashed line (in all panels), extending from $(\alpha, f_c) = (1, 0.5)$ to

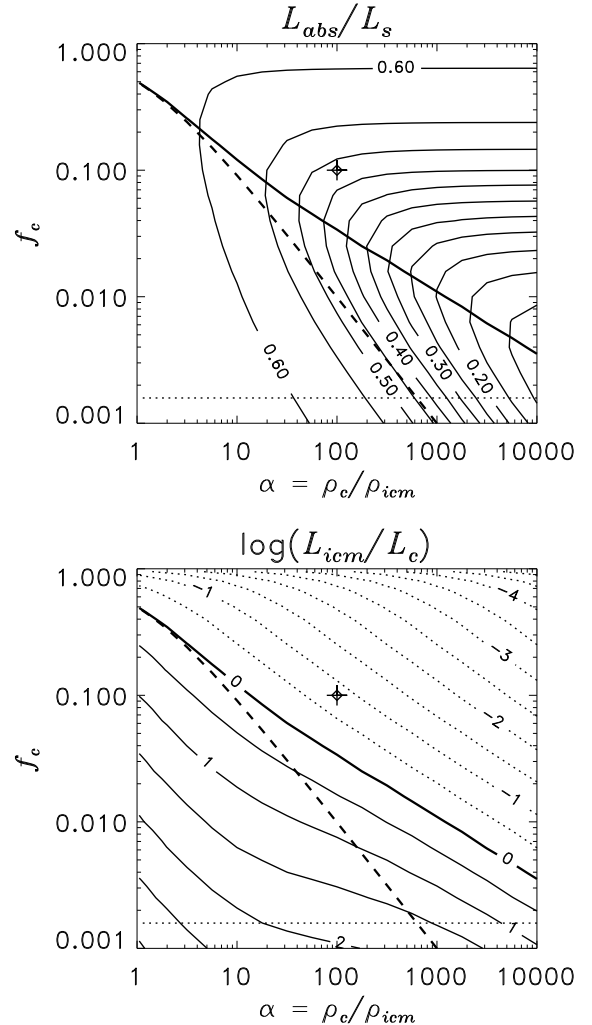


Fig. 26.— Results of the MGEP model over a wide range of clumpy medium parameters (α, f_c) for a uniformly distributed black-body source having $T_s = 15,000\text{K}$ and $L_s = 33,000L_\odot$. (a) Top panel shows absorbed luminosity fraction; (b) and the bottom panel shows the ratio of ICM/clump luminosities. The diamond and cross marks the parameters for which detailed comparisons with MCRT were presented. In both panels the dashed line is the locus of parameters where $M_{icm} = M_c$, and the thick solid line is the locus of parameters where $L_{icm} = L_c$. More details are given in §7.3 of the text.

(1000, 0.001), is the curve

$$f_M(\alpha) = \frac{1}{\alpha + 1}, \quad (102)$$

giving the locus parameters for which the ICM and clumps have equal mass, that is, $M_{icm} = M_c$. The equation for $f_M(\alpha)$ is obtained from eq.(98), which we restate here as

$$M_c = \left(\frac{\alpha f_c}{1 - f_c} \right) M_{icm}. \quad (103)$$

Note that if $f_c > f_M(\alpha)$ then $M_c > M_{icm}$. The thick solid line in all panels represents the locus of parameters $f_L(\alpha)$ for which the ICM and clumps absorb the same amount of energy, that is, $L_{icm} = L_c$. The dotted contours in Figure 26(b) indicate when the ICM absorbs less energy than the clumps. The solid contours in Figure 26(b) indicate that if $f_c < f_L(\alpha)$ then $L_c < L_{icm}$. Combining this with the fact that $M_c > M_{icm}$ when $f_c > f_M(\alpha)$ we have that for the parameter region between the dashed and thick curves

$$f_M(\alpha) < f_c < f_L(\alpha) \Rightarrow \left\{ \begin{array}{l} M_c > M_{icm} \\ L_c < L_{icm} \end{array} \right\}, \quad (104)$$

which guarantees that the temperature of dust in clumps will be less than that in the ICM since, compared to the ICM, a smaller amount of energy is absorbed by a larger number of dust particles, which can radiate this energy at a lower temperature.

Figure 26(a) also shows that for a given density contrast α_0 , the minimum absorbed luminosity (L_{abs}) corresponds to the filling factor $f_c = f_L(\alpha_0)$ for which $L_c = L_{icm}$. When $\alpha \gg 1$, the condition $L_c = L_{icm}$ is achieved when there is approximate equality between the effective optical depth of the clumps and that of the ICM, that is, $\tau_{mg}(\lambda_p) \approx \tau_{icm}(\lambda_p)$, where λ_p is the wavelength where most of the source energy is absorbed. By equation (65), the value of f_c for which $\tau_{mg} \approx \tau_{icm}$ is nearly the same value for which τ_{eff} attains a minimum as a function of f_c (see also Figures 14, 19 and 20). Consequently, as $\alpha \rightarrow \infty$, the steepest descent of L_{abs} is along the curve $f_L(\alpha)$. A detailed derivation of this result and the following equations would require studying τ_{mg} and τ_{icm} as given by eqs.(74) and (75), respectively, but here we assume that the effects of scattering are of second order importance.

Let us study the curve $f_L(\alpha)$ in more detail. As $\alpha \rightarrow 1$ the condition $L_c = L_{icm}$ is achieved by having

$M_c = M_{icm}$, and so $f_L(\alpha) \approx f_M(\alpha)$ when $\alpha < 5$, as shown by the merging of the dashed and thick curves in in Figure 26. However, as $\alpha \rightarrow \infty$ we see that $f_L(\alpha) \gg f_M(\alpha)$. This behavior is due to the change in the effective optical depth of the clumps, τ_{mg} , since the clumps become optically thick as $\alpha \rightarrow \infty$, so we derive an equation for $f_L(\alpha)$ as follows. Starting with $\tau_{mg}(\lambda_p) = \tau_{icm}(\lambda_p)$ and applying the mega-grains equations from §5 we obtain

$$\frac{3f_c}{4r_c(1-f_c)^\gamma} = \frac{\kappa(\lambda_p)\rho_{hom}}{(\alpha-1)f_c+1}, \quad (105)$$

assuming optically thick clumps. Since we propose that eq.(105) occurs when $L_c = L_{icm}$ we now use the symbol f_L in place of f_c for the solution. Then as $\alpha \rightarrow \infty$ we know that $f_L \ll 1$ but $\alpha f_L \gg 1$, so eq.(105) becomes

$$\frac{3f_L}{4r_c} \approx \frac{\kappa(\lambda_p)\rho_{hom}}{\alpha f_L}. \quad (106)$$

Solving for f_L gives

$$f_L(\alpha) \approx \sqrt{\frac{4r_c\kappa(\lambda_p)\rho_{hom}}{3\alpha}} \quad (107)$$

when α is large. Using $\kappa(\lambda_p)\rho_{hom} = 1.7$, which occurs when $\lambda_p \sim 0.55\mu\text{m}$, gives $f_L(\alpha) \approx \frac{1}{3}\alpha^{-\frac{1}{2}}$ which produces a perfect fit to the zero contour of $\log(L_{icm}/L_c)$ in Figure 26(b) when $\alpha > 30$ (not shown). The transition from the behavior $f_L(\alpha) \approx f_M(\alpha)$ to the behavior $f_L(\alpha) \propto \alpha^{-\frac{1}{2}}$ occurs naturally around values of α for which eq.(107) is greater than $f_M(\alpha)$, indicating that the clumps are becoming optically thick. We find that the same value of $\kappa(\lambda_p)\rho_{hom} = 1.7$ in eq.(107) gives perfect fits to the large α behavior of $f_L(\alpha)$ for all $0.1 \leq r_c \leq 0.8$ (not shown).

Figure 27 shows contours of the temperature of graphite dust in the ICM (T_{icm} , top panel), in the clumps (T_c , middle panel), and the temperature ratio, T_{icm}/T_c (bottom panel). The thick solid lines are the curves $f_L(\alpha)$ for which $L_c = L_{icm}$ and the dashed lines are the curves $f_M(\alpha)$ for which $M_c = M_{icm}$. The contours of T_{icm} wrap around $f_L(\alpha)$, whereas the contours of T_c wrap around $f_M(\alpha)$. As $\alpha \rightarrow \infty$ and $f_c \rightarrow 0$, we find that T_c decreases whereas T_{icm} increases slightly. From the relation $L \propto MT^{4+\beta}$, where β is the emissivity index, we get that

$$\frac{T_{icm}}{T_c} = \left[\left(\frac{M_c}{M_{icm}} \right) \left(\frac{L_{icm}}{L_c} \right) \right]^{\frac{1}{4+\beta}}, \quad (108)$$

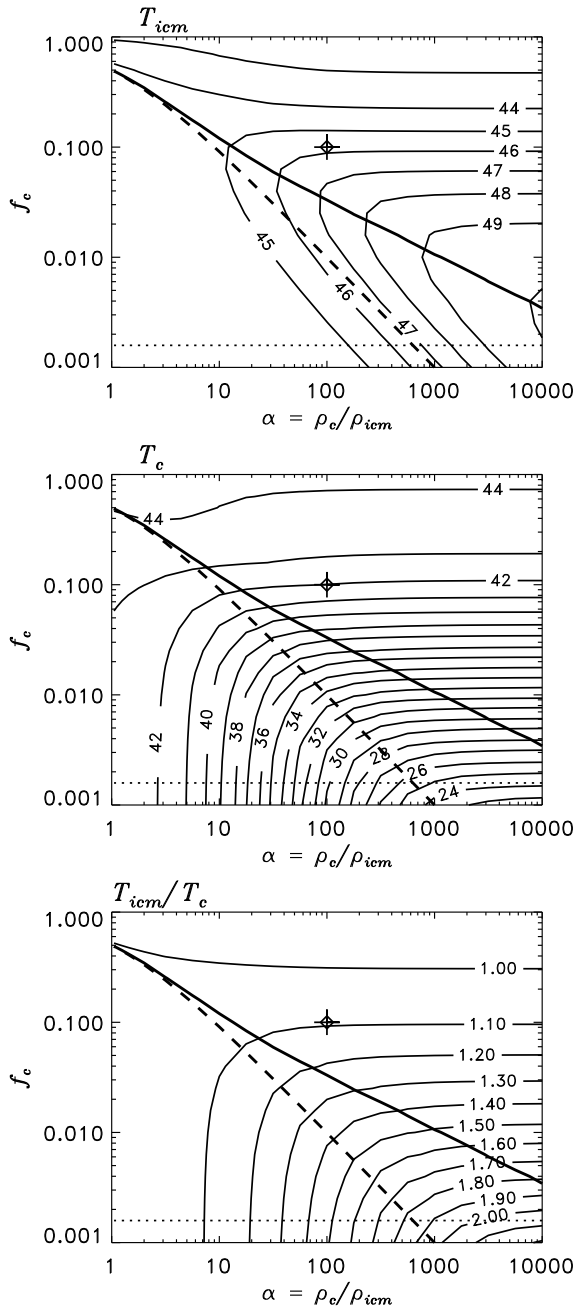


Fig. 27.— Temperatures of graphite dust heated by uniformly distributed sources, as computed by the MGEP model over a wide range of clumpy medium parameters (α, f_c). The top, middle, bottom panels show temperatures in the ICM, the clumps, and the ratio, respectively. The diamond and cross indicate results that were compared with MCRT.

and with the conditions in eq.(104), this equation explains why the condition $f_M(\alpha) < f_c < f_L(\alpha)$ leads to $T_c < T_{icm}$. We can also explain why the temperature ratio must increase as $\alpha \rightarrow \infty$. Substituting eq.(107) into eq.(103) gives

$$\frac{M_c}{M_{icm}} \approx C\sqrt{\alpha} \quad (109)$$

along the $f_L(\alpha)$ curve, where $L_c = L_{icm}$ and where C is a constant. Using this in eq.(108) we get that along the $f_L(\alpha)$ curve

$$\frac{T_{icm}}{T_c} \approx (C\sqrt{\alpha})^{\frac{1}{4+\beta}}. \quad (110)$$

Therefore T_{icm}/T_c must increase as $\alpha \rightarrow \infty$. The net result is that T_c decreases faster than T_{icm} increases because $M = M_c + M_{icm}$ is a constant whereas $L_{abs} = L_c + L_{icm} = 2L_{icm}$ is decreasing as $\alpha \rightarrow \infty$ and $f_c = f_L(\alpha)$. Thus the dust in opaque clumps becomes self shielding. Note that the spectrum of the emitted radiation is dominated by dust at temperature T_c if $f_c > f_L(\alpha)$, since then $L_c > L_{icm}$, or it is dominated by dust at temperature T_{icm} if $f_c < f_L(\alpha)$.

The temperature of silicates also exhibits the same variations but with lower values since silicates absorb only about 25% of what graphites absorb for the chosen composition. The same type of pattern, shown here for specific values of r_c, T_s, L_s , and source type, is found for other values of r_c, T_s, L_s , and the central point source or uniformly illuminating external source types. The dust temperatures are lower as L_s is decreased, and there is less variation in T_{icm}/T_c as T_s or r_c is decreased. Cases of $T_s > 20,000\text{K}$ would require modeling the ionization of gas and the heating of dust by absorption of Ly α photons.

8. SUMMARY AND CONCLUSIONS

We have introduced an analytical model for the escape and absorption of radiation in two-phase clumpy media, based on combining the mega-grains approximation of HP93 with escape/absorption probability formulae for homogeneous media, as summarized in §5, and referred to by the acronym MGEP. Enhancements of the mega-grains approximation developed in this paper include: (1) improved and extended the formula for effective optical depth to all clump filling factors, (2) improved the formula for the effective albedo, (3) developed a new approximation for the effective scattering asymmetry parameter, and (4)

developed new approximations for the fractions absorbed by each phase of the medium. We also developed a new approximation for the fraction of photons from a uniformly illuminating external source that are absorbed in a sphere of dust when scattering occurs.

The space of parameters describing a two-phase clumpy dusty environment is six-dimensional: the clump filling factor, the clump to interclump medium (ICM) density ratio, and the clump radii, together characterize the morphology of the medium, and the interaction (absorption plus scattering) coefficient, scattering albedo and asymmetry parameter are the three optical parameters of the dust which vary with wavelength. The analytic MGEP model was compared with Monte Carlo simulations of radiative transfer (MCRT) over a subspace of the six-dimensional parameter space, and we found good agreement for most of the parameter values checked. More importantly, the qualitative behavior of the MGEP model agrees very well with MCRT simulations, giving us confidence in applying the MGEP model to parameter ranges which have not yet been checked by MCRT simulations. Three types of source distributions were studied: the central point source (C), uniformly distributed internal sources (U), and uniform illumination by external sources (X). Source type U is the least absorbed, whereas source type X is the most absorbed at low optical depths and source type C is the most absorbed at high optical depths.

The MGEP model was shown to predict very well the emerging SED in a realistic simulation of stellar-like sources heating a clumpy dusty medium, as compared to MCRT simulations. Furthermore, the MGEP method requires just seconds to compute a full spectrum simulation, in comparison to hours of computation when using the MCRT method.

From MGEP simulations over a wide range parameters characterizing the clumpy medium we find that for constant clump to ICM density ratio, α , the total luminosity absorbed by the clumpy medium attains a minimum at the filling factor, f_c , for which the luminosity absorbed by clumps (L_c) and the ICM (L_{icm}) are equal. The curve of f_c versus α for which $L_c = L_{icm}$ is found to be proportional to $\alpha^{-\frac{1}{2}}$, a consequence of the clumps becoming optically thick, whereas the curve of f_c for which the clumps and ICM have equal mass is proportional to α^{-1} , and these diverging behaviors cause the temperature of dust in clumps to decrease as $\alpha \rightarrow \infty$ and $f_c \rightarrow 0$. Physically, the dust in opaque clumps shields itself from radia-

tion, thus reaching a lower equilibrium temperature than dust in the ICM. The extra parameters gained by introducing clumpiness allows for modeling more unusual relationships between the luminosity absorbed by dust and the resulting dust temperatures.

We would like to acknowledge useful comments and suggestions given by the referee, Mike Hobson, and by Michel Fioc. This research was supported by the NASA Astrophysical Theory Program NRA97-12-OSS-098.

A. FINAL FLUX APPORTIONMENT IN MONTE CARLO

Let N_0 be the number of photons emitted as a group at the start of the Monte Carlo simulation and suppose after k iterations of traveling, escape, absorption and scattering there are N_k photons remaining in the medium. Since after each scattering the flux weight of each photon is reduced by the albedo $0 < \omega < 1$, the actual flux remaining after k scatterings is $\omega^k N_k$. For clarity in the following derivation define the flux weight factor

$$W_k \equiv \omega^k. \quad (\text{A1})$$

After one more iteration of traveling there are N_{k+1} photons remaining, each still having weight W_k , so that the flux escaping during the $k + 1$ iteration is $E_{k+1} = W_k(N_k - N_{k+1})$. The remaining photons interact with the medium and are apportioned into absorbed and scattered fractions: the absorbed flux is $A_{k+1} = (1 - \omega) W_k N_{k+1}$, and the flux remaining after scattering is $\omega W_k N_{k+1} = W_{k+1} N_{k+1}$. Carrying this analysis forward by induction gives the general formula for the escaping flux after each iteration:

$$\begin{aligned} E_{k+1} &= W_k(N_k - N_{k+1}) \\ E_{k+2} &= W_{k+1}(N_{k+1} - N_{k+2}) \\ &\vdots \\ E_{k+n} &= \omega^{k+n-1}(N_{k+n-1} - N_{k+n}); \end{aligned} \quad (\text{A2})$$

and the absorbed flux after each iteration:

$$\begin{aligned} A_{k+1} &= (1 - \omega) W_k N_{k+1} \\ A_{k+2} &= (1 - \omega) W_{k+1} N_{k+2} \\ &\vdots \\ A_{k+n} &= (1 - \omega) \omega^{k+n-1} N_{k+n}. \end{aligned} \quad (\text{A3})$$

We seek expressions for the infinite sums of E_{k+n} and A_{k+n} over $n > 0$ in order to terminate the Monte Carlo simulation at the k -th iteration and still have an accurate estimate of the escaping flux. Assume that for all $n > 0$

$$\frac{N_{k+n}}{N_{k+n-1}} = \beta \quad , \quad (\text{A4})$$

so that after k iterations the fraction of photons remaining after each additional iteration is assumed to have reached a steady state. Then we have

$$N_{k+n} = \beta^n N_k \quad , \quad (\text{A5})$$

$$N_{k+n-1} - N_{k+n} = (1 - \beta)\beta^{n-1} N_k \quad . \quad (\text{A6})$$

The sum of the escaping flux is then:

$$\begin{aligned} \sum_{n=1}^{\infty} E_{k+n} &= \omega^k \sum_{n=1}^{\infty} \omega^{n-1} (N_{k+n-1} - N_{k+n}) \\ &= \omega^k N_k (1 - \beta) \sum_{n=1}^{\infty} (\omega\beta)^{n-1} \\ &= \omega^k N_k (1 - \beta) / (1 - \omega\beta) \quad . \quad (\text{A7}) \end{aligned}$$

Since $\omega^k N_k$ is the known amount of flux remaining after k iterations, the fraction that would eventually escape if the iterations were continued is then

$$f_k^{esc} = \frac{1 - \beta}{1 - \omega\beta} \quad , \quad (\text{A8})$$

assuming that eq.(A4) is true. Similarly for the sum of the absorbed flux

$$\begin{aligned} \sum_{n=1}^{\infty} A_{k+n} &= (1 - \omega)\omega^k \sum_{n=1}^{\infty} \omega^{n-1} N_{k+n} \\ &= \omega^k N_k (1 - \omega) \sum_{n=1}^{\infty} \omega^{n-1} \beta^n \\ &= \omega^k N_k (1 - \omega)\beta / (1 - \omega\beta) \quad , \quad (\text{A9}) \end{aligned}$$

and it is clear that

$$f_k^{esc} + f_k^{abs} = \frac{1 - \beta}{1 - \omega\beta} + \frac{(1 - \omega)\beta}{1 - \omega\beta} = 1 \quad , \quad (\text{A10})$$

giving a check of the derivations. Note that the simpler assumption of $f_k^{esc} = \omega$ and $f_k^{abs} = 1 - \omega$ corresponds to the case of $\beta = 1/(1 + \omega)$, which incorporates no knowledge of the particular radiative transfer situation and could not possibly work for all types of

sources and geometries. In contrast, the final iteration escaping fraction given by eq.(A8) is based on a partial history of absorption and scattering and therefore can better estimate the true value.

To examine the effects of relaxing the assumption of eq.(A4), define the remaining fraction at the k -th iteration:

$$\beta_k \equiv \frac{N_k}{N_{k-1}} \quad , \quad (\text{A11})$$

the ratio of the number of photons remaining after the k -th iteration over the number of photons in the medium before the k -th iteration. In our experience with Monte Carlo simulations we find that the sequence β_k ($k = 1, 2, 3, \dots$) is monotonically either increasing or decreasing (does not oscillate), and the direction of convergence depends on the source geometry and the value of g , the phase function asymmetry parameter. In our Monte Carlo simulations with uniformly distributed internal emitters, the sequence β_k converges rapidly, and using β_k in place of β in eq.(A8) gives an f_k^{esc} which predicts the total escaping flux quite well. The remaining fraction β_k is found to be an increasing sequence when $g < g^*(\tau)$, where $g^*(\tau)$ is approximately given by eq.(21), since photons tend to get trapped in the medium when scattering is more isotropic. When $g > g^*(\tau)$ then β_k is a decreasing sequence, since photons tend to escape after more scatterings if the angular scattering distribution is on average more forward. When $g = g^*(\tau)$ we find that the sequence β_k is essentially constant. This dependence on the asymmetry parameter g is related to the validity of the escape probability formula for scattering discussed in §3.2 and further analyzed in Appendix C2. The behavior of the sequence β_k is essentially the same for a uniformly illuminating external source of photons. In the extreme case of a single central source, it takes more scatterings for β_k to converge and it is always a decreasing function of k . Thus f_k^{esc} always slightly overestimates the escaping fraction for the case of a central source, but never underestimates it. When the scattering is more forward the rate of decreasing β_k is faster during the first few scatterings, since in this case the likelihood that a photon will escape increases after each scattering more than when the scattering is isotropic.

The discovery of the above equations and behavior was facilitated by the use of dynamic arrays to represent a group of photons, a standard feature of the Interactive Data Language (IDL), a product of Research Systems Incorporated (RSI).

B. RANDOM CLUMPS IN A TWO PHASE MEDIUM

In section 2.2 we introduced equation (11) for the number of identical random clumps needed to produce a given volume filling factor in a two-phase medium. Here we give a more detailed derivation of that equation. Let X be a randomly chosen point in the medium. Then the probability that a randomly placed clump will contain the point X is simply

$$p \equiv \frac{v_c}{V} \quad (\text{B1})$$

where v_c is the volume of a clump, and V is the total volume of the medium. Continue to randomly place more clumps in the medium, without regard to overlaps, for a total of N_c clumps. Then the probability, $P(n)$, that the point X will be contained in n clumps is given by the binomial distribution:

$$P(n) = \binom{N_c}{n} p^n (1-p)^{N_c-n} \quad (\text{B2})$$

In particular, the probability that X is not in any clump is

$$P(0) = (1-p)^{N_c} \quad (\text{B3})$$

and so the fraction of the volume V occupied by the clumps is

$$f_c = 1 - P(0) = 1 - (1-p)^{N_c} \quad (\text{B4})$$

Solving for N_c gives the desired equation

$$N_c = \frac{\ln(1-f_c)}{\ln(1-p)} \quad (\text{B5})$$

for the number of identical randomly placed clumps which will have a total filling factor of f_c , when each clump has a filling factor p .

The expectation value for n of the binomial distribution [eq.(B2)] is

$$E(n) = \sum_{n=0}^{N_c} nP(n) = N_c p = \frac{N_c v_c}{V} = Q_c, \quad (\text{B6})$$

equaling the porosity of the clumps, Q_c , which was introduced for the mega-grains approximation. As $p \rightarrow 0$ and $N_c \rightarrow \infty$ the binomial distribution is well approximated by the Poisson distribution having the same expectation (e.g. Bevington & Robinson 1992):

$$P(n) \simeq \frac{Q_c^n e^{-Q_c}}{n!} \quad (\text{B7})$$

For $n = 0$ this approximation gives

$$f_c = 1 - P(0) \simeq 1 - e^{-Q_c}, \quad (\text{B8})$$

providing another equation relating porosity and filling factor, which is exact for our purposes, since $p < 10^{-3}$ (e.g. when $r_c < 0.1 R_S$) and $N_c \gg 1$. When $f_c \ll 1$ then of course $f_c \simeq Q_c$.

Another quantity of interest is the average number of clumps encountered along a randomly chosen line of sight, also called the covering factor, F_c . Consider a cylinder of radius r_c and length L centered on the line of sight. The volume of the intersection of the cylinder with the random clumps is $\pi r_c^2 L f_c$ and we can estimate the number of clumps in the intersection by dividing by the volume of a clump:

$$F_c \approx \frac{\pi r_c^2 L f_c}{\frac{4}{3} \pi r_c^3} = L \left(\frac{3f_c}{4r_c} \right) \quad (\text{B9})$$

This is actually more like a lower bound estimate since the clumps may overlap. An upper bound is obtained by using the porosity in place of the filling factor:

$$F_c < L \left(\frac{3Q_c}{4r_c} \right) \quad (\text{B10})$$

C. ESCAPE AND INTERACTION PROBABILITIES FOR A SPHERE

C.1. No Scattering

Here we derive equations (26) and (19), which are exact formulas for the interaction and escape probabilities of external and internal sources, respectively, in a homogeneous sphere of dust, ignoring the effects of scattering. Thus, scattering and absorption are considered together as interactions causing extinction of photons along a line of sight, and by extinction escape probability we mean the probability of escaping without being scattered or absorbed. Consider a ray intersecting the sphere at an angle θ with respect to the surface normal vector, which we call the impact angle. The length of the chord created by the intersection is $2R \cos \theta$, where R is the radius of the sphere. Defining $\tau \equiv \rho \kappa R$, the optical radius, where κ is the dust interaction coefficient and ρ is the density of dust, the extinction optical depth of the chord is $2\tau \cos \theta$, and this will be used in the derivations.

To derive the interaction probability, eq.(26), for the case of a uniformly illuminating external source,

consider a beam of photons traveling in parallel rays impacting a hemisphere. Upon computing the transmission of the beam we can get the interacting fraction of photons, and then by symmetry this gives the interaction probability for all possible beams impacting the sphere, i.e. a uniformly illuminating external source. Let I_0 be the intensity of each parallel ray in the impacting beam. Then the intensity emerging from the other side is reduced by the extinction which depends on the impact angle as follows:

$$I_{out}(\tau, \theta) = I_0 \exp(-2\tau \cos \theta) \quad . \quad (C1)$$

The total flux emerging without interaction is computed by integrating over all impact angles with respect to solid angle:

$$\begin{aligned} F_{out}(\tau) &= 2\pi I_0 \int_0^{\pi/2} e^{-2\tau \cos \theta} \cos \theta \sin \theta d\theta \\ &= 2\pi I_0 \int_0^1 \mu e^{-2\tau \mu} d\mu \quad (C2) \\ &= \pi I_0 \left[\frac{1}{2\tau^2} - \left(\frac{1}{\tau} + \frac{1}{2\tau^2} \right) e^{-2\tau} \right], \end{aligned}$$

where we have used the substitution of variables $\mu = \cos \theta$ and integration by parts. The flux that would emerge if the sphere was empty is computed by integrating with $\tau = 0$ in eq.(C2), obtaining

$$F_0 \equiv F_{out}(0) = 2\pi I_0 \int_0^1 \mu d\mu = \pi I_0 \quad . \quad (C3)$$

So the fraction of photons which interact is

$$\begin{aligned} P_i(\tau) &= \frac{F_0 - F_{out}(\tau)}{F_0} \quad (C4) \\ &= 1 - \frac{1}{2\tau^2} + \left(\frac{1}{\tau} + \frac{1}{2\tau^2} \right) e^{-2\tau}, \end{aligned}$$

giving the interaction probability for a uniformly illuminating external source. For the case of an optically thin sphere note that the extinction behaves as

$$e^{-2\tau \mu} \rightarrow 1 - 2\tau \mu \quad \text{when } \tau \ll 1, \quad (C5)$$

and so the emerging flux is

$$\begin{aligned} F_{out}(\tau \sim 0) &\simeq 2\pi I_0 \int_0^1 \mu (1 - 2\tau \mu) d\mu \\ &= \pi I_0 \left[1 - \frac{4\tau}{3} \right], \quad (C6) \end{aligned}$$

and as expected this gives

$$P_i(\tau \sim 0) \simeq \frac{4\tau}{3} \quad . \quad (C7)$$

For the case of uniformly distributed internal emission, the probability of escaping without interactions, eq.(19), can be derived in a similar fashion. Let ϵ be the emission per unit volume per second. Then the non-interacting intensity emerging from a ray at an angle θ with respect to the surface normal is

$$I_{out}(\tau, \theta) = \frac{\epsilon}{\rho\kappa} (1 - e^{-2\tau \cos \theta}), \quad (C8)$$

obtained in the standard fashion by integrating the transfer equation with no scattering along the chord of optical length $2\tau \cos \theta$ through the sphere. The total non-interacting flux emerging in any given direction is computed by integrating with respect to solid angle, as in eq.(C2), over all the parallel rays:

$$\begin{aligned} F_{out}(\tau) &= \frac{2\pi\epsilon}{\rho\kappa} \int_0^{\pi/2} (1 - e^{-2\tau \cos \theta}) \cos \theta \sin \theta d\theta \\ &= \frac{2\pi\epsilon}{\rho\kappa} \int_0^1 (1 - e^{-2\tau \mu}) \mu d\mu \quad (C9) \\ &= \frac{\pi\epsilon}{\rho\kappa} \left[1 - \frac{1}{2\tau^2} + \left(\frac{1}{\tau} + \frac{1}{2\tau^2} \right) e^{-2\tau} \right], \end{aligned}$$

obtaining a result similar to the interaction probability above, due to the same exponential term in the integral. If the medium had zero absorption and scattering, the intensity emerging from a ray is

$$I_0(R, \theta) = 2\epsilon R \cos \theta \quad . \quad (C10)$$

The total flux emerging in any given direction is again computed by integrating with respect to solid angle over all the parallel rays:

$$\begin{aligned} F_0(R) &= \int_0^{2\pi} d\phi \int_0^{\pi/2} d\theta \cos \theta \sin \theta I_0(R, \theta) \\ &= 4\pi\epsilon R \int_0^1 \mu^2 d\mu = \frac{4\pi\epsilon R}{3}. \quad (C11) \end{aligned}$$

So the fraction of photons which escape the sphere is

$$\begin{aligned} P_e(\tau) &= \frac{F_{out}(\tau)}{F_0(R)} \quad (C12) \\ &= \frac{3}{4\tau} \left[1 - \frac{1}{2\tau^2} + \left(\frac{1}{\tau} + \frac{1}{2\tau^2} \right) e^{-2\tau} \right], \end{aligned}$$

using the fact that $\tau = \rho\kappa R$, giving the extinction escape probability for a uniformly distributed internal source.

TABLE C2
MULTIPLE SCATTERING AND ESCAPE

#	interacting	absorbed	scattered	escaping
1	$1 - P$	$(1 - \omega)(1 - P)$	$\omega(1 - P)$	$P\omega(1 - P)$
2	$\omega(1 - P)^2$	$(1 - \omega)\omega(1 - P)^2$	$\omega^2(1 - P)^2$	$P\omega^2(1 - P)^2$
3	$\omega^2(1 - P)^3$	$(1 - \omega)\omega^2(1 - P)^3$	$\omega^3(1 - P)^3$	$P\omega^3(1 - P)^3$
\vdots	\vdots	\vdots	\vdots	\vdots
n	$\omega^{n-1}(1 - P)^n$	$(1 - \omega)\omega^{n-1}(1 - P)^n$	$\omega^n(1 - P)^n$	$P\omega^n(1 - P)^n$

C.2. Including Scattering

Equation (20), which approximately includes the effects of scattering into any extinction escape probability for the case of uniformly distributed isotropic emitters in a bounded medium, was presented in Lucy et al. (1991) but no derivation was given. In this section we derive the equation and point out some interesting properties. The scattering albedo of the medium is the fraction of the extinction optical depth that is due to scattering: $\omega = \tau_{scat}/\tau_{ext}$, where $\tau_{ext} = \tau_{abs} + \tau_{scat}$, is the sum of absorption and scattering optical depths from the center to the boundary of the medium, e.g. the radius of a sphere. Assume that we are given the escape probability, $P_e(\tau)$, for absorption only, as a function of the optical depth of the bounded medium. We can immediately use $P_e(\tau)$ to give the fraction of emitted photons which escape without interacting (not absorbed *or* scattered), by using $\tau = \tau_{ext}$. For convenience we shall identify $P \equiv P_e(\tau)$ in the following derivation. Thus a fraction P of photons escape with no interactions and a fraction $1 - P$ interacts with the medium. Then by definition of the albedo, a fraction $(1 - \omega)(1 - P)$ is absorbed and the fraction $\omega(1 - P)$ is scattered for the first time. Assume that the scattered photons are distributed uniformly in the medium and the directions of travel are isotropic. Then we can apply the extinction escape probability again to find that a fraction $P\omega(1 - P)$ escapes after one scattering. Repeating these steps, observe that a fraction $\omega(1 - P)^2$ interacts with the medium to result in a fraction $\omega^2(1 - P)^2$ that scatters a second time. Continuing to assume that the scattered photons are uniformly distributed and isotropic it follows that a fraction $P\omega^2(1 - P)^2$ escapes after two scatterings.

Table C2 summarizes the analysis of the fractions in each state and extends it by induction. The first column is the number of interactions that have occurred. The column labeled “scattered” feeds back into the “interacting” column of the next row with another factor of $1 - P$ to give the next interaction. Note that for the first interaction, the photons that are absorbed have experienced zero scatterings, so that the number of scatterings for fractions in the “interacting” and “absorbed” columns is one less than the interaction number. The induction presented in the table shows that a fraction $P\omega^n(1 - P)^n$ escapes after n scatterings. Summing these escaping fractions over an infinite number of scatterings gives the sought after formula for the total escaping fraction:

$$\begin{aligned} \mathcal{P}_{esc}(\tau, \omega) &= P \sum_{n=0}^{\infty} \omega^n (1 - P)^n \\ &= \frac{P}{1 - \omega(1 - P)}. \end{aligned} \quad (\text{C13})$$

Recall that the formula is valid (most accurate) at a single value of the scattering asymmetry parameter, which in the case of spherical geometry is approximately given by eq.(21). The absorbed fractions listed in the third column of Table C2 can also be summed to get the total absorbed fraction:

$$\begin{aligned} \mathcal{P}_{abs}(\tau, \omega) &= (1 - \omega)(1 - P) \sum_{n=0}^{\infty} \omega^n (1 - P)^n \\ &= \frac{(1 - \omega)(1 - P)}{1 - \omega(1 - P)}, \end{aligned} \quad (\text{C14})$$

finding that $\mathcal{P}_{esc}(\tau, \omega) + \mathcal{P}_{abs}(\tau, \omega) = 1$, which gives a check of the above derivations.

Let us define distributions, $p_e(n)$ and $p_a(n)$, for the probability that a photon will escape or get absorbed after n scatterings. To arrive at a probability distribution, the fraction $P\omega^n(1-P)^n$ which escapes after n scatterings must be normalized by dividing by the total escaping fraction, obtaining

$$\begin{aligned} p_e(n) &= \frac{P\omega^n(1-P)^n}{\mathcal{P}_{esc}(\tau, \omega)} \\ &= [1 - \omega(1-P)]\omega^n(1-P)^n, \end{aligned} \quad (\text{C15})$$

after substituting eq.(C13). As mentioned before, the number of scatterings occurring for the absorbed fractions listed in the third column of Table C2 is actually $n-1$, where n is the number of interactions given in the first column. Therefore, the probability distribution of absorption after n scatterings is

$$\begin{aligned} p_a(n) &= \frac{(1-\omega)\omega^n(1-P)^{n+1}}{\mathcal{P}_{abs}(\tau, \omega)} \\ &= [1 - \omega(1-P)]\omega^n(1-P)^n, \end{aligned} \quad (\text{C16})$$

resulting in the fact that $p_a(n) = p_e(n)$ for all n . Of course this can be true only when $\mathcal{P}_{esc}(\tau, \omega)$ is valid. Monte Carlo simulations verify that the escaping and absorbed probability distributions are equal *only* when equation (C13) agrees with the Monte Carlo results, which occurs only for a single value of the scattering asymmetry parameter g , as discussed in section 3.2 for the case of spherical geometry.

Defining $A \equiv 1 - P$, the average number of scatterings that a photon experiences before escape or absorption is calculated as

$$\begin{aligned} \langle n_{scat} \rangle_* &= \sum_{n=0}^{\infty} n p_e(n) \\ &= \sum_{k=0}^{\infty} \left(\sum_{n=0}^{\infty} p_e(n) - \sum_{n=0}^k p_e(n) \right) \\ &= \sum_{k=0}^{\infty} \left(1 - [1 - \omega A] \left[\frac{1 - \omega^{k+1} A^{k+1}}{1 - \omega A} \right] \right) \\ &= \sum_{k=1}^{\infty} \omega^k (1-P)^k \\ &= \frac{1}{1 - \omega(1-P)} - 1 \\ &= \frac{\mathcal{P}_{esc}(\tau, \omega)}{P_e(\tau)} - 1. \end{aligned} \quad (\text{C17})$$

Monte Carlo simulations for the case of uniform emission within a homogeneous sphere of absorbers and

scatterers again verifies that when the asymmetry parameter takes on the particular value $g = g^*(\tau)$, approximately given by eq.(21), then the average number of scatterings experienced by photons is the same whether the final state is escape or absorption: $\langle n_{scat} \rangle_{esc} = \langle n_{scat} \rangle_* = \langle n_{scat} \rangle_{abs}$. For other values of g we find that $\langle n_{scat} \rangle_{esc} < \langle n_{scat} \rangle_* < \langle n_{scat} \rangle_{abs}$ when $g < g^*(\tau)$, so that absorption occurs after more scatterings than escape since there is more absorption than predicted by eq.(C13), whereas $\langle n_{scat} \rangle_{esc} > \langle n_{scat} \rangle_* > \langle n_{scat} \rangle_{abs}$ when $g > g^*(\tau)$, since there are more escaping photons than predicted. We conjecture that the ratio of $\langle n_{scat} \rangle_{esc}$ to $\langle n_{scat} \rangle_{abs}$ can only be affected by g and τ because it is dependent on geometry: the directions of scattering and proximity to the boundary of the medium. The albedo ω gives probability of absorption versus scattering and so affects the magnitude of $\langle n_{scat} \rangle_*$, but it does not enter into the geometry of photon paths, possibly explaining why $g^*(\tau)$ is independent of ω . Note that as the medium becomes optically thick ($\tau \rightarrow \infty$) then $P \rightarrow 0$ and then eq.(C17) predicts that $\langle n_{scat} \rangle_* \rightarrow \omega/(1-\omega)$ from below, and so for $g \leq g^*(\tau)$ we have that $\langle n_{scat} \rangle_{esc} \leq \omega/(1-\omega)$, which is effectively for all g since $g^*(\tau) \rightarrow 1$ as $\tau \rightarrow \infty$.

D. ANALYSIS OF CLUMP OVERLAPS

To extend the mega-grains approximation to high filling factors, consider that as $f_c \rightarrow 1$ it is the increase of clump overlaps which makes the mega-grains model become unrealistic. Since we ignore the extra density occurring in overlaps, the effective radii of the clumps can be reduced to eliminate most of the overlapping and the number of clumps then must be increased to retain the same filling factor. The volume of clump overlaps is $V(Q_c - f_c)$ and so the average overlap per clump is

$$\frac{V(Q_c - f_c)}{N_c} = v_c \left(\frac{Q_c - f_c}{Q_c} \right) \quad (\text{D1})$$

where we have applied eq.(44) and v_c is the volume of just one clump. Suppose there is a pair of clumps which overlap in volume by the amount given in eq.(D1), then to find the reduced radius at which the pair of clumps would not overlap we must solve

$$\frac{v_c}{2} \left(\frac{Q_c - f_c}{Q_c} \right) = \frac{\pi}{3} h^2 (3r_c - h) \quad (\text{D2})$$

for h , the half-depth of the overlap, where r_c is the clump radius. The reduced radius which eliminates the overlap is then given by $r_c - h$. We have solved eq.(D2) numerically for the full range of filling factors $0 < f_c < 1$ and find that $r_c(1 - f_c) < r_c - h$ as $f_c \rightarrow 1$, thus eliminating the overlap. We propose to substitute $r_c(1 - f_c)^\gamma$ for all instances of r_c in the mega-grains equations, where γ is an optional tuning parameter. In this new model, when $\gamma = 1$, the density of clumps is

$$n_c = \frac{3f_c}{4\pi r_c^3(1 - f_c)^3} > \frac{3Q_c}{4\pi r_c^3} \quad (\text{D3})$$

thus greater than originally defined, and we assume that the radius renormalization has effectively eliminated overlaps while preserving the filling factor.

E. DISTRIBUTION OF DUST TEMPERATURES AROUND A POINT SOURCE OF RADIATION

Given an isotropic point source of radiation in a spherically symmetric medium, the resulting distribution of radiation and heating of the dust is then a function of only the radial distance r from the point source. We will show that the probability distribution of dust temperatures can be approximated by a power law function if the dust density and absorbed luminosity versus r , and if the emitted luminosity versus dust temperature can be approximated by power law functions. Letting $N(r)$ be the number of dust grains in a sphere of radius r , our approach is to obtain approximations for

$$\frac{dN}{dT} = \frac{dN}{dr} \left(\frac{dT}{dr} \right)^{-1}, \quad (\text{E1})$$

which then gives the functional form for the distribution of temperatures.

Assume that the luminosity absorbed by the dust at distance r varies like an inverse power law with exponent η ,

$$L_{abs}(r) \sim m(r) r^{-\eta}, \quad (\text{E2})$$

which in the optically thin case is nearly exact with $\eta = 2$, where $m(r)$ is the mass of dust in a thin shell at radius r . When the dust is optically thick we expect $\eta > 2$, because the absorbed luminosity decays more rapidly than any power law (η is then also a function

of r). The luminosity emitted by the dust scales with the dust temperature, $T(r)$, approximately as

$$\begin{aligned} L_{em}[T(r)] &\equiv 4\pi m(r) \int_0^\infty B_\nu[T(r)] \kappa_\nu d\nu \\ &\sim m(r) T(r)^{4+\beta}, \end{aligned} \quad (\text{E3})$$

if the emissivity per unit mass of the dust scales with frequency like $\kappa_\nu \sim \nu^\beta$, and usually $0 < \beta \leq 2$. Equating the absorbed and emitted luminosities of the dust we get an approximate relationship between dust temperature and radial distance:

$$T(r) \sim r^{-\frac{\eta}{4+\beta}}. \quad (\text{E4})$$

The rate of change in temperature with respect to radial distance then varies as:

$$\frac{dT}{dr} \sim r^{-\left(1 + \frac{\eta}{4+\beta}\right)} \sim T^{(1 + \frac{4+\beta}{\eta})}, \quad (\text{E5})$$

where we have also inverted eq.(E4) and substituted for r .

Assume that the dust density is approximately a power law $\rho(r) \sim r^{-\delta}$, so that the number of dust grains, $N(r)$, in a sphere of radius r also varies like a power law function:

$$N(r) = 4\pi \int_0^r \rho(s) s^2 ds \sim r^{3-\delta}. \quad (\text{E6})$$

Then

$$\frac{dN}{dr} \sim r^{2-\delta} \sim T^{(\delta-2)\left(\frac{4+\beta}{\eta}\right)}, \quad (\text{E7})$$

where we have again substituted for r using eq.(E4). Combining eqs.(E5) and (E7) into (E1):

$$\frac{dN}{dT} \sim T^{(\delta-2)\left(\frac{4+\beta}{\eta}\right)} T^{(-1 - \frac{4+\beta}{\eta})} \quad (\text{E8})$$

$$\sim T^{(\delta-3)\left(\frac{4+\beta}{\eta}\right) - 1}. \quad (\text{E9})$$

From this scaling approximation we presume that the distribution of dust temperatures follows a power law

$$p(T) = a T^\mu \quad (\text{E10})$$

with exponent

$$\mu = (\delta - 3) \left(\frac{4 + \beta}{\eta} \right) - 1, \quad (\text{E11})$$

which is certainly negative as long as $\delta \leq 3$. The normalizing factor a is determined by requiring

$$\int_{T_{\min}}^{T_{\max}} p(T) dT = 1, \quad (\text{E12})$$

where T_{\max} is usually the dust sublimation temperature ($\sim 1500\text{K}$) and T_{\min} is the minimum dust temperature. Actually, the minimum dust temperature is the major free parameter in this theory, and is determined by balancing the absorbed and emitted dust luminosities:

$$\int_0^R L_{\text{abs}}(r)r^2 dr = M \int_{T_{\min}}^{T_{\max}} p(T)K(T)dT, \quad (\text{E13})$$

where M is the total mass of dust contained in a sphere of radius R , and where

$$K(T) = \int_0^\infty B_\nu(T)\kappa_\nu d\nu \quad (\text{E14})$$

is the Planck averaged emissivity at temperature T . Most of the emission comes from dust at temperatures near T_{\min} since those dust grains occupy most of the volume and the dust temperature decays rapidly with distance from the point source. Once T_{\min} is determined, the IR emission spectrum from the dust grains is given by

$$F_\nu = 4\pi M\kappa_\nu \int_{T_{\min}}^{T_{\max}} B_\nu(T)p(T) dT. \quad (\text{E15})$$

The behavior of the emissivity of graphite or silicates changes at wavelengths longer than about $10\mu\text{m}$, therefore we find that the power law approximation of the emissivity averaged with a Planck function at a given temperature (proportional to the luminosity emitted by dust),

$$K(T) \sim T^{4+\beta_i}, \quad (\text{E16})$$

requires two exponents, β_i , with $i = 1$ for $T > T_b$, and $i = 2$ for $T \leq T_b$, where T_b is called the emissivity break temperature, corresponding to the wavelength at which the behavior of the dust emissivity changes. From examination of the behavior of $K(T)$, the values of β_i and T_b are found to be approximately

$$\beta_i = \left\{ \begin{array}{ll} (1.0, 2.0) & \text{(graphite)} \\ (0.5, 2.0) & \text{(silicates)} \end{array} \right\} \quad (\text{E17})$$

and

$$T_b = \left\{ \begin{array}{ll} 80\text{K} & \text{(graphite)} \\ 150\text{K} & \text{(silicates)} \end{array} \right\}. \quad (\text{E18})$$

Consequently, the power law distribution of temperatures around a central source will have an exponent depending on the dust temperature range:

$$\mu_i = (\delta - 3) \left(\frac{4 + \beta_i}{\eta} \right) - 1 \quad (\text{E19})$$

yielding power law probability distributions

$$p_i(T) \equiv a_i T^{\mu_i}, \quad (\text{E20})$$

where the constants a_i are determined by requiring that $p_1(T_b) = p_2(T_b)$ and

$$\int_{T_b}^{T_{\max}} p_1(T)dT + \int_{T_{\min}}^{T_b} p_2(T)dT = 1, \quad (\text{E21})$$

yielding (defining $\gamma_i = \mu_i + 1$)

$$\begin{aligned} a_2 &= a_1 T_b^{\gamma_1 - \gamma_2} \\ a_1 &= \frac{\gamma_1 \gamma_2}{\gamma_2 T_{\max}^{\gamma_1} + (\gamma_1 - \gamma_2) T_b^{\gamma_1} + \gamma_1 T_{\min}^{\gamma_2} T_b^{\gamma_1 - \gamma_2}}. \end{aligned} \quad (\text{E22})$$

This approximation for the temperature distribution and resulting IR emission spectrum were found to be in reasonable agreement with Monte Carlo simulations for the case of $\delta = 0$.

REFERENCES

- Bazell, D., Desert, F.X., 1988, *ApJ*, 333, 353
- Bevington, P.R. & Robinson, D.K. 1992, *Data Reduction and Error Analysis for the Physical Sciences* (McGraw Hill), Chapter 2
- Boissé, P. 1990, *A&A*, 228, 483
- Chan, K.-W., Moseley, S.H., Casey, S., Harrington, J.P., Dwek, E., Loewenstein, R., Városi, F., and Glaccum, W. 1997, *ApJ*, 483, 798
- Code, A.D., and Whitney, B.A. 1995, *ApJ*, 441, 400
- Cox, D.P. 1995, in *The Interplay Between Massive Star Formation, the ISM and Galaxy Evolution*, ed. Knuth et al. (Cedex: Editions Frontieres), 223
- Dickey, J.M., and Garwood, R.W. 1989, *ApJ*, 341, 201
- Draine, B.T. 1985, *ApJS*, 57, 587
- Dwek, E. et al. 1997, *ApJ*, 475, 565
- Elmegreen, B.G. 1997, *ApJ*, 477, 196
- Elmegreen, B.G., and Falgarone, E. 1996, *ApJ*, 471, 816
- Falgarone, E. 1995, in *The Interplay Between Massive Star Formation, the ISM and Galaxy Evolution*, ed. Knuth et al. (Cedex: Editions Frontieres), 95

- Gaustad, J.E. and van Buren, D. 1993, *PASP*, 105, 1127
- Gordon, K.D., Witt, A.N., Carruthers, G.R., Christensen, S.A., and Dohne, B.C., 1994, *ApJ*, 432, 641
- Gordon, K.D., Calzetti, D., and Witt, A.N. 1997, *ApJ*, 487, 625
- Heney, L.G., and Greenstein, J.L. 1941, *ApJ*, 93, 70
- Hobson, M.P., and Scheuer, P.A.G. 1993, *MNRAS*, 264, 145
- Hobson, M.P., and Padman, R. 1993, *MNRAS*, 264, 161 (HP93)
- Knapp, G. 1995, *Sky and Telescope*, May, p.20
- Lucy, L.B., Danziger, I.J., Gouiffes, C., and Bouchet, P. 1991, in *Supernovae*, ed. S.E. Woosley (New York: Springer-Verlag), p.82
- Lux, I., and Koblinger, L. 1995, *Monte Carlo Particle Transport Methods: Neutron and Photon Calculations* (Boca Raton, CRC Press), p.40
- Marscher, A.P., Moore, E.M., and Bania, T.M. 1993, *ApJ*, 419, L101
- McKee, C.F. 1995, in *The Interplay Between Massive Star Formation, the ISM and Galaxy Evolution*, ed. Knuth et al. (Cedex: Editions Frontieres), 223
- Murthy, J., Walker, H.J., and Henry, R.C. 1992, *ApJ*, 401, 574
- Natta, A., and Panagia, N. 1984, *ApJ*, 287, 228 (NP84)
- Neufeld, D.A. 1991, *ApJ*, 370, L85
- Neumann, J. 1951, *NBS Applied Math Series*, No. 12, (U.S. Gov. Printing Office), p.36
- Norman, C.A., and Ferrara, A. 1996, *ApJ*, 467, 280
- Osterbrock, D.E. 1989, *Astrophysics of Gaseous Nebulae and Active Galactic Nuclei* (Mill Valley CA: University. Science Books), Appendix 2
- Pfenniger, D., and Combes, F. 1994, *A&A*, 285, 94
- Press, W.H., Teukolsky, S.A., Vetterling, W.T., and Flannery, B.P. 1992, *Numerical Recipes* (Cambridge: Cambridge Univ. Press)
- Rosen, A., and Bregman, J.N. 1995, *ApJ*, 440, 634
- Rybicky, G.B., and Lightman, A.P. 1979, *Radiative Processes in Astrophysics* (John Wiley & Sons), p.37
- Sanders, D.B., Scoville, N.Z., and Solomon, P.M. 1985, *ApJ*, 289, 387
- Spitzer, L. 1978, *Physical Processes in the Interstellar Medium* (John Wiley & Sons)
- Stutzki, J., and Gusten, R. 1990, *ApJ*, 356, 512
- van Buren, D. 1989, *ApJ*, 338, 147
- Városi, F. and Dwek, E. 1997, in *The Ultraviolet Universe at Low and High Redshift*, ed. W. Waller et al. (New York: AIP), 370
- Városi, F. and Dwek, E. 1999, in preparation
- Waller, W.H., Városi, F., Boulanger, F., and Digel, S.W., 1997, in *New Horizons from Multi-wavelength Sky Surveys*, eds. B.J. McLean et al. (IAU Symp. 179: Kluwer Academic), 194
- Witt, A.N. 1977, *ApJSup*, 35, 1
- Witt, A.N., and Gordon, K.D. 1996, *ApJ*, 463, 681
- Wolf, S., Fischer, O., and Pfau, W. 1998, *A&A*, 340, 103